

Cyclokinetic models and simulations for high-frequency turbulence in fusion plasmas

Zhao Deng (赵登)^{1,2,†}, R. E. Waltz³, Xiaogang Wang (王晓钢)^{2,4}

¹*Institute of Fluid Physics, China Academy of Engineering Physics, P.O. Box 919-108, Mianyang 621900, China*

²*State Key Laboratory of Nuclear Physics and Technology, School of Physics, Peking University, Beijing 100871, China*

³*General Atomics, P.O. Box 85608, San Diego, CA 92186-5608, USA*

⁴*Department of Physics, Harbin Institute of Technology, Harbin 150001, China*

Corresponding authors. E-mail: [†]zdzhadeng@foxmail.com

Received September 19, 2015; accepted November 20, 2015

Gyrokinetics is widely applied in plasma physics. However, this framework is limited to weak turbulence levels and low drift-wave frequencies because high-frequency gyro-motion is reduced by the gyro-phase averaging. In order to test where gyrokinetics breaks down, Waltz and Zhao developed a new theory, called cyclokinetics [R. E. Waltz and Zhao Deng, *Phys. Plasmas* 20, 012507 (2013)]. Cyclokinetics dynamically follows the high-frequency ion gyro-motion which is nonlinearly coupled to the low-frequency drift-waves interrupting and suppressing gyro-averaging. Cyclokinetics is valid in the high-frequency (ion cyclotron frequency) regime or for high turbulence levels. The ratio of the cyclokinetic perturbed distribution function over equilibrium distribution function $\delta f/F$ can approach 1.

This work presents, for the first time, a numerical simulation of nonlinear cyclokinetic theory for ions, and describes the first attempt to completely solve the ion gyro-phase motion in a nonlinear turbulence system. Simulations are performed [Zhao Deng and R. E. Waltz, *Phys. Plasmas* 22(5), 056101 (2015)] in a local flux-tube geometry with the parallel motion and variation suppressed by using a newly developed code named rCYCLO, which is executed in parallel by using an implicit time-advanced Eulerian (or continuum) scheme [Zhao Deng and R. E. Waltz, *Comp. Phys. Comm.* 195, 23 (2015)]. A novel numerical treatment of the magnetic moment velocity space derivative operator guarantee accurate conservation of incremental entropy.

By comparing the more fundamental cyclokinetic simulations with the corresponding gyrokinetic simulations, the gyrokinetics breakdown condition is quantitatively tested. Gyrokinetic transport and turbulence level recover those of cyclokinetics at high relative ion cyclotron frequencies and low turbulence levels, as required. Cyclokinetic transport and turbulence level are found to be lower than those of gyrokinetics at high turbulence levels and low- Ω^* values with stable ion cyclotron modes. The gyrokinetic approximation is found to break down when the density perturbation exceeds 20%, or when the ratio of nonlinear $E \times B$ frequency over ion cyclotron frequency exceeds 20%. This result indicates that the density perturbation of the Tokamak L-mode near-edge is not sufficiently large for breaking the gyro-phase averaging. For cyclokinetic simulations with sufficiently unstable ion cyclotron (IC) modes and sufficiently low $\Omega^* \sim 10$, the high-frequency component of the cyclokinetic transport can exceed that of the gyrokinetic transport. However, the low-frequency component of the cyclokinetic transport does not exceed that of the gyrokinetic transport. For higher and more physically relevant $\Omega^* \geq 50$ values and physically realistic IC driving rates, the low-frequency component of the cyclokinetic transport remains smaller than that of the gyrokinetic transport. In conclusion, the “L-mode near-edge short-fall” phenomenon, observed in some low-frequency gyrokinetic turbulence transport simulations, does not arise owing to the nonlinear coupling of high-frequency ion cyclotron motion to low-frequency drift motion.

Keywords turbulence, cyclokinetics, gyrokinetics, drift waves, ion cyclotron modes

PACS numbers 52.35Ra, 52.25Fi, 52.30Gz, 52.55Fa, 52.65Ti

Contents

1	Introduction	2	4	Simulation results	19
2	Cyclokinetics	5	4.1	Standard case	20
2.1	Cyclokinetic equations in the gyro-phase angle form	6	4.1.1	Linear rates	20
2.1.1	The Boltzmann equation	6	4.1.2	Nonlinear saturation	20
2.1.2	Transport equation	6	4.2	Simulation results with stable ion cyclotron modes	21
2.1.3	Equation of motion	6	4.2.1	Linear rates	21
2.1.4	Cyclokinetic equations in gyro-phase angle form	7	4.2.2	Nonlinear simulation results	22
2.1.5	Normalization	8	4.2.3	Physical explanations of the simulation results	23
2.1.6	The Poisson equation	9	4.3	Simulation results with unstable ion cyclotron modes	24
2.2	Cyclokinetic equations in the cyclotron harmonic form	9	4.3.1	Unstable IC modes	24
2.2.1	Cyclotron harmonic transformation	9	4.3.2	Nonlinear simulation results	24
2.2.2	Linear dispersion relation	9	4.3.3	More physical case	26
2.2.3	Nonlinear terms	10	5	Discussion	26
2.2.4	Incremental entropy	11	5.1	Controversy regarding the L-mode near-edge transport “short-fall” problem	26
2.2.5	The Poisson equation	11		Acknowledgements	27
2.3	The cyclokinetic equation in the Fourier harmonic form	12		Appendix A	27
2.3.1	The Fourier transformation	12	A.1	Derivation of cyclokinetic equations	27
2.3.2	Cyclic boundary condition in the gyro phase space	12	A.1.1	The derivation of linear terms	27
2.3.3	Nonlinear terms	12	A.1.2	The derivation of non-conservative nonlinear terms	28
2.3.4	Incremental entropy	12	A.1.3	The derivation of conservative nonlinear terms	28
2.3.5	The Poisson equation	13	A.2	Derivation of nonlinear incremental entropy conservation	30
2.4	Gyrokinetic equations	13	A.2.1	The incremental entropy conservation of the ∂_μ term	30
2.5	Electron equations of motion	13	A.2.2	The incremental entropy conservation of the ∂_α term	31
2.5.1	Non-adiabatic electron model	13		References	33
2.5.2	Collisional drift wave electron model	14			
2.6	Discussion	14			
2.6.1	The reason for omitting the parallel motion and variations	14			
2.6.2	Recipes for generalization and conversion of continuum gyrokinetic implementations to cyclokinetic implementations	14			
3	Numerical method	14			
3.1	Discretization of magnetic moment	16			
3.2	Discretization of magnetic moment derivative operator	16			
3.3	Linear eigenvalue solver	17			
3.4	Time advance method	17			
3.5	Grid convergence test	17			
3.5.1	Wavenumber grid convergence	17			
3.5.2	Harmonic number convergence	17			
3.5.3	Magnetic moment grid convergence	18			
3.6	The rCYCLO code validation	18			
3.6.1	Linear verification	18			
3.6.2	Nonlinear verification	19			

1 Introduction

Known as one of the most promising approaches in fusion energy, magnetic confinement fusion is a historic scientific challenge that may significantly contribute to the world long term energy needs. The principal idea is to constrain high-temperature plasma in a designed magnetic field. Tokamak develops very quickly among magnetic confinement devices, since it possesses the characteristics of strong magnetic field, high temperature, long operation time, and robust operation parameters. There exists multi-scale motion in the Tokamak high-temperature plasma. For most configuration, the fastest (10^{-6} s) and large-scale (machine size) ideal magnetohydrodynamic (MHD) instabilities generally determine the ultimate operational limit. Ideal MHD instabilities are driven by current or pressure gradients. Among these

instabilities, the short-wavelength ballooning mode and the long-wavelength kink mode are typically well understood and can be avoided in principle. Regarding the steady state, the energy and the time of the particle transportation (10^0 s) largely determine the confinement quality. The classical diffusion theory is associated with Coulomb collisions between particles. The classical diffusion coefficient calculated by Rosenbluth and Kaufman [1] is proportional to $1/B^2$ and is much smaller than the experimental value. After accounting for the toroidal effect of the charged particle motion in a real Tokamak configuration, the effective orbit width becomes one order larger in the new classical theory, where the diffusion exceeds the classical diffusion by a factor of q^2 as calculated by Pfirsch and Schluter [2], where q is the safety factor. Although the transport level in the new classical theory is larger than the one in the classical theory, the experimental transport level remains under-predicted by the new classical theory. This under-predicted transport has been termed anomalous transport. This anomalous transport has been attributed to micro-turbulence.

It is well known that micro-turbulence is likely to exist in any large-Reynolds-number fluid, such as air or water, and this phenomenon is captured by the Navier-Stokes equation. For the magnetically confined plasma in Tokamak, it is important to understand and predict the micro-turbulence transport, because it is one of the main processes negatively affecting the ability to maintain confinement for steady state operation. The transport across the magnetic field is dominated by low-frequency drift-wave turbulence. Plasma drift-waves were first discovered in the Q machine, which is a long cylindrical device. Research performed on the Q machine [3] established the localized rotating wave structure of drift-waves, and the phase shift of the drift-waves has been measured. Later, several types of drift-wave instabilities were discovered in the Columbia Linear Machine, including the trapped electron modes [4], trapped ion modes [5], collision-free curvature-driven trapped particle modes [6], and ion temperature gradient modes [7]. In Tokamaks, drift-waves were first discovered in the microwave scattering experiment [8] and in the infrared CO_2 laser scattering experiments [9, 10]. These experiments indicated that drift-waves saturate for a wide range of mixing lengths with a non-adiabatic electron response [11]. After these initial findings, a large number of drift-wave turbulence studies were conducted using different devices, including TEXT, TFTR, ATF, Alcator, ASDEX, Heliotron, and JFT2M. These studies provided very strong evidences [12–16] in support of the idea that drift-wave fluctuations account for the particle and thermal energy transport.

Hassegawa and Mima were the first to describe micro-

turbulence in plasma. According to their theory [17, 18] the plasma micro-turbulence is caused by the nonlinear interaction of the electrostatic $E \times B$ drift motions. The density gradient acts as a source, providing the energy on a large scale. The energy cascades to the small scale, where it is damped by ion collisions. The Hassegawa-Mima model [17, 18] describes the basic idea of a nonlinear wave-wave interaction for plasma turbulence. Following this pioneering studies, additional physical models of micro-turbulence were developed. The Hassegawa-Wakatani model considered the parallel effect [19], while Waltz and Dominguez considered the trapped particle as a fluid and included the FLR effect in their gyro-Landau fluid model [20]. Although these drift wave turbulence-based models explain some of the main features of the Tokamak confinement, many transport-related issues remain to be resolved. Along with rapid advances in development of computing capabilities, it became possible to consider more fundamental and complicated theoretical descriptions in numerical computations.

A milestone of transport theory for magnetically confined plasma is the development of the gyrokinetic theory and of numerical methods for solving the associated gyrokinetic equations. The gyrokinetic theory is more fundamental than the fluid theory. In principle, the six-dimensional Boltzmann equations for each species coupled with the Maxwell equations can be used to describe all collective motion in plasma. The Boltzmann-Maxwell system describes physical phenomena from the micro-scale of ion (and electron) gyro-radius to the macro-scale of machine size; however, the calculation is too computationally expensive and cannot be performed by using the existing computational capabilities. To reduce the calculation complexity, the gyrokinetic equation is obtained after averaging the Boltzmann equation over the gyro-phase angle and expanding the perturbed distribution function to the lowest order. The distribution of gyrocenters is advanced with gyro-averaged fields. The electrostatic formulation of gyrokinetics was generalized in the late 1960s [21, 22] with the electromagnetic fields included in the early 1980s [23, 24], and was quickly extended from linear to nonlinear description [25].

It is well known that gyrokinetic transport simulations in the core regime of Tokamak are in a good agreement with experiments [26], where turbulence levels are low. However, gyrokinetic simulations of some near-edge L-mode Tokamak plasmas using the GYRO code [27] have been found to under-predict both the transport and the turbulence levels by at least 5-fold [26] or even 10-fold in the case of a more turbulent and colder edge [28]. This mismatch for the transport and low-frequency turbulence is called the “L-mode near-edge short-fall”. The

transport “short-fall” problem in the near-edge L-mode Tokamak gyrokinetic transport simulation was discovered by White *et al.* by comparing the GYRO simulations with the DIII-D experiment results in 2007 [29]. They found that both the ion and electron heat diffusivities are under-predicted by a factor of 5 at $\rho_r = 0.75$, where ρ_r is the normalized toroidal flux. The under-predicted factor becomes larger than 5 [26] for $\rho_r > 0.75$ or at higher q , where the level of turbulence is higher. The “short-fall” problem has been well studied in the recent years. Multiple gyrokinetic and gyro-fluid simulation results comparisons solidly established the existence of the transport “short-fall” problem. The results of the nonlinear simulations using GYRO, GEM, and TGLF are compared in Fig. 1 [30].

The L-mode near-edge short-fall suggests that either some important mechanism is missing from the currently used gyrokinetic simulation program such as GYRO, or the gyrokinetic approximation itself becomes invalid. In order to test where gyrokinetics breaks down, Waltz and Zhao have developed a more fundamental theory, termed the cyclokinetic theory [31], and the corresponding simulation code rCYCLO [32]. Cyclokinetics is more fundamental than gyrokinetics. Six-dimensional cyclokinetics can be regarded as an extension of five-dimensional gyrokinetics to include high-frequency ion cyclotron waves. As shown in Fig. 2, cyclokinetics dynamically follows the high-frequency ion gyro-phase motion and nonlinearly

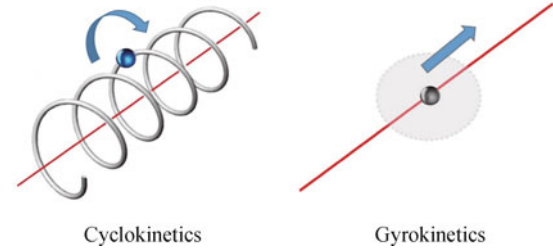


Fig. 2 The comparison between cyclokinetics and gyrokinetics. Cyclokinetics dynamically follows the high-frequency ion gyro-phase motion, while gyrokinetics follows the low-frequency gyro-center motion.

couples the high-frequency ion cyclotron modes to the low-frequency drift modes. Gyrokinetics is an approximation of cyclokinetics, obtained by gyro-averaging over the high-frequency gyro-motion in cyclokinetics, and only follows the low-frequency gyro-center motion. Cyclokinetics recovers both linear and nonlinear gyrokinetics when only the first cyclotron harmonic is retained. The linear low-frequency drift mode rates in cyclokinetics and gyrokinetics are the same. Nonlinear cyclokinetics imposes no limit on the perturbation amplitude, whereas gyrokinetics is limited to the low drift-wave frequencies and weak turbulence levels (with the perturbed $E \times B$ velocity much less than the ion thermal velocity ($\delta v_{\perp}^E \ll v_i^{th}$) on the small scale of the ion gyro-radius ($\rho k_{\perp} \sim O(1)$ in Ref. [33] (p. 113), where k_{\perp} is the perpendicular wavenumber). For comparison, gyrokinetics is limited to weak turbulence levels ($\delta v_{\perp}^E \ll v_i^{th}$) and low drift wave frequencies ($\omega \ll \Omega$), while cyclokinetics extends gyrokinetics to high turbulence levels ($\delta v_{\perp}^E \leq v_i^{th}$) and high frequencies ($\omega \leq N\Omega$). Ω is the ion cyclotron frequency, and N is the largest ion cyclotron harmonic retained.

The high-frequency gyro-motion included in cyclokinetics possibly interrupts and suppresses the gyro-averaging if the turbulence level is sufficiently high. Formally, there is no gyro-averaging when all cyclotron (gyro-phase angle) harmonics of the perturbed distribution function (δf) are retained. It is also possible that sufficiently unstable high-frequency ion cyclotron modes could nonlinearly drive low-frequency turbulence and transport. This leads us to the conjecture that the low-frequency component of the cyclokinetic transport level might be driven higher than in gyrokinetics, so as to recover the L-mode near-edge “short-fall”.

Actually, linear cyclokinetics predates linear gyrokinetics to the early 1960s. In fact, some of the earliest work on “anomalous diffusion arising from micro-instabilities in a plasma” of fusion interest seemed to have focused first (1962) on high-frequency current drift [34] and grad-B drift [35] ion-cyclotron instabilities lead-

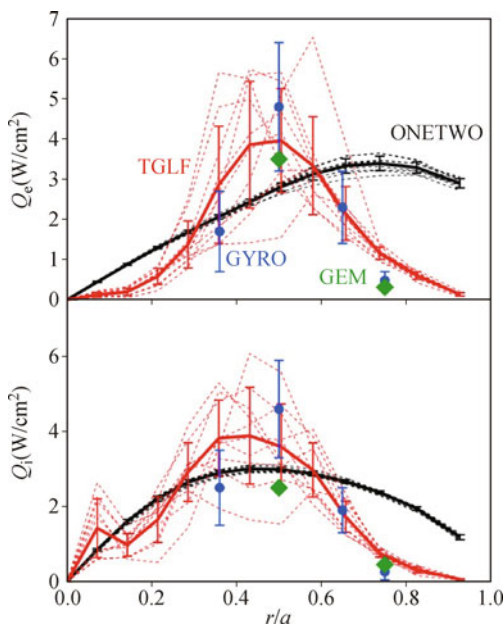


Fig. 1 Comparison of ONETWO power balance calculations (—) of (top) ion and (bottom) electron energy fluxes Q_i and Q_e to predictions from TGLF (---), GYRO (●), and GEM (◆). Reproduced from Ref. [30].

ing to Bohm size and scaled diffusivities $D_B = c_s \rho_s = cT_e/(eB)$. Only later (1965) did the work focus on the low-frequency “universal” (density gradient) diamagnetic drift waves [36], which is now associated with gyrokinetic gyro-Bohm size and scale diffusion as $D_{gB} = D_B \rho_* = (c_s/a) \rho_s^2$. This early work used the time-honored [Landau (1946)] procedure of neglecting the nonlinear term and integrating along unperturbed particle orbits to arrive at the linear dispersion relation as a (possibly truncated) sum of cyclotron harmonics using quasi-neutrality. While unstable high-frequency ion cyclotron modes with low wave numbers ($k_\perp \rho \leq 1$) are not generally thought to be the main cause of or even make a significant contribution to turbulent transport in Tokamaks, the current drift ion cyclotron modes [34] were experimentally observed in the TFR Tokamak [37] in 1978 and shortly thereafter treated in sheared-toroidal Tokamak geometry [38]. Of course, the importance of ion (and electron) cyclotron waves in Tokamak plasma heating and current drive is well established.

The name “cyclokinetics” and the nonlinear formulation were first introduced in Ref. [31]. Ref. [34] treated the high-frequency current driven ion cyclotron modes, and Refs. [35, 36] were among the first to treat low-frequency drift modes in linear electrostatic 6D kinetics which integrated over the gyro-phase. The work in Refs. [32, 39] was the first to present the numerical simulation of nonlinear cyclokinetic theory for ions. That work was also the first to completely solve the ion gyro-phase motion in a nonlinear turbulence system. The numerical method proposed in Refs. [32, 39] is likely to be useful for designing a more comprehensive and physically realistic 6D Eulerian kinetic simulation code.

In Section 1, a brief introduction of the background and history of plasma transport is given, both from the theoretical and experimental perspectives, emphasizing that the L-mode near-edge short-fall problem might be attributed to the breakdown of the gyrokinetic theory. In Section 2, the new theory of cyclokinetics is introduced, in two forms: (i) cyclokinetic equations in the cyclotron harmonic form (CKinCH) and (ii) cyclokinetic equations in the Fourier harmonic form (CKinFH). In Section 3, the newly developed cyclokinetic code rCYCLO is introduced, and the numerical methods for solving the cyclokinetic problem are also introduced. The important verification of incremental entropy conservation and the grid convergence are also verified in this chapter. In Section 4, the cyclokinetic simulation results are presented and the analysis of the gyrokinetic theory breakdown is provided. Finally, the short-fall issue is discussed in Section 5.

2 Cyclokinetics

Since the six-dimensional (6D) cyclokinetic simulation is computationally too expensive, for simplifying the exposition and improving the simulation efficiency a four-dimensional (4D) $[k_x, k_y, \mu, \alpha]$ reduced nonlinear cyclokinetic model was developed by Waltz and Zhao [31]. k_x, k_y are the Fourier transform wavenumbers of the cross-field space positions x, y . μ is the magnetic moment, and α is the ion gyro-phase. The two-dimensional (2D) $[k_z, v_z]$ parallel motion is suppressed for simplicity. By comparing the 4D $[k_x, k_y, \mu, \alpha]$ cyclokinetic simulations with the corresponding three-dimensional (3D) $[k_x, k_y, \mu]$ gyrokinetic simulations, the rCYCLO code can quantitatively test the breakdown of gyrokinetics and gyro-averaging at a sufficiently high turbulence level and sufficiently low relative ion cyclotron frequency Ω^* , where $\Omega^* = 1/\rho^*$ and ρ^* is the relative ion gyro-radius. Cyclokinetics dynamically follows the high-frequency gyro-motion with no averaging over the gyro-phase α . No approximation is made for the $E \times B$ nonlinearity. Only the electrostatic perturbations in a local flux-tube geometry are considered as shown in Fig. 3, with a shear-less B -field decreasing in the radial x direction. This produces a grad- B drift in the y direction. The ion density and temperature gradients are fixed. The electrons are treated by using either the non-adiabatic electron model or a collisional drift wave (CDW) combined with the resistive-g mode fluid model. Cyclokinetics nonlinearly couples the toroidally (grad- B) driven ion temperature gradient (ITG) modes and the CDW modes to the ion cyclotron (IC) modes.

The δf formulations of gyrokinetics and cyclokinetics are limited to *local* micro-turbulence on the cross-field wavelength scale of turbulent eddies $(1-10)\rho_s$ which are much smaller than the length scales of the density and temperature profiles represented by a (the typical minor radius of a Tokamak); hence the “rho-star” parameter $\rho_* = \rho_s/a$ is typically below a few percent. The relative ion cyclotron frequency is $\Omega^* = 1/\rho^* \sim 100$, and cannot be scaled away in the non-zero cyclotron harmonic equations; thus, cyclokinetic diffusivity breaks the local gyro-Bohm diffusivity scaling. Because unstable high-frequency cyclotron harmonics can provide an additional channel to tap the free energy in the plasma gradient, cyclokinetics can be expected to exhibit larger (perhaps some way toward Bohm-sized) diffusion. The positive and negative cyclotron modes will beat together, driving (or possibly damping) the low-frequency drift wave turbulence. Of course, cyclokinetic simulations will likely be more than 100-fold more expensive, because an Ω^*

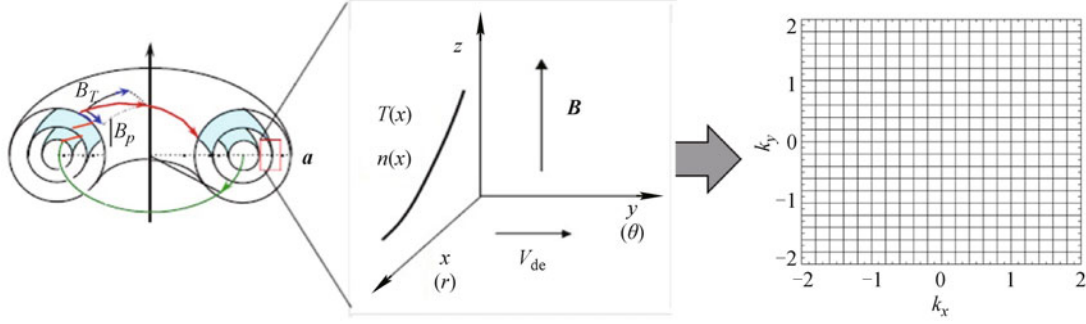


Fig. 3 The geometry of rCYCLO code. A local flux-tube geometry is considered. The parallel motion and variation are ignored. The cross-field space (x, y) are Fourier transformed to wave number space (k_x, k_y) . A shearless B -field decreases in the radial x direction. The ion density and temperature gradients are fixed in x direction.

times smaller time step is required to follow even the lowest cyclotronharmonic.

2.1 Cyclokinetic equations in the gyro-phase angle form

2.1.1 The Boltzmann equation

The Boltzmann equation is the most fundamental description of plasma. Following Ref. [40] the state of plasma can be described by the distribution functions $f_\alpha(t, \mathbf{r}, \mathbf{v})$ that characterize all particle components. These functions describe the density of particles of species α at time t at the point (\mathbf{r}, \mathbf{v}) in the system phase space; the quantity $f_\alpha(t, \mathbf{r}, \mathbf{v})d\mathbf{r}d\mathbf{v}$ then represents the number of particles in the 6D volume element $d\mathbf{r}d\mathbf{v}$. In the simplest case, the plasma consists of electrons and a single ion species ($\alpha = e$ and $\alpha = i$). The plasma behavior is described by a system of kinetic equations, Boltzmann's equations, which describe the temporal evolution of the distribution functions [41–44]:

$$\partial f_\alpha / \partial t + \mathbf{v} \cdot \nabla f_\alpha + (\mathbf{F}_\alpha / m_\alpha) \cdot \partial f_\alpha / \partial \mathbf{v} = C_\alpha. \quad (2.1.1)$$

In the above equation, \mathbf{F}_α is the force on a particle of species α at point \mathbf{r} and velocity \mathbf{v} , m_α is the particle mass, C_α represents the collision associated with the species α . For a particle that carries a charge e_α and is located in an electric field \mathbf{E} and a magnetic field \mathbf{B} :

$$\mathbf{F}_\alpha = e_\alpha(\mathbf{E} + \mathbf{v}/c \times \mathbf{B}). \quad (2.1.2)$$

The distribution function f for the ion species ($\alpha = i$) is

$$\partial f / \partial t + \mathbf{v} \cdot \nabla f + (e/m)[\mathbf{E} + \mathbf{v}/c \times \mathbf{B}] \cdot \partial f / \partial \mathbf{v} = C + S. \quad (2.1.3)$$

where S is the source.

2.1.2 Transport equation

In the presence of the fluctuations of a turbulent electro-

static field $\mathbf{E} \Rightarrow E_x^0 \hat{\mathbf{e}}_x + \delta \mathbf{E}_\perp$, decompose $f = F + \delta f$ where the statistical (or time) averages $\delta \mathbf{E}$ and δf vanish with $\partial F / \partial t \sim 0$. Collisions are likely needed for maintaining the equilibrium background F close to the assumed Maxwellian, but are otherwise ignored in what follows. By averaging Eq. (2.1.3) with respect to the time, the transport equation is obtained:

$$\partial F / \partial t + \nabla \cdot (\mathbf{v} F) + (e/m)(E_x^0 \hat{\mathbf{e}}_x + \mathbf{v}/c \times \mathbf{B}) \cdot \partial F / \partial \mathbf{v} = D + S, \quad (2.1.4)$$

where

$$D = -(e/m)\delta \mathbf{E}_\perp \cdot \partial \delta f / \partial \mathbf{v}_\perp \quad (2.1.5)$$

with the time averaging of D implicit in Eq. (2.1.4). Multiplying Eq. (2.1.4) by $\int d\mathbf{x}^3/V \int d\mathbf{v}^3 v_y [1, mv^2/2]$ and integrating by parts, the box (volume V or flux surface) average turbulent electrostatic $\mathbf{E} \times \mathbf{B}$ radial particle (energy) transport flux is obtained as usual:

$$[\Gamma_x, Q_x] = \int d\mathbf{x}^3/V \int d\mathbf{v}^3 [1, mv^2/2] (c\delta E_y/B) \delta f, \quad (2.1.6)$$

as well as a turbulent heating source [45], which is not accounted for here.

2.1.3 Equation of motion

Unless otherwise noted, we will follow the notation and analysis in Ref. [31] by converting the coordinates $[\mathbf{x}, \mathbf{v}]$ to $[\mathbf{x}', u, \mu, \alpha]$, where $\mathbf{x} = \mathbf{x}'$, $u = \hat{\mathbf{b}} \cdot \mathbf{v}$ is the parallel velocity with $\hat{\mathbf{b}} = \mathbf{B}/B \Rightarrow \hat{\mathbf{e}}_z$, and $\mu = v_\perp^2/(2B)$ is the magnetic moment with the cross-field velocity \mathbf{v}_\perp . What will become the gyro-phase angle α is defined by $\mathbf{v} = u\hat{\mathbf{b}} + \mathbf{v}_\perp$ and $\mathbf{v}_\perp = v_\perp(\hat{\mathbf{e}}_x \cos \alpha + \hat{\mathbf{e}}_y \sin \alpha)$ with $\hat{\mathbf{e}}_y = \hat{\mathbf{b}} \times \hat{\mathbf{e}}_x$, $mv^2/2 = m\mu B + mu^2/2$. Henceforth, the velocity of light will be set to $c \rightarrow 1$. Eq. (2.1.3) can be re-written (again by ignoring the collision term C) as

$$\partial f / \partial t + \Lambda f - \Omega \partial f / \partial \alpha = S, \quad (2.1.7)$$

where (from Ref. [45] Eqs. (12) and (24))

$$\begin{aligned} \Lambda f &= \mathbf{v} \cdot \nabla' f + \dot{u} \partial f / \partial u + \dot{\mu} \partial f / \partial \mu + \dot{\alpha} \partial f / \partial \alpha \\ &= (1/B) \nabla' \cdot (B \mathbf{v} f) + \partial(\dot{u} f) / \partial u \\ &\quad + \partial(\dot{\mu} f) / \partial \mu + \partial(\dot{\alpha} f) / \partial \alpha, \end{aligned} \quad (2.1.8)$$

and (from Ref. [45] Eqs. (16), (17), and (18))

$$\dot{u} = \mathbf{v} \cdot (\nabla \hat{\mathbf{b}}) \cdot \mathbf{v}_\perp + (e/m) E_{//} \Rightarrow 0, \quad (2.1.9)$$

$$\begin{aligned} B \dot{\mu} &= -\mathbf{v} \cdot [\mu \nabla B + u (\nabla \hat{\mathbf{b}}) \cdot \mathbf{v}_\perp] + (e/m) \mathbf{E}_\perp \cdot \mathbf{v}_\perp \\ &\Rightarrow (\mu B/R) v_x + (e/m) E_x^0 v_x + (e/m) \delta \mathbf{E}_\perp \cdot \mathbf{v}_\perp, \end{aligned} \quad (2.1.10)$$

$$\begin{aligned} \dot{\alpha} &= -\mathbf{v} \cdot [(\nabla \hat{\mathbf{e}}_x) \cdot \nabla \hat{\mathbf{e}}_y + (u/v_\perp^2) (\nabla \hat{\mathbf{b}}) \times \hat{\mathbf{b}} \cdot \mathbf{v}_\perp] \\ &\quad + (e/m) \mathbf{E}_\perp \cdot \hat{\mathbf{b}} \times (\mathbf{v}_\perp / v_\perp^2) \\ &\Rightarrow -(e/m) E_x^0 v_y / v_\perp^2 + (e/m) \delta \mathbf{E}_\perp \cdot \hat{\mathbf{b}} \times (\mathbf{v}_\perp / v_\perp^2), \end{aligned} \quad (2.1.11)$$

where the parallel variations and parallel velocity are suppressed, $\nabla_{//} \Rightarrow 0$ and $u \Rightarrow 0$, which kill the associated curvature drifts (absent in a straight B -field). The grad- B drift with $-\nabla_x B/B = 1/R$ is retained, as well as the radial electric field E_x^0 and the turbulent fluctuating field $\delta \mathbf{E}_\perp$. The reduced 4D model has the phase space volume of $\int d\mathbf{x}_\perp^2 \int_0^{2\pi} d\alpha \int_0^\infty B d\mu$.

Subtracting the time average of Eq. (2.1.7) from itself, the equation for the perturbed distribution function is obtained:

$$\begin{aligned} \partial \delta f / \partial t + \mathbf{v}_\perp \cdot \nabla \delta f + [\mu B/R + (e/m) E_x^0] v_x \partial_{B\mu} \delta f \\ - \{ [\mu B/R + (e/m) E_x^0] v_y / v_\perp^2 \\ - \mu B/R (v_y / v_\perp^2) + \Omega \} \partial_\alpha \delta f \\ = -(e/m) \delta \mathbf{E}_\perp \cdot \mathbf{v}_\perp \partial_{B\mu} F - (e/m) \delta \mathbf{E}_\perp \cdot \hat{\mathbf{b}} \times \mathbf{v}_\perp / v_\perp^2 \partial_\alpha F \\ - (e/m) \delta \mathbf{E}_\perp \cdot \mathbf{v}_\perp \partial_{B\mu} \delta f \\ - (e/m) \delta \mathbf{E}_\perp \cdot \hat{\mathbf{b}} \times \mathbf{v}_\perp / v_\perp^2 \partial_\alpha \delta f. \end{aligned} \quad (2.1.12)$$

In order for the background equilibrium F to be the stationary solution of Eq. (2.1.3), it must be a function of the three invariants of Eq. (2.1.3), which are $[mv_\perp^2/2, x + v_y/\Omega, y - v_x/\Omega]$, with the third precluded so as to obtain no y -dependence in the radial flux surface. However, F should have radial x -gradients, which brings in the second invariant. Hence, F is a Maxwellian drifting in the y -direction. Take $F = P_{nT} P_T P_B n_0 F_M$, where the Maxwellian distribution is $F_M = [1/(\pi v_i^{th2})] \exp(-m\mu B/T_i)$, T_i is the ion temperature, $P_{nT} = \exp[-(1/L_n - 1/L_{T_i})(x + v_y/\Omega)]$, $P_T = \exp[-(m\mu B/T_i L_{T_i})(x + v_y/\Omega)]$, and $P_B =$

$\exp[-(m\mu B/T_i R)(x + v_y/\Omega)]$. Eq. (2.1.12) is not clearly Lorenz frame-invariant with respect to $E_x^0 \hat{\mathbf{e}}_x \times B \hat{\mathbf{e}}_z$ drifts in the y -direction. However, a simple shift of the velocity space variable $\mathbf{v}_\perp = v_\perp (\hat{\mathbf{e}}_x \cos \alpha + \hat{\mathbf{e}}_y \sin \alpha) \Rightarrow v_E \hat{\mathbf{e}}_y + v_\perp (\hat{\mathbf{e}}_x \cos \alpha + \hat{\mathbf{e}}_y \sin \alpha)$, where $v_E = E_x^0/B$, removes E_x^0 in both Eqs. (2.1.3), (2.1.4), and Eq. (2.1.12) transforms $\partial \delta f / \partial t \Rightarrow [\partial \delta f / \partial t - v_E \nabla_y \delta f]$, which displays the Doppler rotation Lorentz invariance. Fourier transforming in the cross-field direction (x, y) to (k_x, k_y) the k -component of the fluctuating electric field is $\delta \mathbf{E}_{\perp k} = -i \mathbf{k} \delta \phi_k$.

2.1.4 Cyclokinetic equations in gyro-phase angle form

The simulation box (x, y) is a small symmetric rectangle with side equal to L , satisfying $\rho_s \ll L \ll a$. The parameter ρ_s is the ion gyro-radius associated with ion sound speed, and a is the Tokamak minor radius. The straight and shear-less magnetic field varies only in the x direction $B(x) = B[1 - (x + r)/R]$. The variable x represents the radial position with $x = 0$ at the center of the box, R is the Tokamak major radius, and r is the minor radius of the flux tube. Since no trapped particles are considered, the value of the local inverse aspect ratio r/R does not enter in this model. After straightforward manipulation of the linear F term on the RHS of Eq. (2.1.12), the nonlinear non-conservative form of the ion cyclokinetic equation for δf_k in the gyro-phase angle space is obtained:

$$\begin{aligned} \partial \delta f_k / \partial t - i v_E k_y \delta f_k - i v_d k_y \delta g_k + i \mathbf{v}_\perp \cdot \mathbf{k}_\perp \delta g_k - \Omega \partial_\alpha \delta g_k \\ = -i \omega_*^{nT} (n_0 F_M) e \delta \phi / T_e \\ + \sum_{k_1} (e/m) [\delta \phi_{k_1} i \mathbf{k}_1 \cdot \mathbf{v}_\perp \partial_{B\mu} \delta f_{k_2} \\ + \delta \phi_{k_1} i \mathbf{k}_1 \cdot \hat{\mathbf{b}} \times (\mathbf{v}_\perp / v_\perp^2) \partial_\alpha \delta f_{k_2}], \end{aligned} \quad (2.1.13)$$

where $\delta f_k = \delta g_k - (n_0 F_M) e \delta \phi_k / T_i$ with the non-adiabatic part δg_k . The quantity $\mathbf{k}_\perp = k_\perp [\cos \beta \hat{\mathbf{e}}_x + \sin \beta \hat{\mathbf{e}}_y]$ is the cross-field wave-number vector in Cartesian coordinates with $\hat{\mathbf{e}}_y = \hat{\mathbf{e}}_z \times \hat{\mathbf{e}}_x$, $\hat{\mathbf{e}}_z = \hat{\mathbf{b}} = \mathbf{B}/B$, and β is the wave angle. The subscript \perp of the wave-number vector is ignored for convenience, because the parallel direction is reduced. The three-wave interaction requires $\mathbf{k}_2 = \mathbf{k} - \mathbf{k}_1$. T_e is the electron temperature. n_0 is the unperturbed ion density. $\omega_*^{nT} = [T_e/(eB)] k_y \{1/L_n + [(m\mu B/T_i) - 1]/L_{T_i}\}$ is the density gradient and temperature gradient drift frequency. $P_{nT} P_T P_B = \exp\{-(1/L_n - 1/L_{T_i}) + (m\mu B/T_i)(1/L_{T_i} + 1/R)(x + v_y/\Omega)\}$ has been set to unity (after taking the $[\partial_{B\mu}, \partial_\alpha]$ velocity derivatives) to suppress any exponential radial profile variation, which would be incon-

sistent with local homogeneous turbulence and the k_x -transform.

2.1.5 Normalization

At this point (and henceforth), it is convenient to work in gyro-Bohm units. The primary normalized cyclokinetic equation in the gyro-phase angle space (Eq. (2.1.13)) can be re-written as

$$\begin{aligned} D\delta\hat{f}_k/D\hat{t} - i\hat{\omega}_k^E\delta\hat{f}_k - i\hat{\omega}_k^d\delta\hat{g}_k + i\hat{\mathbf{v}}_\perp \cdot \hat{\mathbf{k}}\Omega_*\delta\hat{g}_k - \Omega_*\partial_\alpha\delta\hat{g}_k \\ = -i\hat{\omega}_{*k}^T\delta\hat{\phi}_k(n_0F_M) \\ + \sum_{k1}[(T_e/T_i)\delta\hat{\phi}_{k1}i\hat{\mathbf{k}}_1 \cdot \hat{\mathbf{v}}_\perp\partial_\mu\delta\hat{f}_{k2} \\ + \delta\hat{\phi}_{k1}i\hat{\mathbf{k}}_1 \cdot \hat{\mathbf{b}} \times \hat{\mathbf{v}}_\perp/\hat{v}_\perp^2\partial_\alpha\delta\hat{f}_{k2}], \end{aligned} \quad (2.1.14)$$

where $\delta\hat{g}_k(\hat{\mu}, \alpha) = \delta\hat{f}_k(\hat{\mu}, \alpha) + (T_e/T_i)\delta\hat{\phi}_k n_0 F_M(\hat{\mu})$ represents the non-adiabatic part of the distribution function. The variables are normalized to the gyro-Bohm units. Macro-lengths are scaled to the Tokamak minor radius a , cross-field micro-turbulence lengths are scaled to the sound speed ion gyro-radius ρ_s , velocities are scaled to the ion sound speed c_s , time is scaled to a/c_s , and ion velocity is scaled to the ion thermal speed $v_i^{th} = \sqrt{2T_i/m_i}$. The ion sound speed is defined by $c_s = \sqrt{T_e/m_i}$, with $\rho_s = c_s/\Omega$, where $\Omega = eB/(m_i c)$ is the ion gyro-frequency. The wavenumber, the time, and the magnetic moment are normalized as $\hat{k} = k\rho_s$, $\hat{t} = t(c_s/a)$, and $\hat{\mu} = (v_\perp/v_i^{th})^2$ respectively. The perturbed ion distribution function, electric potential, and Maxwell's distribution function are normalized as $\delta\hat{f}_k = (\delta f_k T_i/m_i)/\rho^*$, $\delta\hat{\phi}_k = (e\delta\phi_k/T_e)/\rho^*$, and $F_M(\hat{\mu}) = e^{-\hat{\mu}}/2\pi$ respectively, where $\rho^* = \rho_s/a$ is the relative ion gyro-radius. $\hat{\omega}_k^E = \hat{v}^E \hat{k}_y$ is the Doppler $E \times B$ rotation frequency. $\hat{\omega}_k^d = 2\hat{k}_y(T_i/T_e)\hat{\mu}(a/R)$ is the grad- B drift frequency. The factor 2 is added here to compensate for the curvature drive from the suppressed parallel direction. $\hat{\mathbf{v}}_\perp \cdot \hat{\mathbf{k}}_\perp = k\rho\cos(\alpha - \beta)$, and $\rho = v_\perp/\Omega$ is the ion gyro-radius. $\Omega_*\partial_\alpha\delta\hat{g}_k$ represents the linear high-frequency ion gyro-motion. $\hat{\omega}_{*k}^T = \hat{k}_y[(a/L_n) + (a/L_{Ti})(\hat{\mu} - 1)]$ is the density and temperature gradient drive frequency for the drift waves. Artificial damping at high and low k is incorporated into time derivative operator $D/D\hat{t} = \partial/\partial\hat{t} + \mu_{HK}\hat{k}^4 + \mu_{LK}/\hat{k}^2$. μ_{HK} and μ_{LK} are constants. $\mu_{HK}\hat{k}^4$ represents the damping of high- k modes, which allows turbulence energy to escape to short wavelength modes where it is physically damped by collisions. μ_{LK}/\hat{k}^2 represents the damping of low- k modes. It physically represents the neglected magnetic shear damping which makes the low- k modes slightly stable. This allows the low- k modes to saturate the inverse cascade energy from the higher k driving modes. The large factor $\Omega^* = 1/\rho^*$ is

the relative ion cyclotron frequency, which ranges from 10 to 1000, with 50 to 100 being the typical physical values of interest. We set $n_0 \equiv 1$ in the units of density n_e , which implies $n_i = n_e$. The velocity space integration of the 2D Maxwell's ion distribution function is $\oint d\alpha \int_0^\infty d\hat{\mu} F_M(\hat{\mu}) = 1$, where the parallel velocity has been suppressed. The perturbed potential and the distribution function satisfy the realistic condition $\delta\hat{\phi}_{-k} = \delta\hat{\phi}_k^*$, $\delta\hat{f}_{-k} = \delta\hat{f}_k^*$. Note that cyclokinetics does not assume $\delta f/F \ll 1$, where F is the equilibrium background distribution.

It is useful to note that the nonlinear coupling in Eq. (2.1.14) does not (explicitly) have the familiar “ $\hat{\mathbf{k}}_1 \times \hat{\mathbf{k}}_2$ ” form ($\sum_{k1} \Omega_* \hat{\mathbf{e}}_z \cdot \hat{\mathbf{k}}_1 \times \hat{\mathbf{k}}_2 \delta\hat{\phi}_{k1} \delta\hat{f}_{k2}$) expected of the simple nonlinear $E \times B$ motion in which self-interaction “ $\hat{\mathbf{k}}_1 = \pm\hat{\mathbf{k}}_2$ ” is precluded. Nevertheless, after applying the conservative property Eq. (2.1.15) to Eq. (2.1.14), it is straightforward to prove that the nonlinearity conserves the total incremental entropy:

$$(T_e/T_i)\partial_\mu\hat{\mathbf{k}}_1 \cdot \hat{\mathbf{v}}_\perp + \partial_\alpha\hat{\mathbf{k}}_1 \cdot \hat{\mathbf{b}} \times \hat{\mathbf{v}}_\perp/\hat{v}_\perp^2 = 0. \quad (2.1.15)$$

The incremental entropy is defined as

$$S = \sum_k \oint d\alpha \int_0^\infty d\hat{\mu} (\delta\hat{f}_k^* \delta\hat{f}_k). \quad (2.1.16)$$

The radial ion particle and energy fluxes in the gyro-Bohm units of $n_0 c_s \rho^{*2}$ and $T_e n_0 c_s \rho^{*2}$ are

$$\begin{aligned} [\hat{I}, \hat{Q}^\perp] = Re \oint d\alpha \int_0^\infty d\hat{\mu} \sum_k [1, (T_i/T_e)\hat{\mu}] \\ \cdot i\hat{k}_y \delta\hat{\phi}_k^* [\delta\hat{g}_k(\hat{\mu}, \alpha)/n_0], \end{aligned} \quad (2.1.17)$$

where Re means that only the real part is retained. $\delta\hat{g}_k$ indicates that the transport is proportional to the non-adiabatic perturbed distribution function. The diffusivities are defined as fluxes divided by gradients:

$$[\hat{D}, \hat{\chi}] = [\hat{I}, \hat{Q}^\perp]/[a/L_n, a/L_{Ti}]. \quad (2.1.18)$$

It is difficult to correctly simulate Eq. (2.1.14), because it is difficult to ensure correct temporal evolution of the stiff α -derivative term $\Omega_*\partial_\alpha\delta\hat{g}_k$. It is better to transform α to a harmonic space so as to replace the derivative operator by the harmonic number identity. There are two types of harmonic transforms: cyclotron harmonics and Fourier harmonics. Nonlinear cyclokinetic equations in the cyclotron harmonic representation (CKinCH) were introduced in Ref. [39]. Cyclokinetic equations with Fourier harmonics (CKinFH) were introduced in Ref. [32]. The CKinCH nonlinear simulations are considerably more computationally expensive than the CKinFH simulations, but it is easier to analytically identify

the CKinCHwith gyrokinetics.

2.1.6 The Poisson equation

The quasi-neutrality relation determining $\delta\hat{\phi}_k$ is expressed in the Poisson equation:

$$\delta\hat{\phi}_k = \frac{\oint d\alpha \int_0^\infty d\hat{\mu} \delta f_k(\hat{\mu}, \alpha)/n_0 - C_{DW} \cdot \delta\hat{n}_k^e}{(1 - C_{DW})R_k + C_{DW} \cdot (\hat{\lambda}_D^2 \hat{k}^2)}, \quad (2.1.19)$$

where $\hat{\lambda}_D \ll 1$ is the Debye length in the units of ρ_s , C_{DW} is the control parameter for determining the electron model, $C_{DW} = [0, 1]$ for the [near adiabatic electron, collisional drift wave electron] model, $R_k = \lambda_k - i\delta_k$ represents the electron response function, and δ_k is the electron non-adiabatic parameter. $\delta_1 > 0$ will add unstable electron drift waves to the unstable “toroidal” ITG modes. Positive δ_k drives instability to all except the $\hat{k}_y = 0$ modes. $\delta\hat{n}_k^e = (\delta n_k^e/n_0)/\rho^*$ is the normalized perturbed electron density, and $\delta\hat{n}_k^i = \oint d\alpha \int_0^\infty d\hat{\mu} \delta f_k(\hat{\mu}, \alpha)/n_0$ is the normalized perturbed ion density. The electron equations of motion are given in Section 2.5.

2.2 Cyclokinetic equations in the cyclotron harmonic form

2.2.1 Cyclotron harmonic transformation

To make a clear connection between cyclokinetic and gyrokinetics and for easier quantification of the gyrokinetics breakdown conditions, Eqs. (2.1.14), (2.1.17) and (2.1.19) are re-formulated in terms of the cyclotron harmonics. The cyclotron harmonic $\delta\hat{G}_k^n(\hat{\mu})$ is defined by introducing an integrating factor on $\delta\hat{g}_k(\hat{\mu}, \alpha)$ (and similarly on $\delta\hat{f}_k(\hat{\mu}, \alpha)$):

$$\begin{aligned} & \delta\hat{g}_k(\hat{\mu}, \alpha) \exp[-ik\rho \sin(\alpha - \beta)] \\ &= \sum_{n=-N_\alpha+1}^{n=N_\alpha-1} \delta\hat{G}_k^n(\hat{\mu}) \exp[in(\alpha - \beta)]. \end{aligned} \quad (2.2.1)$$

In order to formulate numerically efficient equations, a finite expansion in the gyro-phase space is applied here instead of an infinite expansion in Ref. [31]. $n = -N_\alpha + 1, \dots, 0, \dots, N_\alpha - 1$ is the harmonic number with respect to α . The cyclotron harmonics are the linearly uncoupled “normal modes” of cyclokinetics. The perturbed distribution function satisfies the reality condition $\delta\hat{F}_{-k}^{-n} = (-1)^n [\delta\hat{F}_k^n]^*$ and $\delta\hat{G}_{-k}^{-n} = (-1)^n [\delta\hat{G}_k^n]^*$.

Using $\oint d\alpha/(2\pi) \exp[ik\rho \sin(\alpha - \beta) - in(\alpha - \beta)] = J_n(k\rho)$, where $J_n(k\rho)$ is the Bessel function, Eq. (2.1.14) can be re-written in terms of the cyclotron harmonics as

(by henceforth suppressing the Doppler $E \times B$ rotation frequency $\hat{\omega}_k^E$):

$$\begin{aligned} & D\delta\hat{F}_k^n/D\hat{t} - i\hat{\omega}_k^d \delta\hat{G}_k^n - in\Omega_* \delta\hat{G}_k^n \\ &+ J_n(k\rho) \delta\hat{\phi}_k i\hat{\omega}_{*k}^{nT} n_0 F_M(\hat{\mu}) \\ &= \oint d\alpha/(2\pi) \exp[-in(\alpha - \beta) + ik\rho \sin(\alpha - \beta)] N L_k(\hat{\mu}, \alpha) \\ &= \partial_\mu N L_k^n(\hat{\mu}) + \partial_\alpha N L_k^n(\hat{\mu}), \end{aligned} \quad (2.2.2)$$

where

$$\begin{aligned} \partial_\mu N L_k^n(\hat{\mu}) &= \sum_{n'} \sum_{k1} \delta\hat{\phi}_{k1} \oint \exp[-in(\alpha - \beta) \\ &+ ik\rho \sin(\alpha - \beta) + in'(\alpha - \beta_2) \\ &- ik_2\rho \sin(\alpha - \beta_2)] [ik_1\rho \cos(\alpha - \beta_1)] (T_e/T_i) \\ &\cdot [\partial_{\hat{\mu}} \delta\hat{F}_{k2}^{n'} - \delta\hat{F}_{k2}^{n'} ik_2\rho \sin(\alpha - \beta_2)/(2\hat{\mu})] [d\alpha/(2\pi)], \end{aligned} \quad (2.2.3)$$

and

$$\begin{aligned} \partial_\alpha N L_k^n(\hat{\mu}) &= \sum_{n'} \sum_{k1} \delta\hat{\phi}_{k1} \oint \exp[-in(\alpha - \beta) \\ &+ ik\rho \sin(\alpha - \beta) + in'(\alpha - \beta_2) \\ &- ik_2\rho \sin(\alpha - \beta_2)] [-ik_1\rho \sin(\alpha - \beta_1)/\hat{v}_\perp^2] \\ &\cdot [in' - ik_2\rho \cos(\alpha - \beta_2)] \delta\hat{F}_{k2}^{n'} [d\alpha/(2\pi)], \end{aligned} \quad (2.2.4)$$

where $\delta\hat{F}_k^n(\hat{\mu}) = \delta\hat{G}_k^n(\hat{\mu}) - J_n(k\rho) \delta\hat{\phi}_k (T_e/T_i) n_0 F_M(\hat{\mu})$ and $N L_k(\hat{\mu}, \alpha)$ refers to the nonlinear terms on the RHS of Eq. (2.1.14). $\partial_\mu N L_k^n(\hat{\mu})$ and $\partial_\alpha N L_k^n(\hat{\mu})$ on the RHS of Eq. (2.2.2) correspond to the $\partial_{\hat{\mu}}$ and ∂_α derivative terms on the RHS of Eq. (2.1.14). $\sum_{n'}$ represents $\sum_{n'=-N_\alpha+1}^{n'=N_\alpha-1}$.

Following Eqs. (2.1.17) and (2.2.1), the radial transport fluxes are:

$$\begin{aligned} [\hat{I}, \hat{Q}^\perp] &= Re 2\pi \int_0^\infty d\hat{\mu} \sum_k \sum_n [1, (T_i/T_e) \hat{\mu}] \\ &\cdot i\hat{k}_y \delta\hat{\phi}_k^* J_n(k\rho) \delta\hat{G}_k^n(\hat{\mu})/n_0, \end{aligned} \quad (2.2.5)$$

which again recovers the gyrokinetic description when truncated at $n = 0$.

2.2.2 Linear dispersion relation

The linear dispersion relation is explored, before unpacking the nonlinear terms. Since the collisional drift wave electron model is too complicated to analyze the linear dispersion relation, the electron is described by using the non-adiabatic model, by setting $C_{DW} = 0$ in Eq. (2.1.19). The quasi-neutrality relation, Eq. (2.1.19), becomes:

$$\begin{aligned}
 n_0 \delta \hat{\phi}_k(\lambda_k - i \hat{k}_y \delta_1) &= -n_0 \delta \hat{\phi}_k(T_e/T_i) + \oint d\alpha \int_0^\infty d\hat{\mu} \delta \hat{g}_k(\hat{\mu}, \alpha) \\
 &= -n_0 \delta \hat{\phi}_k(T_e/T_i) + \sum_n 2\pi \int_0^\infty d\hat{\mu} J_n(k\rho) \delta \hat{G}_k^n(\hat{\mu}) \\
 &= -n_0 \delta \hat{\phi}_k(T_e/T_i) [1 - \sum_n \Gamma_n(b)] \\
 &\quad + \sum_n 2\pi \int_0^\infty d\hat{\mu} J_n(k\rho) \delta \hat{F}_k^n(\hat{\mu}), \quad (2.2.6)
 \end{aligned}$$

where $J_{-n} = (-1)^n J_n$ is used, and Eq. (6.615) in p.710 of Ref. [46] is used to obtain the modified Bessel function (I_n) form $\Gamma_n(b) = \exp(-b) I_n(b)$, where $b = (k\rho)^2/2 = (T_i/T_e) \hat{k}^2$. The first term on the RHS can be called the (perturbed) ion polarization density with the second called the density of gyro-centers. From the identity (Eq. (8.536) in p. 980 of Ref. [46]) $\sum_n J_n^2 = 1 \Rightarrow [1 - \sum_n \Gamma(b)] = 0$, polarization density formally vanishes if all cyclotron harmonics $[-\infty < n < \infty]$ are retained (compared with Eq. (2.1.19), which has no polarization density). From the linear LHS side of Eq. (2.2.2), $\delta \hat{G}_k^n = n_0 F_M J_n(k\rho) \delta \hat{\phi}_k [\hat{\omega}_{*k}^{nT} + \hat{\omega}(T_e/T_i)]/(\hat{\omega} + \hat{\omega}_k^d + n\Omega)$, and the intermediate Eq. (2.2.6), the linear dispersion relation is written as

$$\begin{aligned}
 [\lambda_k - i \hat{k}_y \delta_1] &= -(T_e/T_i) \\
 &\quad + \sum_n 2\pi \int_0^\infty d\hat{\mu} J_n^2(k\rho) F_M(\hat{\mu}) [\hat{\omega}_{*k}^{nT}(\hat{\mu}) \\
 &\quad + \hat{\omega}(T_e/T_i)]/[\hat{\omega} + \hat{\omega}_k^d(\hat{\mu}) + n\Omega_*]. \quad (2.2.7)
 \end{aligned}$$

For the dissipative electron drive $i\delta_k = 0$ (here $\delta_k = \hat{k}_y \delta_1$), the $\hat{k}_y \neq 0$ dispersion relation has both a low-frequency drift wave and high-frequency ion cyclotron reactive toroidal ITG modes driven by a/L_{T_i} and stabilized by a/L_{n_i} ; however, the ITG ion cyclotron modes are neutrally stable without unphysically large values of a/L_{T_i} . When the $\hat{\mu}$ dependence of $\hat{\omega}_{*k}^{nT}$ and $\hat{\omega}_k^d$ is suppressed, $2\pi \int_0^\infty d\hat{\mu} J_n^2(k\rho) F_M(\hat{\mu}) \Rightarrow \Gamma_n(b)$, e.g., $a/L_{T_i} \Rightarrow 0$ and $a/R \Rightarrow 0$, which of course removes the toroidal ITG instability. For $\delta_k = \hat{k}_y \delta_1 > 0$ and expanding around the resonances $\hat{\omega}_k \sim -n\Omega_*$, the linear dispersion relation becomes:

$$\hat{\omega}_k \sim -n\Omega_* + \Gamma_n(b) [\hat{\omega}_{*k}^n - n\Omega_*(T_e/T_i)]$$

$$\cdot \{1 + (T_e/T_i)[1 - \Gamma_n(b)] - i \hat{k}_y \delta_1\}^{-1}. \quad (2.2.8)$$

The well-known low-frequency “i-delta” electron drift wave driven by density gradients $a/L_{n_i} > 0$ is recovered for $n = 0$. For $n \neq 0$, the $\hat{\omega}_{*k}^n$ term is not significant and the ion cyclotron modes are driven/damped by $i\delta_k$ alone, without a density gradient, as in the Drummond-Rosenbluth current drift ion cyclotron modes [34] with “kinetic” electrons (see Ref. [20] for examples in shear slab and toroidal geometries). As noted, physically the $i\delta_k$ value depends on the frequency of the actual linear mode. It is useful to note that in building a test model for nonlinear gyrokinetic simulations, the growth and damping rates of the low-frequency drift waves can be separately controlled by the ITG temperature gradient a/L_{T_i} and the high-frequency ion cyclotron modes by the δ_1 parameter. There is little linear interaction among the cyclotron harmonics, so they can be treated separately one n at a time.

2.2.3 Nonlinear terms

As noted, the gyrokinetic nonlinearity in Eq. (2.1.14) does not (in an obvious way) have the familiar “ $\hat{k}_1 \times \hat{k}_2$ ” form common to gyrokinetics (and all previously explored 2D (planar) turbulence models) that precludes nonlinear self-interaction. Hence, the focus in unpacking the nonlinear terms $\partial_\mu N L_k^n(\hat{\mu}) + \partial_\alpha N L_k^n(\hat{\mu})$ on the RHS of Eqs. (2.2.3) and (2.2.4) is to isolate the “ $\hat{k}_1 \times \hat{k}_2$ ” from the self-interacting “ $\hat{k}_1 \cdot \hat{k}_2$ ” components. Note that $k\rho \sin(\alpha - \beta) - k_2\rho \sin(\alpha - \beta_2) = \hat{\varepsilon}_z \cdot \hat{\mathbf{k}} \times \hat{\mathbf{v}}_\perp - \hat{\varepsilon}_z \cdot \hat{\mathbf{k}}_2 \times \hat{\mathbf{v}}_\perp = \hat{\varepsilon}_z \cdot \hat{\mathbf{k}}_1 \times \hat{\mathbf{v}}_\perp = k_1\rho \sin(\alpha - \beta_1)$ and $-\hat{k}_1 \hat{k}_2 \sin(\beta_1 - \beta_2) = \hat{\varepsilon}_z \cdot \hat{\mathbf{k}}_1 \times \hat{\mathbf{k}}_2$ with $\hat{k}_1 \hat{k}_2 \cos(\beta_1 - \beta_2) = \hat{\mathbf{k}}_1 \cdot \hat{\mathbf{k}}_2$, and define a phase factor between different wave angles as $\Delta_n'(\beta, \beta_1, \beta_2) \equiv \exp[-in(\beta_1 - \beta) + in'(\beta_1 - \beta_2)]$. The nonlinear terms (2.2.9) and (2.2.10) are obtained after some manipulation of the Bessel function identities.

Eq. (2.2.2), combined with Eq. (2.2.11), is the penultimate result of this section, and is mathematically identical to Eq. (2.1.14). Eq. (2.2.11) is in the non-conservative form, and its conservative form is obtained by applying the crucial identity Eq. (2.1.15) to its nonlinear term. CKinCH with the conservative nonlinear expression is written as (2.2.12).

$$\begin{aligned}
 \partial_\alpha N L_k^n(\hat{\mu}) &= + \sum_{n'} \sum_{k_1} \hat{\varepsilon}_z \cdot \hat{\mathbf{k}}_1 \times \hat{\mathbf{k}}_2 \{J_{-n+n'}(k_1\rho)/2 - [J_{-n+n'+2}(k_1\rho) + J_{-n+n'-2}(k_1\rho)]/4\} \delta \hat{\phi}_{k_1} \delta \hat{F}_{k_2}^{n'} \Delta_n'(\beta, \beta_1, \beta_2) \\
 &\quad + \sum_{n'} \sum_{k_1} \hat{\mathbf{k}}_1 \cdot \hat{\mathbf{k}}_2 \{[J_{-n+n'+2}(k_1\rho) - J_{-n+n'-2}(k_1\rho)]/(4i)\} \delta \hat{\phi}_{k_1} \delta \hat{F}_{k_2}^{n'} \Delta_n'(\beta, \beta_1, \beta_2) \\
 &\quad + \sum_{n'} \sum_{k_1} (\hat{k}_1/\hat{v}_\perp) \{[J_{-n+n'+1}(k_1\rho) - J_{-n+n'-1}(k_1\rho)]/(2i)\} \delta \hat{\phi}_{k_1} (n' \delta \hat{F}_{k_2}^{n'}) \Delta_n'(\beta, \beta_1, \beta_2), \quad (2.2.9)
 \end{aligned}$$

$$\begin{aligned}
 \partial^\mu NL_k^n(\hat{\mu}) = & + \sum_{n'} \sum_{k1} \hat{\varepsilon}_z \cdot \hat{\mathbf{k}}_1 \times \hat{\mathbf{k}}_2 \{ J_{-n+n'}(k_1\rho)/2 + [J_{-n+n'+2}(k_1\rho) + J_{-n+n'-2}(k_1\rho)]/4 \} \delta\hat{\phi}_{k1} \delta\hat{F}_{k2}^{n'} \Delta_n^{n'}(\beta, \beta_1, \beta_2) \\
 & - \sum_{n'} \sum_{k1} \hat{\mathbf{k}}_1 \cdot \hat{\mathbf{k}}_2 \{ [J_{-n+n'+2}(k_1\rho) - J_{-n+n'-2}(k_1\rho)]/(4i) \} \delta\hat{\phi}_{k1} \delta\hat{F}_{k2}^{n'} \Delta_n^{n'}(\beta, \beta_1, \beta_2) \\
 & - \sum_{n'} \sum_{k1} (\hat{k}_1/\hat{v}_\perp) \{ [J_{-n+n'+1}(k_1\rho) + J_{-n+n'-1}(k_1\rho)]/(2i) \} \delta\hat{\phi}_{k1} (2\hat{\mu}\partial_{\hat{\mu}}\delta\hat{F}_{k2}^{n'}) \Delta_n^{n'}(\beta, \beta_1, \beta_2). \quad (2.2.10)
 \end{aligned}$$

Eq. (2.2.11) is obtained by adding (2.2.9) to (2.2.10),

$$\begin{aligned}
 \partial_\alpha NL_k^n(\hat{\mu}) + \partial^\mu NL_k^n(\hat{\mu}) = & + \sum_{n'} \sum_{k1} \hat{\varepsilon}_z \cdot \hat{\mathbf{k}}_1 \times \hat{\mathbf{k}}_2 [J_{n-n'}(k_1\rho)] \delta\hat{\phi}_{k1} \delta\hat{F}_{k2}^{n'} \Delta_n^{n'}(\beta, \beta_1, \beta_2) \\
 & + \sum_{n'} \sum_{k1} (\hat{k}_1/\hat{v}_\perp) \{ [J_{n-n'+1}(k_1\rho) - J_{n-n'-1}(k_1\rho)]/(2i) \} \delta\hat{\phi}_{k1} (n' \delta\hat{F}_{k2}^{n'}) \Delta_n^{n'}(\beta, \beta_1, \beta_2) \\
 & + \sum_{n'} \sum_{k1} (\hat{k}_1/\hat{v}_\perp) \{ [J_{n-n'+1}(k_1\rho) + J_{n-n'-1}(k_1\rho)]/(2i) \} \delta\hat{\phi}_{k1} (2\hat{\mu}\partial_{\hat{\mu}}\delta\hat{F}_{k2}^{n'}) \Delta_n^{n'}(\beta, \beta_1, \beta_2). \quad (2.2.11)
 \end{aligned}$$

$$\begin{aligned}
 D\delta\hat{F}_k^n/D\hat{t} - i\hat{\omega}_k^d \delta\hat{G}_k^n - in\Omega_* \delta\hat{G}_k^n + J_n(k\rho) \delta\hat{\phi}_k i\hat{\omega}_{*k}^{nT} n_0 F_M(\hat{\mu}) \\
 = \sum_{n'} \sum_{k1} \hat{b} \cdot \hat{\mathbf{k}}_1 \times \hat{\mathbf{k}}_2 [J_{n-n'}(k_1\rho)] \delta\hat{\phi}_{k1} \delta\hat{F}_{k2}^{n'} \Delta_n^{n'}(\beta, \beta_1, \beta_2) \\
 + \sum_{n'} \sum_{k1} (\hat{k}_1/\hat{v}_\perp) \{ [J_{n-n'+1}(k_1\rho) - J_{n-n'-1}(k_1\rho)]/(2i) \} \delta\hat{\phi}_{k1} (n \delta\hat{F}_{k2}^{n'}) \Delta_n^{n'}(\beta, \beta_1, \beta_2) \\
 + \sum_{n'} \sum_{k1} \delta\hat{\phi}_{k1} (T_e/T_i) \partial_{\hat{\mu}} \{ [J_{n-n'+1}(k_1\rho) + J_{n-n'-1}(k_1\rho)] (\hat{k}_1 \hat{v}_\perp) \delta\hat{F}_{k2}^{n'}/(2i) \} \Delta_n^{n'}(\beta, \beta_1, \beta_2). \quad (2.2.12)
 \end{aligned}$$

After some careful algebra, the conservative and non-conservative forms are found to be equivalent as required. Notice that the nonlinear coupling coefficient on the last two lines of the nonlinear term is enhanced by $1/\hat{v}_\perp$ at low velocities.

2.2.4 Incremental entropy

In rCYCLO code, the nonlinear term is calculated by adding the conservative form with the equivalent non-conservative forms of nonlinear terms and dividing by 2. This operation cancels any numerical errors from the μ -derivative operator (described in Ref. [32]) in the nonlinear conservation of incremental entropy. The incremental entropy of CKinCH is defined as

$$S = \sum_k \oint d\alpha \int_0^\infty d\hat{\mu} (\delta\hat{f}_k^* \delta\hat{f}_k)$$

$$= 2\pi \int_0^\infty d\hat{\mu} \sum_k \sum_n (\delta\hat{F}_k^n)^* \delta\hat{F}_k^n. \quad (2.2.13)$$

Using the conservative nonlinear expression in Eq. (2.2.11) together with the non-conservative expression in Eq. (2.2.11), it is straightforward to prove the CKinCH nonlinear entropy conservation. Numerical conservation of nonlinear incremental entropy is a crucial test of any turbulence simulation code (e.g., see Ref. [47] for the case of the GYRO code). Without accurate conservation, there may be no nonlinear saturation. The discretization of the derivative operator $\partial_{\hat{\mu}}$ is designed to ensure the conservation of the incremental entropy, as discussed in Section 3.

2.2.5 The Poisson equation

The Poisson equation for the CKinCH is given as

$$\delta\hat{\phi}_k = \frac{\sum_n 2\pi \int d\hat{\mu} J_n(k\rho) \delta\hat{F}_k^n(\hat{\mu})/n_0 - C_{DW} \cdot \delta\hat{n}_k^e}{(T_e/T_i)[1 - \sum_n 2\pi \int d\hat{\mu} F_M(\hat{\mu}) J_n^2(k\rho)] + (1 - C_{DW})R_k + C_{DW} \cdot (\hat{\lambda}_D^2 \hat{k}^2)}. \quad (2.2.14)$$

The polarization density formally vanishes when all cyclotron harmonics are retained:

$$[1 - \sum_n 2\pi \int d\hat{\mu} F_M(\hat{\mu}) J_n^2(k\rho)] \rightarrow 0|_{n \rightarrow \pm\infty}.$$

2.3 The gyrokinetic equation in the Fourier harmonic form

2.3.1 The Fourier transformation

After straightforwardly expanding $\delta \hat{f}_k(\hat{\mu}, \alpha)$ in Eq. (2.1.14) with finite (or discrete) Fourier harmonics $\delta \hat{f}_k(\hat{\mu}, \alpha) = \sum_{n=-N_\alpha+1}^{N_\alpha-1} \delta \hat{F}_k^n(\hat{\mu}) \exp(in\alpha)$, the 4D gyrokinetic equation is obtained in the Fourier harmonic form given by Eq. (2.3.1), where $n = -N_\alpha + 1, \dots, 0, \dots, N_\alpha - 1$ is the harmonic number with respect to α . The corresponding inverse Fourier transform is: $\delta \hat{F}_k^n(\hat{\mu}) = \frac{1}{2N_\alpha-1} \sum_{m=0}^{m=2N_\alpha-2} \delta \hat{f}_k(\hat{\mu}, \alpha_m) \exp(-in\alpha_m)$, where $\alpha_m = 2\pi m/(2N_\alpha - 1)$.

$$\begin{aligned} D\delta \hat{F}_k^n / D\hat{t} - i\hat{\omega}_k^d \delta \hat{G}_k^n + i(\hat{v}_\perp \hat{k}_1/2) \Omega_* [\exp(-i\beta) \delta \hat{G}_k^{n-1} \\ + \exp(+i\beta) \delta \hat{G}_k^{n+1}] - \Omega_* i n \delta \hat{G}_k^n \\ = -i\hat{\omega}_{*k}^T \delta \hat{\phi}_k n_0 F_M(\hat{\mu}) \delta_0^n + {}^{NL} S(\hat{k}, \hat{\mu}, n). \end{aligned} \quad (2.3.1)$$

$\delta \hat{G}_k^n = \delta \hat{F}_k^n + (T_e/T_i) \delta \hat{\phi}_k n_0 F_M(\hat{\mu}) \delta_0^n$ represents the non-adiabatic part of the distribution function, with $\delta_0^n = [0, 1]$ corresponding to $[n \neq 0, n = 0]$. The perturbed distribution functions are linearly coupled and satisfy the reality condition $\delta \hat{F}_{-k}^{-n} = [\delta \hat{F}_k^n]^*$. ${}^{NL} S(\hat{k}, \hat{\mu}, n)$ represents the nonlinear dynamics.

2.3.2 Cyclic boundary condition in the gyro phase space

Since the gyro phase angle space is cyclic $\delta \hat{f}_k(\hat{\mu}, \alpha + 2\pi) = \delta \hat{f}_k(\hat{\mu}, \alpha)$ on $0 \leq \alpha < 2\pi$, its Fourier form $\delta \hat{F}_k^n$ is also cyclic. For a finite harmonic number $n = -N_\alpha + 1, \dots, 0, \dots, N_\alpha - 1$, a cyclic boundary condition at $\alpha = [0, 2\pi]$ is provided by $\delta \hat{F}_k^{-N_\alpha} = \delta \hat{F}_k^{N_\alpha-1}$, $\delta \hat{F}_k^{N_\alpha} = \delta \hat{F}_k^{-N_\alpha+1}$ as demonstrated from the inverse Fourier transform. The derivative operator also requires a Fourier transform $\partial_\alpha \delta \hat{f}_k(\hat{\mu}, \alpha) \Rightarrow i n \delta \hat{F}_k^n(\hat{\mu})$, where $i n(n)$ is the derivative harmonic identity, which is cyclic $i n[n \pm (2N_\alpha - 1)] = i n(n)$ and $i n(n)$ is calculated from $i n(n) = i[n - j(2N_\alpha - 1)]$ when $-N_\alpha + 1 + j(2N_\alpha - 1) \leq n \leq N_\alpha - 1 + j(2N_\alpha - 1)$ with an integer j . Thus, the cyclic boundary condition of the derivative harmonic identity should be $i n(N_\alpha) = i n(-N_\alpha + 1)$ and $i n(-N_\alpha) = i n(N_\alpha - 1)$.

2.3.3 Nonlinear terms

Eq. (2.1.14) is in the non-conservative form, and its conservative form is obtained by applying the crucial identity in Eq. (2.1.15) to Eq. (2.1.14). After the discrete Fourier harmonic transformation, both the conservative and non-conservative forms of the nonlinear dynamics are obtained. The conservative form (2.3.2) is

$$\begin{aligned} {}^{NL}_{Con} S(\hat{k}, \hat{\mu}, n) = \partial_{\hat{\mu}} \sum_{k1} (T_e/T_i) \delta \hat{\phi}_{k1} i(\hat{v}_\perp \hat{k}_1/2) [\exp(-i\beta_1) \delta \hat{F}_{k2}^{n-1} + \exp(+i\beta_1) \delta \hat{F}_{k2}^{n+1}] \\ - \sum_{k1} \delta \hat{\phi}_{k1} i \hat{k}_1 / (2\hat{v}_\perp) n [\exp(-i\beta_1) \delta \hat{F}_{k2}^{n-1} - \exp(+i\beta_1) \delta \hat{F}_{k2}^{n+1}], \end{aligned} \quad (2.3.2)$$

and the non-conservative form (2.3.3) is

$$\begin{aligned} {}^{NL}_{NCon} S(\hat{k}, \hat{\mu}, n) = \sum_{k1} (T_e/T_i) \delta \hat{\phi}_{k1} i(\hat{v}_\perp \hat{k}_1/2) [\exp(-i\beta_1) \partial_{\hat{\mu}} \delta \hat{F}_{k2}^{n-1} + \exp(+i\beta_1) \partial_{\hat{\mu}} \delta \hat{F}_{k2}^{n+1}] \\ - \sum_{k1} \delta \hat{\phi}_{k1} i \hat{k}_1 / (2\hat{v}_\perp) [\exp(-i\beta_1) (n-1) \delta \hat{F}_{k2}^{n-1} - \exp(+i\beta_1) (n+1) \delta \hat{F}_{k2}^{n+1}]. \end{aligned} \quad (2.3.3)$$

After deriving the $\partial_{\hat{\mu}}$ into the bracket in the first term of Eq. (2.3.2), the conservative form in Eq. (2.3.2) and the non-conservative form in Eq. (2.3.3) are found to be equivalent as required. Notice that the nonlinear coupling coefficient is enhanced by $1/\hat{v}_\perp$ at low velocities.

2.3.4 Incremental entropy

The nonlinear term is calculated as $[{}^{NL}_{Con} S(\hat{k}, \hat{\mu}, n) + {}^{NL}_{NCon} S(\hat{k}, \hat{\mu}, n)]/2$ in the rCYCLO code, in order to cancel any numerical error arising from the numerical approximation of the μ -derivative operator in the nonlinear conservation of incremental entropy. The incremental entropy

of CKinFH is defined as

$$\begin{aligned} S = \sum_k \oint d\alpha \int_0^\infty d\hat{\mu} (\delta \hat{f}_k^* \delta \hat{f}_k) \\ = 2\pi \int_0^\infty d\hat{\mu} \sum_k \sum_{n=-N_\alpha+1}^{n=N_\alpha-1} (\delta \hat{F}_k^n)^* \delta \hat{F}_k^n. \end{aligned} \quad (2.3.4)$$

With the linear terms in Eq. (2.1.14) and Eq. (2.3.1) deleted, it is easy to show in the gyro-phase form, and after some algebra in the discrete Fourier transform form, that the total S is conserved; the calculation details are presented in Appendix A.

2.3.5 The Poisson equation

The Poisson equation for CKinFH is given as

$$\delta\hat{\phi}_k = \frac{2\pi \int d\hat{\mu} \delta\hat{F}_k^0(\hat{\mu})/n_0 - C_{DW} \cdot \delta\hat{n}_k^e}{(1 - C_{DW})R_k + C_{DW} \cdot (\hat{\lambda}_D^2 \hat{k}^2)} \quad (2.3.5)$$

Eq. (2.3.5) indicates that only the zero-th Fourier harmonic $\delta\hat{F}_k^0$ contributes to the electrostatic potential for CKinFH. Whether the Debye length $\hat{\lambda}_D$ is a very small number or even zero is not so important for low- k ITG gyrokinetics (unless dealing with high- k electromagnetic ETG). However, this is very important to cyclokinetics, because Eq. (2.3.5) is numerically close to “0/0” when $C_{DW} = 1$. Moreover, there is a non-zero polarization term in the denominator of the gyrokinetic Poisson equation, while there is no such polarization term in the denominator of the CKinFK Poisson equation in Eq. (2.3.5). If the simulation was conducted in the real space (x, y) , it would likely be impractical to resolve such small scales while on the ion gyro-scale. It is necessary to extrapolate the physically small $\hat{\lambda}_D^2$ from some larger and numerically practical $\hat{\lambda}_D^2$. However, $\hat{\lambda}_D^2$ should not be too large, since an unphysically large $\hat{\lambda}_D^2$ will produce spurious high- k ITG modes in both gyrokinetics and cyclokinetics. In the rCYCLO simulations, the linear growth rates, the linear frequencies and the turbulent transport level do not significantly depend on the size of $\hat{\lambda}_D^2$, if $\hat{\lambda}_D^2$ is sufficiently small (e.g., 0.01).

The particle and energy fluxes are given by

$$[\hat{F}, \hat{Q}^\perp] = Re 2\pi \int_0^\infty d\hat{\mu} \sum_k [1, (T_i/T_e)\hat{\mu}]$$

$$\delta\hat{\phi}_k = \frac{2\pi \int d\hat{\mu} J_0(k\rho) \delta\hat{F}_k(\hat{\mu})/n_0 - C_{DW} \cdot \delta\hat{n}_k^e}{(T_e/T_i) 2\pi \int d\hat{\mu} F_M(\hat{\mu}) [1 - J_0^2(k\rho)] + (1 - C_{DW})R_k + C_{DW} \cdot (\hat{\lambda}_D^2 \hat{k}^2)}, \quad (2.4.2)$$

where $2\pi \int d\hat{\mu} F_M(\hat{\mu}) [1 - J_0^2(k\rho)]$ represents the ion polarization. Gyrokinetics also nonlinearly conserves the incremental entropy, defined as:

$$S = 2\pi \sum_k \int_0^\infty d\hat{\mu} (\delta\hat{F}_k^* \delta\hat{F}_k). \quad (2.4.3)$$

The radial ion particle and energy fluxes are:

$$[\hat{F}, \hat{Q}^\perp] = Re 2\pi \int_0^\infty d\hat{\mu} \sum_k [1, (T_i/T_e)\hat{\mu}] \cdot i\hat{k}_y \delta\hat{\phi}_k^* [J_0(k\rho) \delta\hat{G}_k(\hat{\mu})/n_0]. \quad (2.4.4)$$

2.5 Electron equations of motion

2.5.1 Non-adiabatic electron model

A simple near adiabatic electron response model is

$$\cdot i\hat{k}_y \delta\hat{\phi}_k^* [\delta\hat{G}_k^0(\hat{\mu})/n_0], \quad (2.3.6)$$

where only the non-adiabatic distribution function for the $n = 0$ harmonic appears.

2.4 Gyrokinetic equations

The CKinCH equation [Eq. (2.2.12)] entirely reduces to the gyrokinetic equation [Eq. (2.4.1)] when truncated at the zero-th cyclotron harmonic. The zero-th cyclotron harmonic of CKinCH represents the low-frequency drift motion while other harmonics represent the high-frequency ion cyclotron motion. Keeping only the zero-th harmonic (by setting $n = n' = 0$) in Eq. (2.2.11) [or the equivalent Eq. (2.2.12)], the nonlinear interaction is greatly simplified. Only the first two terms in Eqs. (2.2.9) and (2.2.10), or essentially the first $\hat{\varepsilon}_z \cdot \hat{\mathbf{k}}_1 \times \hat{\mathbf{k}}_2$ term in Eq. (2.2.11), survives with $\Delta_0^0(\beta, \beta_1, \beta_2) \equiv 1$. The correspondingly reduced gyrokinetic equation (also with parallel motion and variation removed) is given by

$$D\delta\hat{F}_k/D\hat{t} - i\hat{\omega}_k^d \delta\hat{G}_k = -i\hat{\omega}_*^{nT} J_0(k\rho) \delta\hat{\phi}_k n_0 F_M(\hat{\mu}) + \sum_{k1} \hat{b} \cdot (\hat{\mathbf{k}}_1 \times \hat{\mathbf{k}}_2) J_0(k1\rho) \delta\hat{\phi}_{k1} \delta\hat{F}_{k2}, \quad (2.4.1)$$

where $\delta\hat{F}_k(\hat{\mu}) = \delta\hat{G}_k(\hat{\mu}) - (T_e/T_i) \delta\hat{\phi}_k n_0 F_M(\hat{\mu}) J_0(k\rho)$ is the non-adiabatic part of the distribution function. It is not surprising that the $\hat{\mu} \partial_{\hat{\mu}} \delta F$ (the last term in Eq. (2.2.12)) in the nonlinearity has been dropped away, because gyrokinetics conserves the magnetic moment.

The Poisson equation of gyrokinetics is given by

$$\frac{\delta n_k^e}{n_0} = \frac{e \delta\hat{\phi}_k}{T_e} R_k, \quad (2.5.1)$$

where the response function is $R_k = \lambda_k - i\delta_k$, and δ_k is the electron non-adiabatic parameter. $\delta_1 > 0$ will add unstable electron drift waves to the unstable “toroidal” ITG modes. Positive δ_k drives instability to all except the $\hat{k}_y = 0$ modes. $\hat{k}_y = 0$ and $\hat{k}_x \neq 0$ modes represent the zonal modes. $\lambda_k = [1, 0]$ represents $[\hat{k}_y \neq 0, \hat{k}_y = 0]$ respectively. $\lambda_k = 0$ represents the zonal mode response to the fast parallel motion of the electron, which cannot support a parallel electric field difference. $\lambda_k = 1$ for $\hat{k}_y \neq 0$ modes describes the adiabatic response of the electron motion in the direction parallel to the electric field.

Since physically δ_1 is a strong function of the frequency, the nearly adiabatic electron response (with a fixed δ_1) assumed above should be seen as an illustra-

tive test model. In more physically realistic simulations, electrons are treated as collisional drift wave electrons.

2.5.2 Collisional drift wave electron model

The simulations in Chapter 4 utilize the collisional drift wave (CDW) electron model. The CDW electron model is essentially the Hasegawa-Wakatani electron model [19] with a grad- B drift added:

$$D\delta\hat{n}_k^e/Dt + i\hat{\omega}_d^e\delta\hat{n}_k^e + \alpha_A(\delta\hat{n}_k^e - \delta\hat{\phi}_k) = -i(\hat{\omega}_*^n - \hat{\omega}_d^e)\delta\hat{\phi}_k + \sum_{k1} \hat{b} \cdot (\hat{k}_1 \times \hat{k}_2) \delta\hat{\phi}_{k1} \delta\hat{n}_{k2}^e, \quad (2.5.2)$$

where $\hat{\omega}_*^n \Rightarrow \hat{k}_y(a/L_n)$ is the density gradient drive frequency, and $\hat{\omega}_d^e \Rightarrow 2\hat{k}_y(a/R)$ is the grad- B drift frequency. The factor 2 here is again used to compensate for the parallel motion curvature drive. $\alpha_A = \hat{k}_{\parallel}^2/[\hat{\nu}_{ei}(m_e/m_i)]$ is the CDW adiabaticity parameter used for controlling the turbulence strength. $\hat{k}_{\parallel} = a/Rq$ is the parallel wavenumber and $\hat{\nu}_{ei}$ is the electron-ion collision frequency. α_A is derived from Ohm's law in the parallel direction. Large α_A leads to a lower turbulence adiabatic electron response (with only the ITG mode drive). Small α_A corresponds to a high turbulence level contributed by the resistive interchange modes. These are strongly driven at a long wavelength (small \hat{k}_y). While the overall sign of the nonlinear terms has no effect on the time-averaged transport, it is very important to have a correct sign of the electron $E \times B$ nonlinearity relative to the ion $E \times B$ nonlinearity.

2.6 Discussion

2.6.1 The reason for omitting the parallel motion and variations

The purpose of this work is to investigate the effect of the nonlinear coupling between the high-frequency ion cyclotron motion and low-frequency drift motion. Therefore, it is important that no approximation regarding the cross-field nonlinear $E \times B$ motion will be made. What type of mode is linearly driven unstable or what artificial damping is chosen is less important, as long as the same model is used in both cyclokinetics and gyrokinetics. The model gyrokinetic linear rates must match the model cyclokinetic low-frequency linear rates. The parallel nonlinearity is one order smaller than the cross-field $E \times B$ nonlinearity, since $k_{\parallel}/k_{\perp} = 1/\Omega^*$. Gyrokinetic implementations typically omit the parallel nonlinearity. The trapped particle modes and the Landau damping in the parallel direction are not relevant to the breakdown

of gyrokinetics. Thus, the parallel motion and parallel variations are omitted. Meanwhile, the calculation complexity is reduced as well.

2.6.2 Recipes for generalization and conversion of continuum gyrokinetic implementations to cyclokinetic implementations

The recipes for converting continuum δf -gyrokinetic implementations (such as GYRO [27, 48] or GS2 [49, 50]) appear to be straightforward (and intuitively obvious). The linear grad- B drifts, curvature drifts, as well as parallel motion operations in realistic geometries should remain unchanged. Following Eqs. (2.2.2)–(2.2.4), in addition to the usual equation for the gyrokinetic perturbed density of gyro-centers or zero-th cyclotron harmonic, $\pm n$ symmetric equations for the higher harmonics $\partial\delta\hat{F}_{\mathbf{k}}^n/\partial t \mp \text{in}\Omega_*\delta\hat{G}_{\mathbf{k}}^n = \dots$ should be added with the gyro-averaged potential perturbation omega-star term generalized: $J_0(k\rho)\delta\hat{\phi}_k i\hat{\omega}_{*k}^T n_0 F_M \Rightarrow J_n(k\rho)\delta\hat{\phi}_k i\hat{\omega}_{*k}^T n_0 F_M$. The ion transport and quasi-neutrality equation follow Eqs. (2.2.5) and (2.2.6). Except when treating high- $kk_{\perp}\rho_i \gg 1$ ETG modes, drift-kinetic electrons are normally used in gyrokinetic implementations in place of the i-delta model or collisional drift wave model here. In addition, both GYRO and GS2 operate with the normalized energy $\hat{\varepsilon} = \hat{\mu}\hat{B} + \hat{u}^2$ and angle grid $\lambda = \hat{\mu}/\hat{\varepsilon}$ replaces the $(\hat{\mu}, \hat{u})$ grids here (poloidal variation in \hat{B} accounts for the trapping). Thus, the velocity space volume element becomes $\oint d\alpha \int_0^\infty d\hat{\mu} \int_{-\infty}^\infty d\hat{u} \Rightarrow \sum_{\sigma=\pm 1} (2\pi/\sqrt{2}) \int_0^\infty \sqrt{\hat{\varepsilon}} d\hat{\varepsilon} \int_0^{1/\hat{B}} d\lambda/\sqrt{1-\lambda\hat{B}}$ and the gradient $\partial_{\hat{\mu}}|_{\hat{u}} \Rightarrow \hat{B}\{\partial_{\hat{\varepsilon}} + [1/(\hat{\varepsilon}\hat{B})]\partial_{\lambda}\}$ must be converted in the nonlinear terms in Eqs. (2.2.9) and (2.2.10), replacing the gyrokinetic nonlinearity in Eq. (2.2.11).

Generalization to electromagnetic perturbations and transport is straightforward. For example, adding $\delta\mathbf{B}_{\perp}$ perturbations by following the GYRO [48] notation and gyroBohm normalization, $\delta\hat{\phi}_k$ is replaced by $\delta\hat{U}_k = \delta\hat{\phi}_k - \sqrt{2T_i/T_e}\hat{u}\delta\hat{A}_k$, with $\delta\hat{A} = (c_s/c)(e\delta A_{\parallel}/T_e)/\rho^*$, $\delta\hat{H}_k^n = [\delta\hat{F}_k^n + J_n(k\rho)\sqrt{2T_i/T_e}\hat{u}\delta\hat{A}_k(T_e/T_i)n_0F_M]$ replaces $\delta\hat{F}_k^n$, and $\delta\hat{G}_k^n$ is replaced by $\delta\hat{H}_k^n + J_n(k\rho)\delta\hat{U}_k(T_e/T_i)n_0F_M$ in Eqs. (2.2.2)–(2.2.6) and Eqs. (2.2.9)–(2.2.11).

3 Numerical method

In order to test the high-turbulence level breakdown of low-frequency gyrokinetics against high-frequency cyclokinetic simulations, the cyclokinetic equations should be solved. Therefore, in this Chapter the corresponding cyclokinetic code will be developed, named rCYCLO,

for simulating the cyclokinetic turbulence transport. The letter “r” denotes reducing the geometry and parallel motion, while “CYCLO” stands for cyclokinetics. The main purpose of this Chapter is to document the numerical methods for cyclokinetic nonlinear simulations and to validate the rCYCLO code.

rCYCLO is a parallel-executed, Eulerian (or continuum) code, which is designed to simulate the 4D $[k_x, k_y, \mu, \alpha]$ nonlinear cyclokinetic turbulent transport. The 2D $[k_z, v_z]$ parallel motion is suppressed. Only the electrostatic perturbations in a local flux-tube geometry are considered, with a shear-less B -field decreasing in the radial x direction. The $E \times B$ motion in the perpendicular direction is considered, and there is no approximation in the $E \times B$ nonlinearity.

The rCYCLO code enables to independently simulate the turbulent transport of both gyrokinetics, cyclokinetics in cyclotron harmonics (CKinCH), cyclokinetics in Fourier harmonics (CKinFH), and drift kinetics. Therefore, the breakdown of gyrokinetics against cyclokinetics through simulating their turbulent transport can be tested at the same geometry and by using the same physical and grid parameters.

The calculations of rCYCLO code mainly include four parts. In the first part, the discretized grids are loaded, the initial values of $\delta\hat{F}_k$ (and $\delta\hat{\phi}_k$) are assigned, and the linear dispersion relation is calculated. In the second part, the nonlinear terms are calculated with the values of $\delta\hat{F}_k$ and $\delta\hat{\phi}_k$. In the third part, the time step is advanced and the values of $\delta\hat{F}_k$ and $\delta\hat{\phi}_k$ for the next time step are obtained. In the last part, the values of physical variables are output and diagnosed. The second and third parts constitute the main loop of temporal evolution. The nonlinear dynamics calculations in the second part are the most computationally expensive ones, and are parallelized for the α and μ directions, whereas the calculations for the k_x and k_y directions cannot be parallelized because the k space is strongly coupled. In the third part, the calculations are parallelized for the k_x and k_y directions. The rCYCLO code offers a visualized IDL program, called vuRCYCLO, for analyzing the data and presenting the physical results conveniently.

The numerical methods applied in the rCYCLO code are documented in this section. The numerical methods for the nonlinear simulations of cyclokinetics in the gyro-phase Fourier harmonic form (CKinFH) are described in details in Ref. [32]. The numerical treatment of CKinFH in Ref. [32] is the same as that of CKinCH in Ref. [39]. The nonlinear CKinCH simulations are more computationally expensive than the CKinFH simulations, but the CKinCH formulation is more transparently related to gyrokinetics.

The cyclokinetic equations form a system of coupled linear and nonlinear partial differential equations (PDEs) [see Eq. (2.1.14)]. The perpendicular wavenumber \mathbf{k} modes are linearly independent but nonlinearly coupled. The linear and nonlinear terms have a partial derivative in the cyclic gyro-phase variable α and the nonlinear terms have a partial derivative in the magnetic moment variable μ . The latter is a significant challenge for the numerical μ -derivative operator proposed in this work. Most importantly, the nonlinear terms in the cyclokinetics formulation do not take the common form $\hat{z} \cdot \mathbf{k}_{\perp 1} \times \mathbf{k}_{\perp 2}$ of the nonlinear gyrokinetics [see Eq. (2.4.1)]. An implicit time linear advance step followed by a lag time nonlinear step is applied in the rCYCLO code. The implicit time linear advance ensures the accuracy of treating the stiff linear dispersion matrix, which must span the low-frequency drift modes and the higher frequency IC modes. For CKinFH, at least 7 to 15 Fourier harmonics are required to accurately recover the linear rates of the gyrokinetic modes even at the highest wavenumbers resolving the ion gyro-radius scale. The novel numerical treatment of the μ -derivative operator (in particular) is carefully chosen to conserve the incremental entropy. The μ -derivative operator enters only in the cyclokinetic $E \times B$ nonlinearity, which contains an apparent $\mu \rightarrow 0$ factor. It must perfectly satisfy the μ -integration by parts rule with zero boundary conditions at $\mu = 0$ and infinity, which then yields a certain level of inaccuracy in the μ -derivative operation. This inaccuracy will be suppressed when either the μ -grid is closely spaced or the low-frequency drift modes are decoupled from the high-frequency IC modes. The deviation of the odd and even μ -grid saturation processes caused by this inaccuracy tends to disappear while increasing Ω^* from 10 to 30.

As a linear code validation test of the rCYCLO implementation, the CKinFH and CKinCH linear rates from the implicit initial value time advance are in an excellent agreement with their eigenvalue solver results. The low-frequency cyclokinetic linear mode rates are in a good agreement with the gyrokinetic rates. As a nonlinear verification, the gyrokinetic transport level obtained by using the rCYCLO implementation recovers the cyclokinetic transport at high Ω^* values and low turbulence levels, as required. However, for the stable IC modes, the cyclokinetic transport level is lower than the gyrokinetic transport at low Ω^* values and high turbulence levels. The transport level of cyclokinetics is lower than that of gyrokinetics because the turbulent electrostatic energy is drained to the less unstable (and in fact stable) IC modes.

3.1 Discretization of magnetic moment

The integration along the μ -direction is numerically expressed as

$$2\pi \int_0^\infty d\hat{\mu} \delta \hat{F}_k^n(\hat{\mu}) = \sum_{j=1}^{j=N_\mu} \delta \hat{F}_k^n(\hat{\mu}_j) W_j. \quad (3.1.1)$$

Let us split the $\hat{\mu}$ integration domain into two regions: $[0, \hat{\mu}_{max}]$ and $[\hat{\mu}_{max}, \infty)$. The first region is described by $\hat{\mu}_j$ ($j = 1, 2, \dots, N_\mu - 1$), and each of the μ -grid points represents the center of a “bin”, with “bin weight” W_j . The corresponding modified bin weights $\bar{W}_j = W_j F_M(\hat{\mu}_j)$ satisfy $\bar{W}_1 = \bar{W}_2 = \dots = \bar{W}_{N_\mu-1}$, which means the weights W_j are chosen such that for a Maxwellian distribution each μ -grid bin is distributed with the same percentage of the distribution. The second region is represented by the last grid point $\hat{\mu}_{N_\mu}$, and set $\hat{\mu}_{N_\mu} = \hat{\mu}_{max}$. The weight of the last grid point evaluates the infinite integral according to $2\pi \int_{\hat{\mu}_{N_\mu}}^\infty d\hat{\mu} F_M(\hat{\mu}) = \bar{W}_{N_\mu}$, where $\bar{W}_{N_\mu} = \bar{W}_j$ ($j = 1, 2, \dots, N_\mu - 1$) is a reasonable and satisfactory choice for obtaining good μ -grid convergence (see Section 3.5). Thus, the weights of all of the grid points have the desirable property $2\pi \int_0^\infty d\hat{\mu} F_M(\hat{\mu}) = \sum_{j=1}^{j=N_\mu} W_j F_M(\hat{\mu}_j) = \sum_{j=1}^{j=N_\mu} \bar{W}_j = 1$. An eight μ -grid example is listed in Table 1. This μ -discretization method is essentially equivalent to the Maxwellian energy space discretization method introduced in Ref. [48].

Table 1 Sample magnetic moment μ -grids and weights.

j	$\hat{\mu}_j$	\bar{W}_j
1	0.066765696	0.1249072
2	0.2106067	0.1248763
3	0.3788429	0.1248270
4	0.5815754	0.1247410
5	0.8369882	0.1245700
6	1.183562	0.1241478
7	1.732868	0.1225323
8	2.079442	0.1250000

3.2 Discretization of magnetic moment derivative operator

The μ -derivative operator $D_{jj'}^\mu$ is defined as

$$\partial_{\hat{\mu}} V(\hat{\mu})|_j = \sum_{j'=1}^{j'=N_\mu} D_{jj'}^\mu V(\hat{\mu}_{j'}), \quad (3.2.1)$$

where $V(\hat{\mu})$ is an arbitrary function of $\hat{\mu}$. $D_{jj'}^\mu$ is required for preserving the integration by parts so as to conserve the incremental entropy. For arbitrary functions $U(\hat{\mu})$ and $V(\hat{\mu})$, the discretized integration by parts is

expressed as

$$\begin{aligned} \sum_j W_j U(\hat{\mu}_j) \sum_{j'} D_{jj'}^\mu V(\hat{\mu}_{j'}) \\ = U(\hat{\mu}) V(\hat{\mu})|_{\hat{\mu}_1}^{\hat{\mu}_{N_\mu}} - \sum_j W_j V(\hat{\mu}_j) \sum_{j'} D_{jj'}^\mu U(\hat{\mu}_{j'}). \end{aligned}$$

The boundary term $U(\hat{\mu}) V(\hat{\mu})|_{\hat{\mu}_1}^{\hat{\mu}_{N_\mu}}$ appears to be non-zero, since numerically $\hat{\mu}_1$ and $\hat{\mu}_{N_\mu}$ cannot reach 0 and ∞ as required by the μ -continuum equations. To eliminate the non-zero boundary term, the μ -derivative operator $D_{jj'}^\mu$ must satisfy the remaining part of the above equation: $\sum_j W_j U(\hat{\mu}_j) \sum_{j'} D_{jj'}^\mu V(\hat{\mu}_{j'}) = -\sum_j W_j V(\hat{\mu}_j) \sum_{j'} D_{jj'}^\mu U(\hat{\mu}_{j'})$ which then can be reduced to

$$W_j D_{jj'}^\mu = -W_{j'} D_{j'j}^\mu. \quad (3.2.2)$$

Next, we define the tridiagonal derivative matrix $H_{jj'}$ from a two-point differential $\partial_{\hat{\mu}} \delta \hat{F}_k(\hat{\mu}_j) = [\delta \hat{F}_k(\hat{\mu}_{j+1}) - \delta \hat{F}_k(\hat{\mu}_{j-1})]/(\hat{\mu}_{j+1} - \hat{\mu}_{j-1}) = \sum_{j'=1}^{j'=N_\mu} H_{jj'} \delta \hat{F}_k(\hat{\mu}_{j'})$, as follows:

$$\begin{aligned} H_{j,j'} &= 1/(\hat{\mu}_{j+1} - \hat{\mu}_{j-1}) \text{ for } j' = j + 1, \\ H_{j,j'} &= -1/(\hat{\mu}_{j+1} - \hat{\mu}_{j-1}) \text{ for } j' = j - 1, \\ H_{j,j'} &= 0 \text{ for other } j, j'. \end{aligned} \quad (3.2.3)$$

Finally, the μ -derivative operator in Eq. (3.2.4) is obtained by combining Eq. (3.2.2) for $D_{jj'}^\mu$ with Eq. (3.2.3) for $H_{jj'}$:

$$D_{jj'}^\mu = [H_{jj'} - (W_{j'}/W_j) H_{j'j}]/2. \quad (3.2.4)$$

It should be clear that if the μ -grid is closely spaced, then $W_j \sim W_{j\pm 1}$ and $D_{jj'}^\mu \sim H_{jj'} \sim -H_{j'j}$. As might be expected from the compromised “zero” μ -boundary conditions, the μ -derivative matrix operation becomes rather inaccurate for $j \rightarrow 1$ and $j \rightarrow N_\mu$. However, since the μ -derivative operator only appears in the nonlinear terms, as long as the incremental entropy is exactly conserved, a certain level of inaccuracy in the μ -derivative operation is just an error in the nonlinear incremental entropy transfer and “scrambling.” This may be not very important. The important point is that with increasing N_μ (and in particular with $\hat{\mu}_1$ getting closer to zero) the μ -grid convergence is easily achieved, as shown in Section 3.5.

The discretized μ -derivative operator is novel. It is designed for canceling any non-zero boundary terms at $\mu = 0$ and $\mu = \infty$ in the continuum μ -integration by parts so as to numerically conserve the incremental entropy.

Note that the calculations for the α, x, y directions are much easier than the ones for the μ -direction, be-

cause these calculations are analytically transformed to the harmonic number n and wavenumbers k_x, k_y .

3.3 Linear eigenvalue solver

CKinFH is taken as an example for illustrating the rCYCLO eigenvalue solver. The Poisson equation (Eq. (2.3.5)) indicates that the electric field $\delta\hat{\phi}_k$ is a function of $\delta\hat{F}_k^0(\hat{\mu})$. Then, the dispersion matrix $M_{jj'}^{nn'}$ and the linear eigenvalue equation (Eq. (3.3.1)) are obtained by combining the linear parts of Eqs. (2.3.1) and (2.5.2) with Eq. (2.3.5):

$$-i\omega\delta\hat{F}_k^n(\hat{\mu}_j) = \sum_{n'=-N_\alpha+1}^{n'=N_\alpha-1} \sum_{j'=0}^{j'=N_\mu} M_{jj'}^{nn'}(\hat{k})\delta\hat{F}_k^{n'}(\hat{\mu}_{j'}), \quad (3.3.1)$$

where $j = 1, 2, 3, \dots, N_\mu$ represent the ion, and $j = 0$ represents the electron (for example: $\delta\hat{F}_k^0(\hat{\mu}_0) = \delta\hat{n}_k^e$). The linear frequency and growth rate are just the eigenvalues (solved by using the numerical library LAPACK) of the dispersion matrix $M_{jj'}^{nn'}$. The same procedure is used in gyrokinetics and CKinCH for solving their linear frequency and growth rate as CKinFH.

3.4 Time advance method

Again taking CKinFH as an example, the nonlinear equation for the temporal evolution corresponding to Eq. (3.4.1) is

$$D\delta\hat{F}_{k,j}^n/Dt = \sum_{n'=-N_\alpha+1}^{n'=N_\alpha-1} \sum_{j'=0}^{j'=N_\mu} M_{jj'}^{nn'}(\hat{k})\delta\hat{F}_{k,j'}^{n'} + {}^{NL}S_{k,j}^n. \quad (3.4.1)$$

The Ω^* terms result in the large entries in $M_{jj'}^{nn'}$ with a wide range of eigenvalues, making it a stiff matrix. This stiff matrix requires using an implicit solution method for obtaining temporal evaluation. Thus, the rCYCLO implementation utilizes a time-centered implicit linear advance scheme and an explicit nonlinear advance scheme. The perturbed distribution function of the next time step $\delta\hat{F}_{k,j}^n$ can be obtained by multiplying the inverse matrix $[R^{-1}]_{jj'}^{nn'}$ on $\bar{S}_{k,j}^n$:

$$\delta\hat{F}_{k,j}^n = \sum_{n'=-N_\alpha+1}^{n'=N_\alpha-1} \sum_{j'=0}^{j'=N_\mu} [R^{-1}]_{jj'}^{nn'}(\hat{k})\bar{S}_{k,j'}^{n'}, \quad (3.4.2)$$

where $\bar{S}_{k,j}^n$ and $R_{jj'}^{nn'}$ are given by

$$\bar{S}_{k,j}^n = \delta\hat{F}_{k,j}^n + (dt/2) \sum_{n'=-N_\alpha+1}^{n'=N_\alpha-1} \sum_{j'=0}^{j'=N_\mu} M_{jj'}^{nn'}(\hat{k})\delta\hat{F}_{k,j'}^{n'}$$

$$+ (dt) {}^{NL}S_{k,j}^n, \quad (3.4.3)$$

$$R_{jj'}^{nn'}(\hat{k}) = \delta_{n'}^n \delta_{j'}^j - (dt/2) M_{jj'}^{nn'}(\hat{k}). \quad (3.4.4)$$

Here, $\delta\hat{F}_{k,j}^n$ is the perturbed distribution function in the previous time step. ${}^{NL}S_{k,j}^n$ is the value of the nonlinear terms in the previous time step. The Poisson equation (Eq. (2.3.5)) is used for updating $\delta\hat{\phi}_k$ at the end of each time step. The linear calculation of the Poisson equation requires collective communication over the μ, n dimensions at each k_x and k_y grid coordinates. Therefore, the linear calculations of Eqs. (3.4.2) and (3.4.3) are parallelized in the k_x and k_y dimensions. Each linear k mode is assigned a dedicated processor.

3.5 Grid convergence test

The simulations use the rCYCLO standard case parameters, which are listed in Table 2. All calculations in this work were performed by using these parameters, unless specified otherwise. The number of the grid points for the standard case is $N_{kx} \times N_{ky} \times (2N_\alpha - 1) \times (N_\mu + 1) = 21 \times 21 \times 9 \times 22 = 87318$. The μ -grid number 22 equals to $N_\mu = 21$ for ions plus 1 forelectron. The possible maximal number of processors for the standard case is $(2N_\alpha - 1) \times (N_\mu + 1) = 9 \times 22 = 198$ in the rCYCLO parallel processing code. The grid convergence in the k -space, μ -space, and Fourier harmonics is demonstrated in this section. During the grid convergence test, only one grid parameter is changed while all other grid parameters are kept at their standard case values.

3.5.1 Wavenumber grid convergence

Figure 4 displays the gyrokinetic energy diffusivity $\hat{\chi}$ versus the number of k -modes, which demonstrates good k -space grid convergence. The number of modes N_k is increased from $11 \times 11 = 121$ to $29 \times 29 = 841$ while fixing $\hat{k}_x^{\max} = \hat{k}_y^{\max} = 1.5$. Grids converge after $N_k = 17 \times 17 = 289$, which indicates that $N_k = 21 \times 21 = 441$ is satisfactory for the standard case. Here and below the standard case is always marked by a red circle.

3.5.2 Harmonic number convergence

Figure 5 shows the CKinFH energy diffusivity $\hat{\chi}$ versus

Table 2 The physics parameters of rCYCLO standard case.

a/L_n	a/L_{Ti}	α_A	a/R	μ_{LK}	μ_{HK}	Ω^*	$\hat{\lambda}_D$
4.00	4.00	1.0	0.3	0.05	0.3	10	0.1
The grid parameters of rCYCLO standard case.							
C_{DW}	N_k	$\hat{k}_x^{max}(=\hat{k}_y^{max})$	N_μ	N_α			
1	21×21	1.5	21	5			

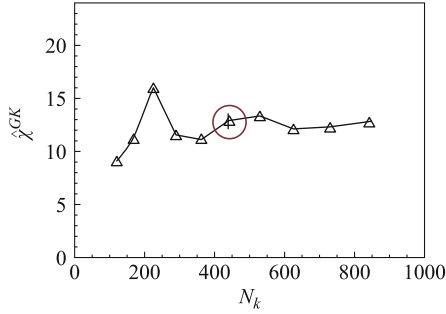


Fig. 4 The gyrokinetic energy diffusivity $\hat{\chi}$ versus the number of k -modes N_k for the mode number convergence test. The standard case is chosen as $N_k = 21 \times 21 = 441$.

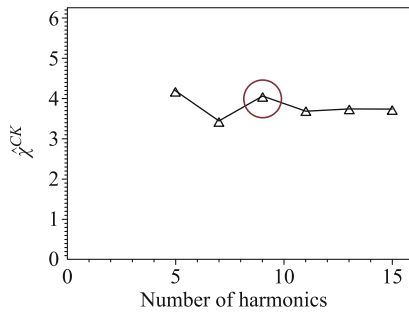


Fig. 5 The gyrokinetic energy diffusivity $\hat{\chi}$ versus the number of harmonics of gyro motion (calculated by $2N_\alpha - 1$) for the harmonic number convergence test. The standard case is chosen as 9.

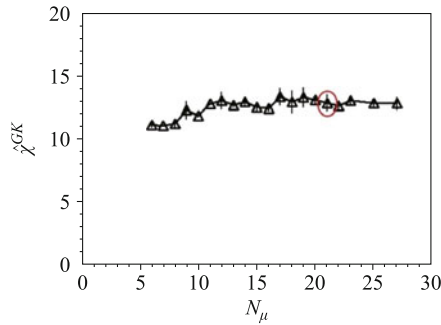


Fig. 6 The gyrokinetic energy diffusivity $\hat{\chi}$ versus N_μ for the μ -grid convergence test. The standard case is chosen as $N_\mu = 21$.

the number of harmonics of gyro-motion (calculated as $2N_\alpha - 1$), which exhibits convergence after 7, with 9 chosen for the standard case.

3.5.3 Magnetic moment grid convergence

Figure 6 shows the GK energy diffusivity $\hat{\chi}$ versus the μ -grid number N_μ , which converges after $N_\mu = 11$, with $N_\mu = 21$ chosen as the standard case parameter.

Figure 7 illustrates the CKinFH energy diffusivity $\hat{\chi}$ versus N_μ . As N_μ increases, the μ grid resolution increases fast while the μ_{max} value increases very slowly.

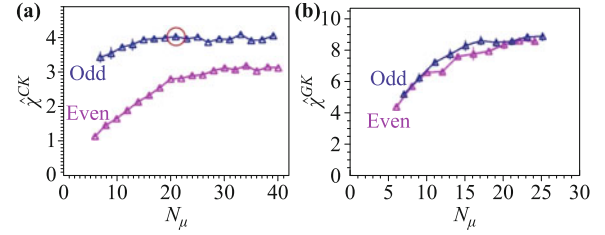


Fig. 7 The gyrokinetic energy diffusivity $\hat{\chi}$ versus N_μ , where (a) the odd and even μ grid numbers follow the different convergence processes at $\Omega^* = 10$ (the standard case parameter); (b) the odd and even convergence processes almost recover each other at $\Omega^* = 30$.

Note that the odd and even μ -grid numbers follow different convergence processes at $\Omega^* = 10$ (the standard case parameter), as shown in Fig. 7(a). However, the odd N_μ converges faster than the even, and finally both approach a similar level; therefore, the odd number $N_\mu = 21$ was chosen as the standard case. The different convergence of the odd and even N_μ is caused by the inaccuracy of the μ -derivative operation. This phenomenon of different convergence can be suppressed either by making the μ -grids more closely spaced by increasing N_μ , or by decreasing the coupling between the low- and high-frequency motion by increasing the relative ion cyclotron frequency Ω^* . To demonstrate the latter, Fig. 7(b) shows that after setting $\Omega^* = 30$, the odd and even convergence trends become nearly identical. This result also indicates that the inaccuracy of the μ -derivative operation is just some “scrambling” error and is not very important.

3.6 The rCYCLO code validation

When testing the high-turbulence level breakdown of low-frequency gyrokinetics against high-frequency gyrokinetics, the rCYCLO implementation must ensure that: (i) the low-frequency gyrokinetic linear rates are not significantly different from the gyrokinetic rates (even at Ω^* values as low as 10); and (ii) at sufficiently large Ω^* and sufficiently low turbulence levels the non-linear gyrokinetic simulations recover the gyrokinetic transport levels as required.

3.6.1 Linear verification

The growth rates obtained from the initial value method recover the results obtained by using the eigenvalue solver, and the low-frequency mode growth rates of gyrokinetics recover those obtained by using CKinFH, as shown in Fig. 8 (these results also recover those obtained by using CKinCH, as described in the next chapter). This linear verification ensures reliable time evolution.

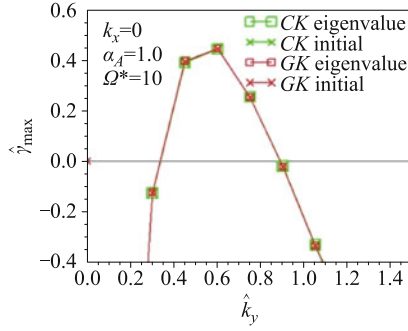


Fig. 8 Linear growth rates of gyrokinetics, cyclokinetics low-frequency (LF) modes at the fixed $k_x = 0$ of standard case. The figure shows that gyrokinetics recovers cyclokinetic low-frequency modes. Time initial results recover eigenvalue results.

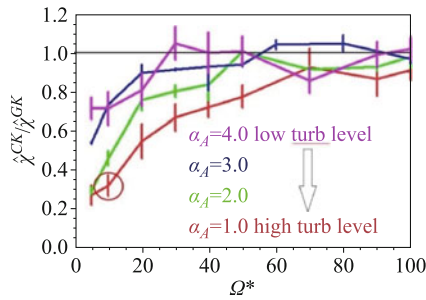


Fig. 9 The energy diffusivity ratio of cyclokinetics over gyrokinetics versus Ω^* . The transport level of gyrokinetics recovers cyclokinetics at high- Ω^* values and low turbulence levels. Cyclokinetic transport level is lower than gyrokinetics at low- Ω^* values and high turbulence levels.

3.6.2 Nonlinear verification

Figure 9 illustrates that the important nonlinear verification of the gyrokinetic transport level recovers the CKinFH transport level at high Ω^* values and low turbulence levels, as expected. Notice that the cyclokinetic transport level is lower than the gyrokinetic transport at low- Ω^* values. The turbulence is drained in the frequency space from the unstable low-frequency domain and spreads into the less unstable high-frequency domain. The transport level of cyclokinetics is lower than that of gyrokinetics, because the turbulent electrostatic energy is drained to the less unstable IC modes.

4 Simulation results

The L-mode near-edge transport “short-fall” of gyrokinetics in some gyrokinetic code simulations remains unsolved since its first discovery in 2007 [29]. Hence, this work aimed to answer the following two questions: (i) Where does the gyrokinetics formalism break down? (ii) Is the L-mode transport “short-fall” caused by the high turbulence level breakdown of the gyrokinetic approxi-

mation itself, or is anything left out of the gyrokinetic implementation? The answers will be given in this Chapter, and are as follows: (i) gyrokinetics starts to break down at the turbulence level $|\delta n/n_0| \cong 20\%$, or when the ratio of nonlinear $E \times B$ frequency over the ion cyclotron frequency $|\omega_{NL}/\Omega|$ exceeds 20%; (ii) L-mode near-edge “short-fall” is not caused by the nonlinear coupling between low-frequency drift motion and high-frequency ion cyclotron motion. Because the turbulence level $|\delta n/n_0|$ of the DIHD appears not to exceed 15% at the very edge, 20% is a very large value. Therefore, gyrokinetic theory is a good description of the Tokamak turbulence, both in the core regime and at the L-mode near-edge (in close field line).

The numerical simulations of CKinCH with rCYCLO in this Chapter have recovered the results of the simulations of CKinFH in Section 3, which were limited to stable high-frequency ion cyclotron modes. Gyrokinetic recovers the low-frequency linear growth rates and frequencies in either form of cyclokinetics. At sufficiently large $\Omega^* \geq 50$ and sufficiently low turbulence levels, the nonlinear gyrokinetic simulations have recovered the cyclokinetic transport levels as required. The cyclokinetic simulations given in this section show that the transport level of cyclokinetics with stable IC modes is lower than the gyrokinetic transport at low $\Omega^* \sim 10$ values. The transport level of cyclokinetics is lower than that of gyrokinetics because the turbulence electrostatic energy is drained to the less unstable IC modes. The breakdown of the gyrokinetic gyroBohm to Bohm scaling by draining and spreading in the frequency space at small Ω^* is analogous to the breakdown of gyroBohm to Bohm scaling by draining and spreading in the real space at large ρ^* , found in the gyrokinetic nonlocal simulations [51, 52]. The simulations show that with sufficiently unstable IC modes, the high-frequency component of the cyclokinetic transport level can exceed the gyrokinetic transport level at sufficient low $\Omega^* \sim 10$, and the direction of draining and spreading can be reversed. However, in these simulations the low-frequency component of the cyclokinetic transport and turbulence level did not exceed that of gyrokinetics. At higher and more physically relevant $\Omega^* \geq 50$ values with physically realistic IC driving rates, the low-frequency component of the cyclokinetic transport level still cannot be driven higher than that of gyrokinetics. Thus, the L-mode near-edge “short-fall” is not caused by the nonlinear coupling between low-frequency drift motion and high-frequency ion cyclotron motion.

While highly driven IC mode simulations may not be physically relevant, they were found to provide a perhaps unique example of bifurcated turbulent transport

states. When the maximal high-frequency (HF) driving rate is about twice the maximal low-frequency (LF) driving rate, a HF low transport level state can jump to a LF high transport level state. These HF and LF transport states represent two basins of attraction of nonlinear saturation. The corresponding electrostatic energy also saturates into two bifurcated steady states but without a jump in the total: the electrostatic energy is simply redistributed from low-frequency modes to high-frequency modes.

4.1 Standard case

4.1.1 Linear rates

The rCYCLO standard case parameters listed in Table 2 were applied here. Figure 10 shows the cyclokinetic linear growth rate $\hat{\gamma}$ of the leading low-frequency mode and the corresponding frequency $\hat{\omega}$, by using the eigenvalue solver described in Section 3.3. The frequency and growth rate of low-frequency drift modes of CKinCH are identical to those of gyrokinetics (GK) as well as CKinFH. The undamped leading low-frequency drift waves are unstable while the undamped high-frequency ion cy-

clotron modes are marginally stable. The addition of the low- k damping μ_{LK}/\hat{k}^2 (high- k damping $\mu_{HK}\hat{k}^4$) stabilizes the low- k (high- k) modes, providing a sink of incremental entropy. The nonlinear terms transfer the incremental entropy from the unstable source modes to the stable sink modes in the k space.

4.1.2 Nonlinear saturation

Figure 11 illustrates the nonlinear saturation processes in time during the initial evolution of the CKinCH standard case. The time average of the energy diffusivity over the saturation period is $\hat{\chi}^{GK} = 13.1 \pm 0.1$ for gyrokinetics, and $\hat{\chi}^{CK} = 3.18 \pm 0.07$ for cyclokinetics, respectively. The corresponding particle diffusivity is $\hat{D}^{GK} = 9.8 \pm 0.4$ for gyrokinetics, and $\hat{D}^{CK} = 2.82 \pm 0.07$ for cyclokinetics, respectively. The time step for the standard case is $\Delta t = 0.001a/c_s$ for gyrokinetics, and $\Delta t = 0.0005a/c_s$ for cyclokinetics, respectively. The time step was chosen to conserve the incremental entropy with the error below 1% after removing all linear terms. In general, the time step should be smaller when Ω^* is higher (e.g., $\Delta t = 0.00005a/c_s$ is chosen for the cyclokinetic case at $\Omega^* = 100$). Figure 12 shows the frequency spec-

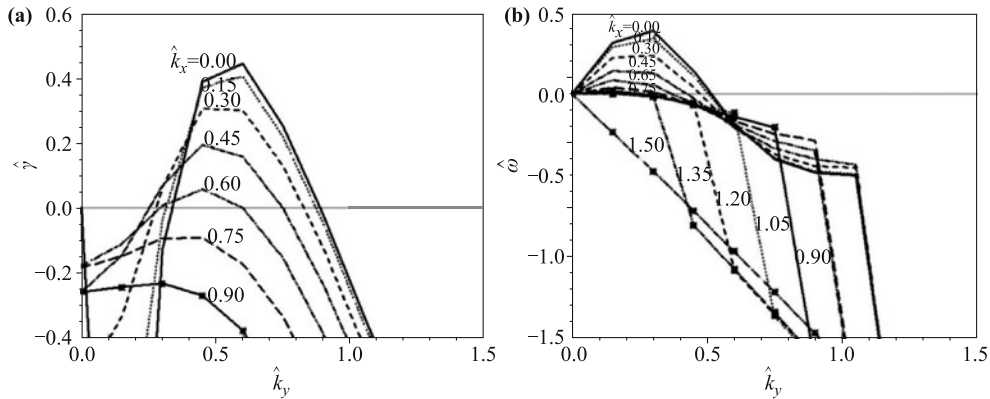


Fig. 10 (a) The linear growth rate $\hat{\gamma}$, and (b) frequency $\hat{\omega}$ spectrums of the CKinCH standard case solved by the eigenvalue solver of rCYCLO [32]. Only the $k_x > 0$ and $k_y > 0$ modes are presented.

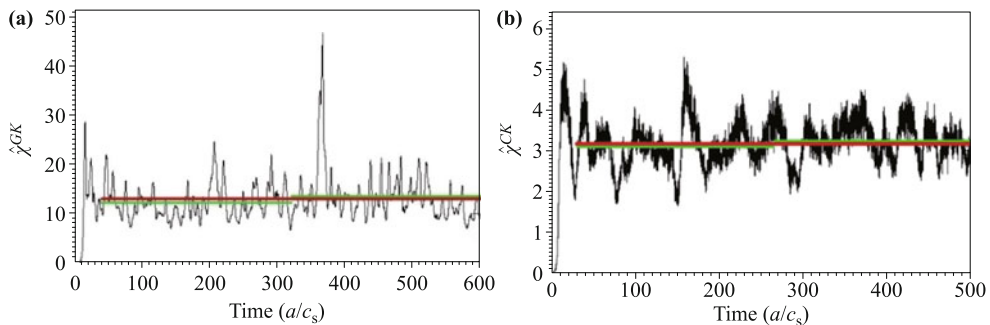


Fig. 11 The time evolution of turbulent energy diffusivity of (a) GK and (b) CKinCH standard case. The average energy diffusivity over the saturated period of time is (a) 13.1 ± 0.1 for GK, (b) 3.18 ± 0.07 for CKinCH. The red and green lines represent the average over all the saturated time and the half period of saturated time respectively.

trum of $\hat{\chi}^{CK}$ and $|\hat{\phi}|^2$ of the CKinCH standard case during the saturation period, which clearly shows the low-frequency drift-wave modes and the four harmonics of high-frequency ion cyclotron modes with $\hat{\omega}$ close to ± 10 , and ± 20 . The linearly stable high-frequency IC modes are nonlinearly driven by the low-frequency unstable drift modes, which satisfy the wave-wave coupling condition. The low-frequency unstable drift modes account for most (e.g., 87% within $|\hat{\omega}| \leq 2$) of the transport.

The two types of low-frequency drift modes, ion temperature gradient (ITG) modes and collisional drift-wave (CDW) modes, are described in Fig. 13(a). It shows the standard case and fixes $\hat{k}_x = 0$ and $\hat{k}_y = 0.45$ with damping $\mu_{LK} = 0$ and $\mu_{HK} = 0$. The negative frequency ITG modes are slightly unstable and nearly independent of α_A (the growth rate of the ITG modes $\hat{\gamma}_{ITG}$ has been multiplied by 10 in Fig. 13(a)). The positive frequency CDW modes are the most unstable modes. The low-collisional (large α_A) electron modes approach the adiabatic limit,

while the highly collisional (small α_A) electron modes transform to the more unstable resistive-g modes at very small α_A . Since the growth rates of the CDW modes decrease much faster than the ITG modes when \hat{k}_x and \hat{k}_y increase, the dominant modes will switch from the CDW modes to the ITG modes when either \hat{k}_x or \hat{k}_y increases over 1.0. The jumps in the frequency spectrum shown in Fig. 10(b) illustrate this mode-switch phenomenon. The nonlinear turbulent transport level of gyrokinetics increases faster than that of cyclokinetics with decreasing α_A , as illustrated in Fig. 13(b).

4.2 Simulation results with stable ion cyclotron modes

4.2.1 Linear rates

The linear growth rates and frequencies of gyrokinetics recover the growth rates and frequencies of cyclokinetics in the low-frequency regime, as shown in Figs. 14(a) and (b). The cyclokinetic ion cyclotron (IC) modes are stable,

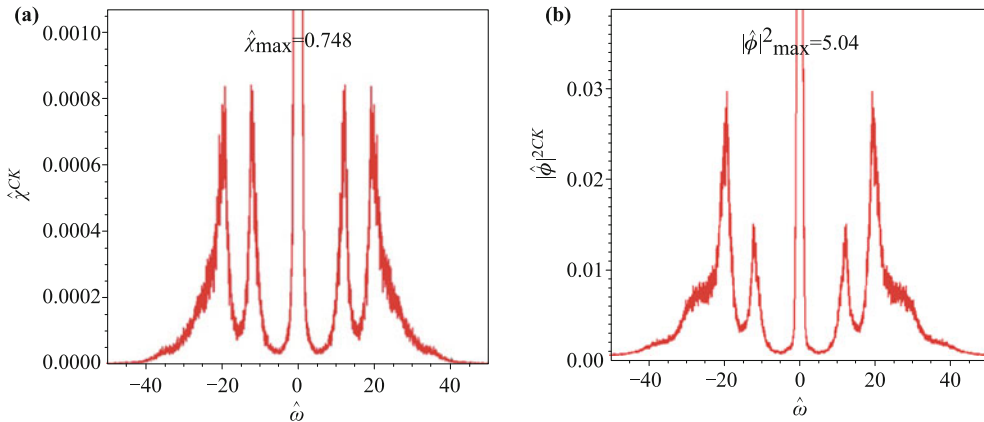


Fig. 12 The frequency spectrum for the CKinCH standard case during the saturated time. (a) $\hat{\chi}^{CK}$ versus $\hat{\omega}$, and (b) $|\hat{\phi}|^2$ versus $\hat{\omega}$. The drift-wave modes ($\hat{\omega}$ close to 0) and the four harmonics of the high-frequency IC modes ($\hat{\omega}$ close to ± 10 , and ± 20) are clearly shown.

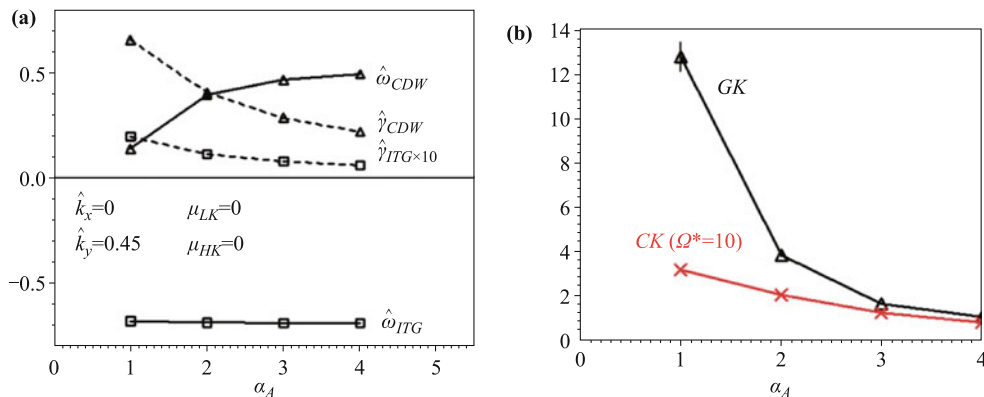


Fig. 13 (a) The low-frequency drift mode growth rate $\hat{\gamma}$ and frequency $\hat{\omega}$ of the standard CKinCH case versus α_A at the fixed point $\hat{k}_x = 0$ and $\hat{k}_y = 0.45$ with damping $\mu_{LK} = 0$ and $\mu_{HK} = 0$. The frequency of ITG modes $\hat{\omega}_{ITG}$ is negative and the corresponding growth rate $\hat{\gamma}_{ITG}$ is small [$\hat{\gamma}_{ITG}$ has been multiplied by 10 in (a)]. The CDW modes are the most unstable modes and their frequency $\hat{\omega}_{CDW}$ is positive. CDW modes will switch to more unstable resistive-g modes with the smaller α_A . (b) The energy diffusivity of gyrokinetics $\hat{\chi}^{GK}$ and cyclokinetics $\hat{\chi}^{CK}$ at $\Omega^* = 10$ versus α_A .

as shown in Fig. 14(a). In the cyclokinetic simulations, the turbulent energy is drained from the unstable drift modes to the stable IC modes. Figure 14(b) illustrates that the frequency of $n = \pm 1$ harmonics are around ∓ 10 . The IC mode frequency deviates from -10 at $k_y > 1.0$, which is caused by the linear coupling to the low-frequency drift modes.

4.2.2 Nonlinear simulation results

At sufficiently large Ω^* and sufficiently low turbulence levels the nonlinear gyrokinetic simulations have recovered the cyclokinetic transport levels, as shown in Fig. 15(a). The transport level of cyclokinetics is lower than the gyrokinetic transport level at low- Ω^* values. The lower cyclokinetic transport level results from the turbulent energy being drained to the less unstable IC modes (shown in Fig. 14(a)). The cyclokinetic nonlinear coupling is enhanced at low velocity by the $1/\hat{v}_\perp$ factor in Eqs. (2.2.11) and (2.2.12). Figure 15(a) is nearly identical to Fig. 8(b) in Section 3.6 that was obtained by performing CKinFH simulations with the same standard grid pa-

rameters, confirming that the numerical CKinCH simulations recover both the linear and nonlinear CKinFH simulations in Ref. [32]. Figure 15(b) shows the time average of the turbulence level $|\delta n/n_0|$ versus Ω^* . In gyrokinetic simulations, $|\delta n/n_0|_{GK} \propto 1/\Omega^* = \rho^*$. The black circles in Fig. 15(b) mark the points at which the gyrokinetics formalism starts to break down. The breakdown condition is formulated as $|\hat{\chi}^{GK} - \hat{\chi}^{CK}|/\hat{\chi}^{CK} > 5\%$. Figure 15(b) indicates that the gyrokinetics formalism starts to break down when

$$|\delta n/n_0| > 20\%. \quad (4.2.1)$$

The turbulence level $|\delta n/n_0|$ is chosen to quantify the breakdown condition, because it is easily measured experimentally.

However, theoretical physicists are more concerned with the frequency scope of gyrokinetics. The low-frequency gyrokinetic approximation requires the nonlinear perturbed $E \times B$ frequency to be much smaller than the ion cyclotron frequency. Ref. [39] gives a simple definition of the frequency ratio of the nonlinear perturbed $E \times B$ frequency over the ion cyclotron frequency:

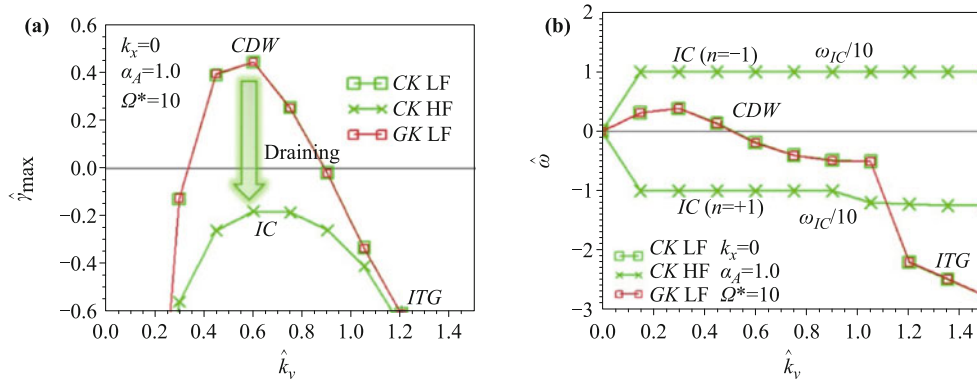


Fig. 14 (a) Linear growth rates and (b) the corresponding frequencies of GK, CKinCH low-frequency (LF) modes and CKinCH high-frequency (HF) modes at the fixed $k_x = 0$ of standard case. The frequencies of IC $n = -1, +1$ harmonics are divided by 10 in (b).

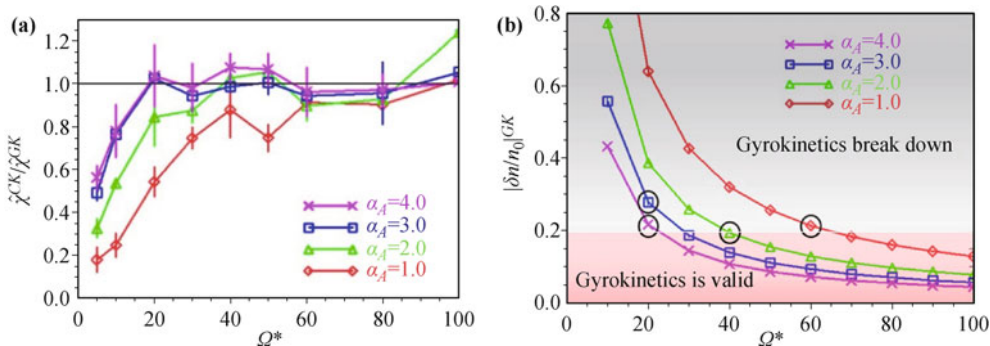


Fig. 15 (a) The energy diffusivity ratio of CKinCH over gyrokinetics versus Ω^* . The transport level of CKinCH recovers gyrokinetics at high- Ω^* values and low turbulence levels. Cyclokinetic transport level is lower than gyrokinetics at low- Ω^* values and high turbulence levels. (b) The time average of turbulence level $|\delta n/n_0|$ versus Ω^* . The black circles mark where gyrokinetics starts to break down, which indicates that gyrokinetics starts to break down when $|\delta n/n_0| > 20\%$.

$$\begin{aligned}
 |\omega_{NL}/\Omega| &= (1/N_k) \sum_k |\mathbf{k} \cdot \delta \mathbf{v}_E|/\Omega \\
 &= (1/N_k) \sum_k |(\mathbf{k}\rho) \cdot (\delta \mathbf{v}_E/v_i^{th})| \\
 &= (\rho^*/N_k) \sum_k |Re[(-i) \sum_{k1} \hat{\mathbf{k}} \cdot \hat{\mathbf{k}}_1 \times \hat{b} \delta \hat{\phi}_{k1}]|,
 \end{aligned} \tag{4.2.2}$$

which is also proportional to ρ^* like $|\delta n/n_0|$. Ω is the ion cyclotron frequency. Ref. [39] indicates that as to the definition in Eq. (4.2.2) the gyrokinetics formalism starts to break down at $|\omega_{NL}/\Omega| > 45\%$.

Note that the definition in Eq. (4.2.2) is not a good choice for representing the nonlinear $E \times B$ frequency of a turbulence system, because it averages over the k spectrum directly but ignores the distribution of the amplitude in the k spectrum. Figure 16 shows that higher k modes exhibit larger nonlinear $E \times B$ frequency, while the amplitude is much smaller. Obviously, the frequency ratio is better defined as the nonlinear perturbed $E \times B$ frequency, shown in Fig. 16(b), by multiplying a weight W_k proportional to the amplitude shown in Fig. 16(a):

$$\begin{aligned}
 |\omega_{NL}/\Omega| &= \sum_k W_k |\mathbf{k} \cdot \delta \mathbf{v}_E|/\Omega \\
 &= \rho^* \sum_k W_k |Re[(-i) \sum_{k1} \hat{\mathbf{k}} \cdot \hat{\mathbf{k}}_1 \times \hat{b} \delta \hat{\phi}_{k1}]|,
 \end{aligned} \tag{4.2.3}$$

where the weight is defined as

$$W_k = \frac{(\delta \hat{\phi}_k)^2}{\sum_k (\delta \hat{\phi}_k)^2}. \tag{4.2.4}$$

Figure 17 shows that, as to the definition in Eq. (4.2.3), the gyrokinetics formalism starts to break down when

$$|\omega_{NL}/\Omega| > 20\%. \tag{4.2.5}$$

4.2.3 Physical explanations of the simulation results

The cyclokinetic small $\Omega^* = 1/\rho^*$ stabilizing effect on

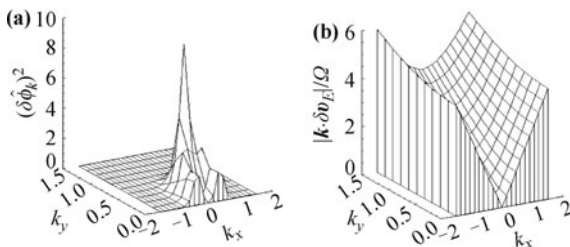


Fig. 16 (a) The k spectrum of the perturbed field amplitude of the gyrokinetic turbulence. (b) The frequency ratio of the nonlinear perturbed $E \times B$ frequency over the ion cyclotron frequency in the k spectrum. Standard case is presented, and both (a) and (b) average over the saturated time period.

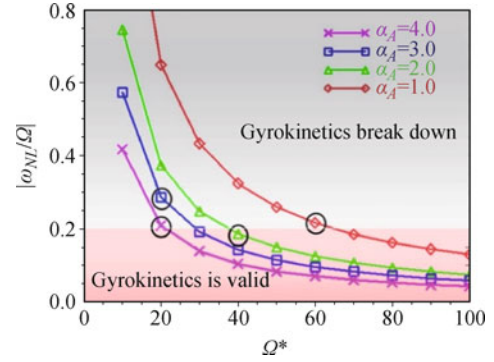


Fig. 17 The frequency ratio of the nonlinear perturbed $E \times B$ frequency over the ion cyclotron frequency versus Ω^* . The definition is given by Eq. (4.2.3). The black circles mark where gyrokinetics starts to break down, which indicates that gyrokinetics starts to break down when $|\omega_{NL}/\Omega| < 20\%$.

gyrokinetics from coupling to stable high-frequency modes is analogous to the global gyrokinetic large ρ^* stabilizing effect from nonlocal turbulence spreading (NTS) [51]. Both L-mode and H-mode DIII-D simulations [52] with the GYRO code show that the NTS mechanism breaking the gyroBohm scaling is caused by the nonlocal drainage of turbulence from the unstable radii and spreading to the stable (or less unstable) radii. At larger ρ^* , where small “local” eddies become large “global” eddies, there is a transition from the gyroBohm scaling $\chi_{gB} = (c_s/a)\rho_s^2$ to the Bohm scaling $\chi_B = \chi_{gB}/\rho^* = \chi_{gB}\Omega^*$. At smaller Ω^* , cyclokinetic transitions in a similar way. The turbulence is drained in the frequency space rather than in the radial space from the unstable low-frequency domain, and spreads into the less unstable high-frequency domain. The NTS paradigm for breaking the gyroBohm scaling in the unstable regions $\chi = \hat{\chi}(0)\chi_{gB}(1 - \rho^*/\rho_{crit}^*)$ is represented by Fig. 18(a), which is taken from Ref. [52]. The cyclokinetic high-frequency stabilization can be written analogously $\hat{\chi}^{CK} = \hat{\chi}^{GK}(1 - \Omega_{crit}^*/\Omega^*)$ as shown in Fig. 18(b). The value of Ω_{crit}^* increases when the turbulence level increases, as shown in Fig. 15(a). Furthermore, in the stable (or less unstable) region, where the local gyroBohm diffusivity is expected to be smaller, the radially nonlocal NTS mechanism can be represented by $\chi = \hat{\chi}(0)\chi_{gB}(1 + \rho^*/\rho_{crit}^*)$ [52]. It has a contribution from the super-gyroBohm to gyroBohm χ_{gB} . Thus, the transport level is higher than the local gyroBohm because the turbulence spreads into these less unstable radii from the more unstable radii. This suggests that if the cyclokinetic high-frequency IC modes are driven to become sufficiently unstable, it might be reasonable to expect that $\hat{\chi}^{CK} = \hat{\chi}^{GK}(1 + \Omega_{crit}^*/\Omega^*)$ with the cyclokinetic low-frequency mode transport level possibly higher than gyrokinetics, because the directions of draining and

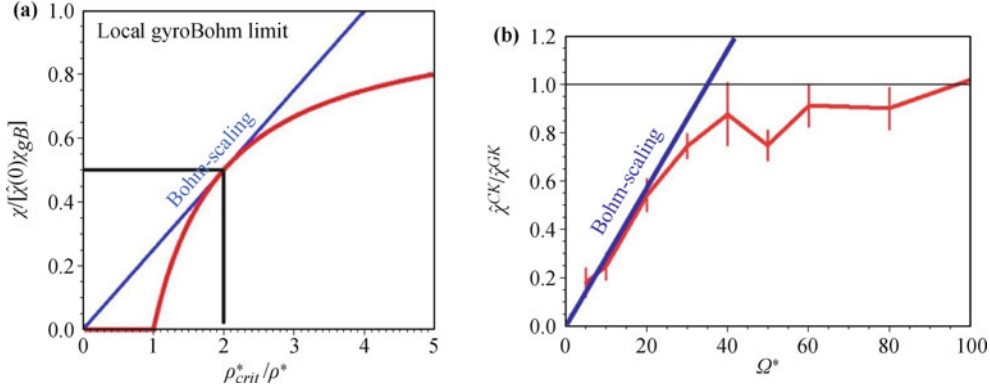


Fig. 18 (a) is from Ref. [52] which shows the rule for breaking gyroBohm scaling by the NTS mechanism. Global gyrokinetic energy diffusivity normalized by gyroBohm level at $\rho^* \Rightarrow 0$ vs. ρ_{crit}^*/ρ^* . (b) Local gyrokinetic energy diffusivity normalized by gyrokinetic diffusivity vs. Ω^* , which indicates that the gyrokinetics has the similar rule for breaking gyroBohm scaling by nonlocal turbulence spreading in frequency space.

spreading might be reversed.

4.3 Simulation results with unstable ion cyclotron modes

4.3.1 Unstable IC modes

In order to obtain the unstable high-frequency IC modes, an artificial driving term $n\gamma_{IC}H(\hat{k}_y)\delta\hat{F}_k^n$ is added to the $n = -1$ and $+1$ harmonics of Eq. (2.2.2) or equivalently Eq. (2.2.12). $H(\hat{k}_y) = -1.778\hat{k}_y^2 + 2.667|\hat{k}_y|$ is a model function with the maximal value $H(\hat{k}_y)|_{\max} = 1.0$ at $\hat{k}_y = 0.75$. The factor γ_{IC} is a constant and represents the maximal driving rate added on the IC modes. Thus, the high-frequency IC modes can be driven unstable without affecting the low-frequency drift modes, as shown in Fig. 19. The same artificial damping rates $\mu_{HK}\hat{k}^4$ and μ_{LK}/\hat{k}^2 of the drift wave modes are added to the IC modes. Note that the gyrokinetic transport level is insensitive to these damping rates of the IC modes as long as the IC modes are less unstable than the low-

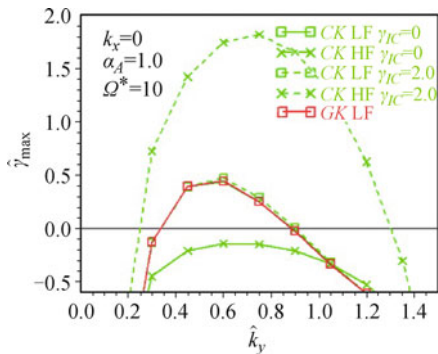


Fig. 19 Linear growth rates of GK, CKinCH low-frequency (LF) modes and CKinCH high-frequency (HF) modes with $\gamma_{IC} = 0$ and 2.0 at the fixed $\hat{x} = 0$ of standard case.

frequency drift modes.

4.3.2 Nonlinear simulation results

Figures 20(a) and (b) show the γ_{IC} parametric dependence of the energy diffusivity ratio $\hat{\chi}^{CK}/\hat{\chi}^{GK}$ and the electrostatic energy ratio $\hat{E}^{CK}/\hat{E}^{GK}$ at $\Omega^* = 10$. The turbulence electrostatic energy is defined as

$$\hat{E} = \frac{1}{2} \sum_k \hat{k}^2 \delta\hat{\phi}_k^* \delta\hat{\phi}_k, \quad (4.3.1)$$

with $\hat{\chi}^{GK}$ and \hat{E}^{GK} constant with respect to γ_{IC}/Ω^* . There are two different regimes for each curve, and a jump of $\hat{\chi}^{CK}/\hat{\chi}^{GK}$ between the two regimes, but no jump of $\hat{E}^{CK}/\hat{E}^{GK}$ (with the minor exception at $\alpha_A = 4$). Notice that the $\hat{\chi}^{CK}$ value can be driven higher than $\hat{\chi}^{GK}$.

In order to illustrate the jump, more details of the $\alpha_A = 2$ case are provided in Figs. 20(a) and (b). Figures 20(c) and (d) show the γ_{IC} parametric dependence of the ratio $\hat{\chi}^{CK}/\hat{\chi}^{GK}$ and $\hat{E}^{CK}/\hat{E}^{GK}$ contributed by the high-frequency modes and low-frequency modes, respectively. The jump is obtained (at all Ω^*) when the maximal high-frequency (HF) driving rate is about twice the maximal low-frequency (LF) driving rate (e.g., the jump of the $\alpha_A = 2$ curve occurs when γ_{IC}/Ω^* is between 0.078 and 0.085 as shown in Fig. 20(c) where the LF driving rate is 0.44 and the HF driving rate is in the 0.78–0.85 range). Before the jump (γ_{IC} below 0.078), about 90% of transport is generated by the low-frequency ($|\hat{\omega}| \leq 2$) modes and about 10% is caused by the high-frequency ($|\hat{\omega}| > 2$) modes. Then, the transport contributed by the high-frequency modes increases to about 90%, and the transport contributed by the low-frequency modes decreases to about 10% in the jump regime of γ_{IC}/Ω^* from 0.078 to 0.085 in Fig. 20(c). After the jump (γ_{IC} above 0.085),

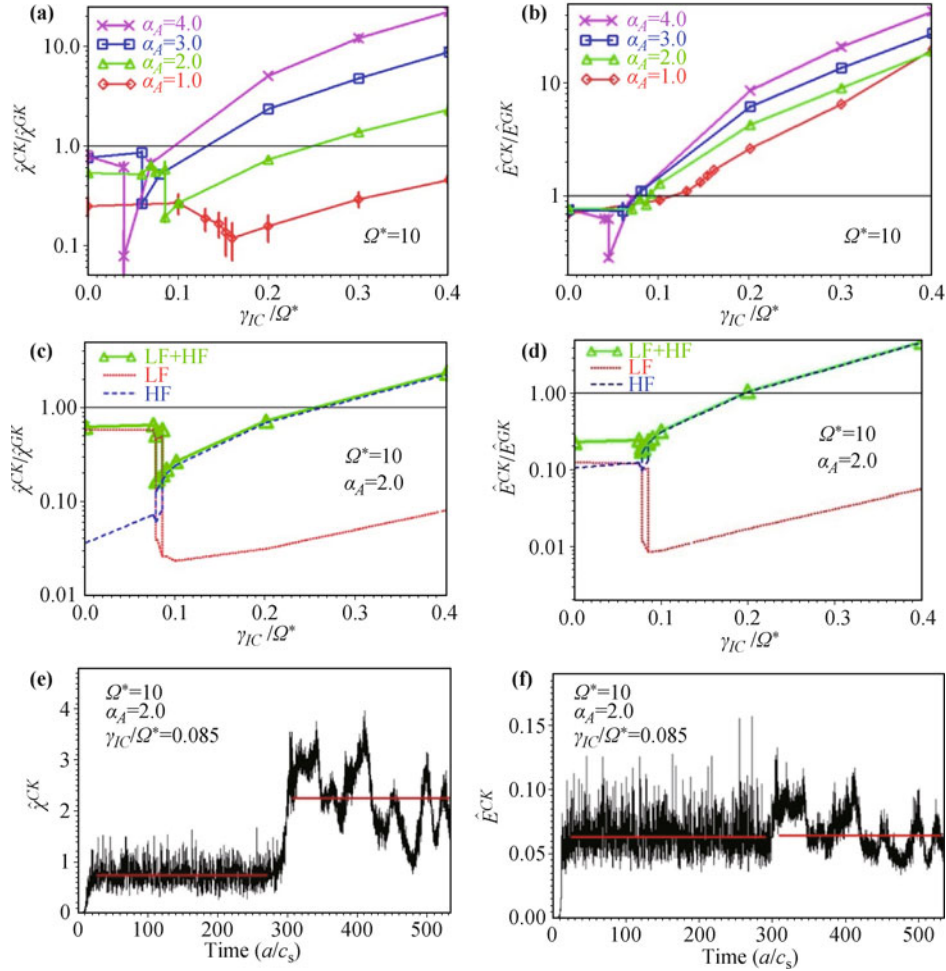


Fig. 20 (a) and (b) show the energy diffusivity ratio $\hat{\chi}^{CK}/\hat{\chi}^{GK}$ and the electrostatic energy ratio $\hat{E}^{CK}/\hat{E}^{GK}$ of CKinCH over gyrokinetics versus γ_{IC}/Ω^* at $\Omega^* = 10$. There are two different regimes for each curve and a jump of $\hat{\chi}^{CK}/\hat{\chi}^{GK}$ between the two regimes but no jump of $\hat{E}^{CK}/\hat{E}^{GK}$ with minor exception at $\alpha_A = 4$. $\hat{\chi}^{GK}$ and \hat{E}^{GK} are constant with respect to γ_{IC}/Ω^* . (c) and (d) describe the high-frequency component (by the blue dash curve) and low-frequency component (by the red dot curve) of $\hat{\chi}^{CK}/\hat{\chi}^{GK}$ and $\hat{E}^{CK}/\hat{E}^{GK}$ versus γ_{IC}/Ω^* at $\alpha_A = 2$ and $\Omega^* = 10$. The green curves represent the summation of low-frequency and high-frequency components. $\gamma_{IC}/\Omega^* = 0$ to 0.078 are the dominantly low-frequency drift mode regimes. $\gamma_{IC}/\Omega^* = 0.078$ to 0.085 correspond to the jump regimes. $\gamma_{IC}/\Omega^* = 0.085$ to 0.4 are the dominantly high-frequency IC mode regimes. The high-frequency component of $\hat{\chi}^{CK}$ can exceed $\hat{\chi}^{GK}$, but the low-frequency component cannot. (e) and (f) illustrate $\hat{\chi}^{CK}$ and \hat{E}^{CK} versus time at $\gamma_{IC}/\Omega^* = 0.085$, $\alpha_A = 2$ and $\Omega^* = 10$. The turbulence saturates to two steady states respectively during time period 21–270 a/c_s and 312–534 a/c_s . The red lines represent the time average of each state. There is a jump of $\hat{\chi}^{CK}$, while there is no jump of \hat{E}^{CK} .

$\hat{\chi}^{CK}$ increases quite rapidly with increasing γ_{IC} in the dominantly high-frequency mode regime of γ_{IC}/Ω^* , from 0.09 to 0.4 in Fig. 20(c). Before the jump, the turbulence is drained from the unstable low-frequency domain and spreads into the less unstable high-frequency domain. After the jump, the turbulence is drained from the more unstable high-frequency domain and spreads into the less unstable low-frequency domain. The jump location corresponds to the point at which the directions of draining and spreading are reversed. The rapid increase in the cyclokinetic transport after the jump in Fig. 20(c) is contributed by the high-frequency IC modes, which are

directly driven by γ_{IC} . The high-frequency IC modes contribute more than 90% of transport in this regime. When γ_{IC} increases to a large value, the high-frequency IC modes are much more unstable than the low-frequency drift modes. The transport of cyclokinetics will become much larger than that of gyrokinetics (e.g., 2.3-fold larger for $\gamma_{IC}/\Omega^* = 0.4$ and $\alpha_A = 2$). More importantly, the high-frequency component of $\hat{\chi}^{CK}$ can exceed $\hat{\chi}^{GK}$, but the low-frequency component of $\hat{\chi}^{CK}$, which is associated with the “short-fall”, is still much smaller than $\hat{\chi}^{GK}$, as shown in Fig. 20(c). Only the low-frequency component transport is important in this work, because

only the low-frequency turbulence is measured in experiments [26].

To explain the reduction in the high-frequency gyrokinetic transport, we combine Eq. (2.2.5) with the linear part of Eq. (2.5.2), and the diffusivity is proportional to the diffusivity correlation phase factor, so that $\hat{\chi} \propto \hat{D} \propto \sum_k \hat{E}C(\hat{\omega})$. The phase factor $C(\hat{\omega})$ is a strong function of the frequency, $C(\hat{\omega}) = (\hat{k}_y/\hat{k}^2)[\alpha_A(\hat{\omega}_*^n - \hat{\omega}) + \hat{\gamma}(\hat{\omega}_*^n - \hat{\omega}_d^e)]/[(\alpha_A + \hat{\gamma})^2 + (\hat{\omega} - \hat{\omega}_d^e)^2]$, which is roughly proportional to $1/\hat{\omega}$ for large $\hat{\omega}$. Thus, the low-frequency component has a large phase factor, and the high-frequency component has a small phase factor. When the directions of draining and spreading are reversed, \hat{E}^{CK} is overall unchanged but is redistributed from low-frequency modes to high-frequency modes. When the energy is transferred from low-frequency modes to high-frequency modes, the gyrokinetic transport level $\hat{\chi}^{CK}$ will decrease.

Bifurcated turbulent transport states are always found in the jump regimes for $\alpha_A = 2, 3, 4$ (but not for $\alpha_A = 1$). These two nonlinear gyrokinetic saturated states are associated with two different basins of attraction, which could be considered analogous to Lorenz attractors [53]. Figure 20(e) illustrates that the turbulence first saturates at a low-level state, in which the high-frequency modes occupy 85% of the transport during the time period 21–270 a/c_s . Then, the turbulence level jumps and saturates at a higher level state in the time period 312–534 a/c_s , in which the low-frequency modes occupy 85% of the transport. Figure 20(f) shows that the gyrokinetic electrostatic energy \hat{E}^{CK} saturates at the same two states, but without an overall jump.

4.3.3 More physical case

A physically reasonable IC drive rate $\hat{\gamma}/\Omega^* \cong 0.3(T_e/T_i)v_D/v_e^{th}$ was given in Eq. (8) in the early work by Drummond and Rosenbluth [34] on current drift driven ion cyclotron modes. Here, v_e^{th} is the electron thermal velocity, and v_D is the electron current drift velocity relative to the stationary ions. A maximal value of $v_D/v_e^{th} = 5$ corresponds to a growth rate of $\hat{\gamma}/\Omega^* = 0.025$ (for $T_e = T_i$ and deuterium). This growth rate is not sufficiently large for driving either LF or HF gyrokinetic turbulence levels higher than those of gyrokinetics at $\Omega^* = 10$, as shown in Fig. 9(a). The value $\gamma_{IC}/\Omega^* = 0.025$ is even well below the jump regime between 0.078 and 0.085.

For a more physically relevant ion cyclotron frequency value $\Omega^* = 50$, the jump occurs again, as shown in Fig. 21, when the maximal high-frequency driving rate is about twice the maximal low-frequency driving rate. However, the IC driving rate $\hat{\gamma}/\Omega^* = 0.025$ is still not

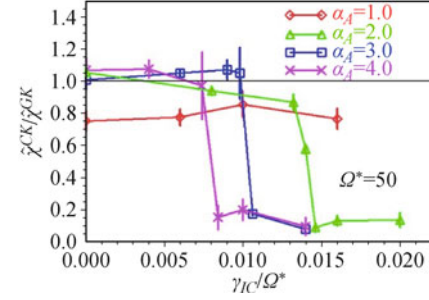


Fig. 21 The energy diffusivity ratio of CKinCH over gyrokinetics versus γ_{IC}/Ω^* at $\Omega^* = 50$.

sufficiently large for driving either LF or HF gyrokinetic turbulent transport higher than that of gyrokinetics. Thus, the L-mode near-edge “short-fall” is not caused by the nonlinear coupling between low-frequency drift motion and high-frequency ion cyclotron motion. At large Ω^* values ($\Omega^* \geq 50$), the high-frequency IC modes are decoupled from the low-frequency drift modes. The nonlinear interaction is no longer strong enough for saturating the very unstable IC modes for $\gamma_{IC}/\Omega^* > 0.02$.

5 Discussion

5.1 Controversy regarding the L-mode near-edge transport “short-fall” problem

Although the “L-mode near-edge short-fall” has been well studied since its first discovery in 2007 [29], there remain a significant number of controversies regarding the “short-fall” problem. Some research suggests that the transport “short-fall” problem does not always exist. GYRO simulations of the outer core region of Alcator C-Mod L-mode yield under-prediction for Q_e but not for Q_i [54–56]. This Q_e under-prediction is apparently attributed to the lack of the high- k electron scale physics in the simulations. A recent multi-scale simulation that includes the electron temperature gradient (ETG) increased Q_e to 30%, which remained insufficient for compensating the under-prediction of Q_e [57]. Continuum Eulerian gyrokinetic code GENE simulations of the L-mode plasma in the ASDEX Upgrade Tokamak suggest that the transport “short-fall” is likely to disappear when a/L_{Ti} is increased by 15%, within the experimental measurement uncertainty [58]. The particles in the cell gyrokinetic code GEM simulations yielded the transport “short-fall” outcome compared with the L-mode transport in the DIII-D experiment, but did not yield “short-fall” when compared with the C-Mod experiment [59], within the range of experimental error (this could occur owing to the insufficient strong turbulence

in the L-mode near-edge of C-Mod). These inconsistent results regarding the “short-fall” problem observations actually should be attributed to coding differences, because different simulation packages use different numerical techniques and approximation methods. The ongoing work by Dr. Crist Holland is still trying to compare the transport “short-fall” phenomena across different simulation packages. Waltz and Zhao are trying to add more information to help resolve the “short-fall” problem, if it exists. More importantly, the present work answers a more general question of the gyrokinetic approximation breakdown condition.

Note that the gyrokinetic approximation breakdown conditions (on the turbulence level being about 20% and the ratio of the nonlinear $E \times B$ frequency to the ion cyclotron frequency being about 20%) that were obtained in this work are idealized results. The physical processes in actual experiments are much more complicated. The breakdown critical values in this work result from the physical process of the $E \times B$ nonlinearity interrupting the ion gyro-motion. Physical processes such as parallel nonlinearity and high- k ETG were not considered in the present work, because these processes were shown to be irrelevant or less important to the gyrokinetic breakdown issue.

Acknowledgements This work was supported by the National Natural Science Foundation of China under Grant Nos. 1126114032 and 10975012, ITER China under Grant No. 2013GB112006, as well as U.S. Department of Energy under GA-Grant No. DE-FG02-95ER54309 and IFS Grant No. DE-FG02-04ER54742.

Appendix A

A.1 Derivation of cyclokinetic equations

The derivation of the cyclokinetic equation [Eq. (2.1.14)] in the gyro-phase angle form, starting from the first principles Boltzmann equation (2.1.1), has already been described in Section 2. In this Appendix, we will derive the cyclokinetic equation by transforming the gyro-phase angle α to the harmonic number n . The steps leading from Eq. (2.1.14) to CKinFH equations (2.3.1), (2.3.2), and (2.3.3) are listed as below.

Some useful formulas are

$$\begin{aligned}\hat{\mathbf{v}}_{\perp} \cdot \hat{\mathbf{k}}_{\perp} &= \hat{v}_{\perp} \hat{k}_{\perp} \cos(\alpha - \beta) \\ &= (\hat{v}_{\perp} \hat{k}_{\perp} / 2) \{ \exp[i(\alpha - \beta)] + \exp[-i(\alpha - \beta)] \},\end{aligned}\quad (\text{A.1})$$

$$\begin{aligned}\hat{\mathbf{v}}_{\perp} \cdot \hat{\mathbf{k}}_1 &= \hat{v}_{\perp} \hat{k}_1 \cos(\alpha - \beta_1) \\ &= (\hat{v}_{\perp} \hat{k}_1 / 2) \{ \exp[i(\alpha - \beta_1)] + \exp[-i(\alpha - \beta_1)] \},\end{aligned}\quad (\text{A.2})$$

$$\begin{aligned}\hat{\mathbf{k}}_1 \cdot \hat{\mathbf{b}} \times \hat{\mathbf{v}}_{\perp} / \hat{v}_{\perp}^2 &= -(\hat{k}_1 / \hat{v}_{\perp}) \sin(\alpha - \beta_1) \\ &= i(\hat{k}_1 / 2\hat{v}_{\perp}) \{ \exp[i(\alpha - \beta_1)] - \exp[-i(\alpha - \beta_1)] \},\end{aligned}\quad (\text{A.3})$$

$$\hat{v}_{\perp} = \hat{\rho} = \sqrt{2(T_i / T_e)} \hat{\mu}. \quad (\text{A.4})$$

The discrete Fourier transform is defined as follows:

$$\delta \hat{f}_k(\hat{\mu}, \alpha) = \sum_{n=-N_{\alpha}+1}^{n=N_{\alpha}-1} \delta \hat{F}_k^n(\hat{\mu}) \exp(in\alpha). \quad (\text{A.5})$$

Where $n = -N_{\alpha} + 1, \dots, 0, \dots, N_{\alpha} - 1$ are the Fourier harmonic numbers. The corresponding inverse discrete Fourier transform is

$$\delta \hat{F}_k^n(\hat{\mu}) = \frac{1}{2N_{\alpha} - 1} \sum_{m=0}^{m=2N_{\alpha}-2} \delta \hat{f}_k(\hat{\mu}, \alpha_m) \exp(-in\alpha_m). \quad (\text{A.6})$$

where $\alpha_m = 2\pi m / (2N_{\alpha} - 1)$. For convenience, the non-conservative form of the cyclokinetic equation [Eq. (2.1.14)] in the gyro-angle phasespace is rewritten here:

$$\begin{aligned}D\delta \hat{f}_k / D\hat{t} - i\hat{\omega}_k^d \delta \hat{g}_k + i\hat{\mathbf{v}}_{\perp} \cdot \hat{\mathbf{k}} \Omega_* \delta \hat{g}_k - \Omega_* \partial_{\alpha} \delta \hat{g}_k \\ = -i\hat{\omega}_{*k}^{nT} \delta \hat{\phi}_k n_0 F_M(\hat{\mu}) \\ + \sum_{k1} [(T_e / T_i) \delta \hat{\phi}_{k1} i\hat{\mathbf{k}}_1 \cdot \hat{\mathbf{v}}_{\perp} \partial_{\hat{\mu}} \delta \hat{f}_{k2} \\ + \delta \hat{\phi}_{k1} i\hat{\mathbf{k}}_1 \cdot \hat{\mathbf{b}} \times \hat{\mathbf{v}}_{\perp} / \hat{v}_{\perp}^2 \partial_{\alpha} \delta \hat{f}_{k2}].\end{aligned}\quad (\text{A.7})$$

The conservative form (A.8) is obtained by substituting Eq. (2.1.15) into Eq. (A.7):

$$\begin{aligned}D\delta \hat{f}_k / D\hat{t} - i\hat{\omega}_k^d \delta \hat{g}_k + i\hat{\mathbf{v}}_{\perp} \cdot \hat{\mathbf{k}} \Omega_* \delta \hat{g}_k - \Omega_* \partial_{\alpha} \delta \hat{g}_k \\ = -i\hat{\omega}_{*k}^{nT} \delta \hat{\phi}_k n_0 F_M(\hat{\mu}) \\ + \sum_{k1} \partial_{\hat{\mu}} [(T_e / T_i) \delta \hat{\phi}_{k1} i\hat{\mathbf{k}}_1 \cdot \hat{\mathbf{v}}_{\perp} \delta \hat{f}_{k2}] \\ + \sum_{k1} \partial_{\alpha} (\delta \hat{\phi}_{k1} i\hat{\mathbf{k}}_1 \cdot \hat{\mathbf{b}} \times \hat{\mathbf{v}}_{\perp} / \hat{v}_{\perp}^2 \delta \hat{f}_{k2}),\end{aligned}\quad (\text{A.8})$$

where the Doppler drift $\hat{\omega}_k^E$ is ignored.

A.1.1 The derivation of linear terms

We now expand the $\delta \hat{f}_k(\hat{\mu}, \alpha)$ and $\delta \hat{g}_k(\hat{\mu}, \alpha)$ terms in Eq. (A.7) by using the inverse Fourier transform in Eq. (A.6), as follows.

The first term is

$$\frac{1}{2N_{\alpha} - 1} \sum_{m=0}^{m=2N_{\alpha}-2} D\delta \hat{f}_k / D\hat{t} \exp(-in\alpha_m) = D\delta \hat{F}_k^n / D\hat{t}.$$

The second term is

$$\frac{1}{2N_{\alpha} - 1} \sum_{m=0}^{m=2N_{\alpha}-2} -i\hat{\omega}_k^d \delta \hat{g}_k \exp(-in\alpha_m) = -i\hat{\omega}_k^d \delta \hat{G}_k^n.$$

The third term is

$$\begin{aligned} & \frac{1}{2N_\alpha - 1} \sum_{m=0}^{m=2N_\alpha-2} \mathbf{i}\hat{\mathbf{v}}_\perp \cdot \hat{\mathbf{k}} \Omega_* \delta \hat{g}_k \exp(-i n \alpha_m) \\ &= \frac{1}{2N_\alpha - 1} \sum_{m=0}^{m=2N_\alpha-2} \mathbf{i} \Omega_*(k\rho/2) \{ \exp[i(\alpha - \beta)] \\ & \quad + \exp[-i(\alpha - \beta)] \} \\ & \quad \cdot \left[\sum_{n'=-N_\alpha+1}^{n'=N_\alpha-1} \delta \hat{G}_k^{n'} \exp(in' \alpha_m) \right] \exp(-i n \alpha_m) \\ &= \mathbf{i} \Omega_*(k\rho/2) [\exp(-i\beta) \delta \hat{G}_k^{n-1} + \exp(i\beta) \delta \hat{G}_k^{n+1}]. \end{aligned}$$

The fourth term is

$$\begin{aligned} & \frac{1}{2N_\alpha - 1} \sum_{m=0}^{m=2N_\alpha-2} -\Omega_* \partial_\alpha \delta \hat{g}_k \exp(-i n \alpha_m) \\ &= -i n \Omega_* \delta \hat{G}_k^n. \end{aligned}$$

The fifth term is

$$\begin{aligned} & \frac{1}{2N_\alpha - 1} \sum_{m=0}^{m=2N_\alpha-2} -i \hat{\omega}_{*k}^{nT} \delta \hat{\phi}_k n_0 F_M(\hat{\mu}) \exp(-i n \alpha_m) \\ &= -i \hat{\omega}_{*k}^{nT} \delta \hat{\phi}_k n_0 F_M(\hat{\mu}) \delta_0^n. \end{aligned}$$

This completes the derivation of all linear terms of CKinFH.

$$\begin{aligned} & D \delta \hat{F}_k^n / D\hat{t} - i \hat{\omega}_k^d \delta \hat{G}_k^n + i k \rho \Omega_* / 2 [\exp(-i\beta) \delta \hat{G}_k^{n-1} \\ & \quad + \exp(i\beta) \delta \hat{G}_k^{n+1}] - i n \Omega_* \delta \hat{G}_k^n + i \hat{\omega}_{*k}^{nT} \delta \hat{\phi}_k (n_0 F_M) \delta_0^n \\ &= \frac{1}{2N_\alpha - 1} \sum_{m=0}^{m=2N_\alpha-2} \partial_\alpha N L_k^n(\hat{\mu}) \exp(-i n \alpha_m) \\ & \quad + \frac{1}{2N_\alpha - 1} \sum_{m=0}^{m=2N_\alpha-2} \partial_\mu N L_k^n(\hat{\mu}) \exp(-i n \alpha_m). \quad (\text{A.9}) \end{aligned}$$

The RHS in the above equation represents the unpacked nonlinear terms.

A.1.2 The derivation of non-conservative nonlinear terms

The ∂_α term is derived as follows:

$$\begin{aligned} & \frac{1}{2N_\alpha - 1} \sum_{m=0}^{m=2N_\alpha-2} \partial_\alpha N L_k^n(\hat{\mu}) \exp(-i n \alpha_m) \\ &= \frac{1}{2N_\alpha - 1} \sum_{m=0}^{m=2N_\alpha-2} \sum_{k_1} \delta \hat{\phi}_{k_1} \mathbf{i} \hat{\mathbf{k}}_1 \cdot \hat{\mathbf{b}} \\ & \quad \times \hat{\mathbf{v}}_\perp / \hat{v}_\perp^2 \partial_\alpha \delta f_{k_2} \exp(-i n \alpha_m) \\ &= \frac{1}{2N_\alpha - 1} \sum_{k_1} \sum_{m=0}^{m=2N_\alpha-2} \hat{k}_1 \delta \hat{\phi}_{k_1} \mathbf{i}^2 / (2\hat{v}_\perp) \\ & \quad \times [\exp(i\alpha_m) \exp(-i\beta_1) - \exp(-i\alpha_m) \exp(i\beta_1)] \end{aligned}$$

$$\begin{aligned} & \cdot (in') \left\{ \sum_{n'=-N_\alpha+1}^{n'=N_\alpha-1} \delta \hat{F}_{k_2}^{n'} \exp(in' \alpha_m) \right\} \exp(-i n \alpha_m) \\ &= \sum_{k_1} -i \delta \hat{\phi}_{k_1} \hat{k}_1 / (2\hat{v}_\perp) [(n-1) \exp(-i\beta_1) \delta \hat{F}_{k_2}^{n-1} \\ & \quad - (n+1) \exp(i\beta_1) \delta \hat{F}_{k_2}^{n+1}]. \quad (\text{A.10}) \end{aligned}$$

In the first step of the above process, $\partial_\alpha N L_k^n(\hat{\mu})$ is replaced by the corresponding term in Eq. (A.7). In the second step of the above process, Eq. (A.3) is applied. In the last step of the above process, $n' = n-1$, $n' = n+1$ are set.

The ∂_μ term is derived as follows:

$$\begin{aligned} & \frac{1}{2N_\alpha - 1} \sum_{m=0}^{m=2N_\alpha-2} \partial_\mu N L_k^n(\hat{\mu}) \exp(-i n \alpha_m) \\ &= \frac{1}{2N_\alpha - 1} \sum_{m=0}^{m=2N_\alpha-2} \sum_{k_1} (T_e/T_i) \delta \hat{\phi}_{k_1} \mathbf{i} \hat{\mathbf{k}}_1 \\ & \quad \cdot \hat{\mathbf{v}}_\perp \partial_\mu \delta \hat{f}_{k_2} \exp(-i n \alpha_m) \\ &= \frac{1}{2N_\alpha - 1} \sum_{k_1} \sum_{m=0}^{m=2N_\alpha-2} (T_e/T_i) \delta \hat{\phi}_{k_1} \mathbf{i} \hat{\mathbf{k}}_1 \hat{v}_\perp / 2 \\ & \quad \times [\exp(i\alpha_m) \exp(-i\beta_1) + \exp(-i\alpha_m) \exp(i\beta_1)] \\ & \quad \cdot \left\{ \sum_{n'=-N_\alpha+1}^{n'=N_\alpha-1} \partial_\mu \delta \hat{F}_{k_2}^{n'} \exp(in' \alpha_m) \right\} \exp(-i n \alpha_m) \\ &= \sum_{k_1} (T_e/T_i) \delta \hat{\phi}_{k_1} \mathbf{i} \hat{\mathbf{k}}_1 \hat{v}_\perp / 2 [\exp(-i\beta_1) \partial_\mu \delta \hat{F}_{k_2}^{n-1} \\ & \quad + \exp(i\beta_1) \partial_\mu \delta \hat{F}_{k_2}^{n+1}]. \quad (\text{A.11}) \end{aligned}$$

In the first step of the above derivation process, $\partial_\mu N L_k^n(\hat{\mu})$ is replaced by the corresponding term in Eq. (A.7). In the second step of the above process, Eq. (A.2) is applied. In the last step of the above process, $n' = n-1$, $n' = n+1$ are set. The non-conservative form of the CKinFH equation is obtained as follows, by combining Eqs. (A.10) and (A.11):

$$\begin{aligned} & D \delta \hat{F}_k^n / D\hat{t} - i \hat{\omega}_k^d \delta \hat{G}_k^n + i k \rho \Omega_* / 2 [\exp(-i\beta) \delta \hat{G}_k^{n-1} \\ & \quad + \exp(i\beta) \delta \hat{G}_k^{n+1}] - \Omega_* i n \delta \hat{G}_k^n + i \hat{\omega}_{*k}^{nT} \delta \hat{\phi}_k (n_0 F_M) \delta_0^n \\ &= \sum_{k_1} \hat{k}_1 \delta \hat{\phi}_{k_1} (-i) / (2\hat{v}_\perp) [(n-1) \exp(-i\beta_1) \delta \hat{F}_{k_2}^{n-1} \\ & \quad - (n+1) \exp(i\beta_1) \delta \hat{F}_{k_2}^{n+1}] \\ & \quad + \sum_{k_1} (T_e/T_i) \delta \hat{\phi}_{k_1} \mathbf{i} \hat{\mathbf{k}}_1 \hat{v}_\perp / 2 [\exp(-i\beta_1) \partial_\mu \delta \hat{F}_{k_2}^{n-1} \\ & \quad + \exp(i\beta_1) \partial_\mu \delta \hat{F}_{k_2}^{n+1}]. \quad (\text{A.12}) \end{aligned}$$

A.1.3 The derivation of conservative nonlinear terms

The ∂_α is derived as Eq. (A.13):

$$\begin{aligned}
 \frac{1}{2N_\alpha - 1} \sum_{m=0}^{m=2N_\alpha-2} \partial_\alpha N L_k^n(\hat{\mu}) \exp(-i n \alpha_m) &= \frac{1}{2N_\alpha - 1} \sum_{m=0}^{m=2N_\alpha-2} \sum_{k1} \partial_\alpha (\delta \hat{\phi}_{k1} i \hat{k}_1 \cdot \hat{\mathbf{b}} \times \hat{\mathbf{v}}_\perp / \hat{v}_\perp^2 \delta f_{k2}) \exp(-i n \alpha_m) \\
 &= \frac{1}{2N_\alpha - 1} \sum_{k1} \sum_{m=0}^{m=2N_\alpha-2} \partial_\alpha \{ \hat{k}_1 \delta \hat{\phi}_{k1} i^2 / (2 \hat{v}_\perp) [\exp(i \alpha_m) \exp(-i \beta_1) - \exp(-i \alpha_m) \exp(i \beta_1)] \\
 &\quad \cdot \sum_{n'=-N_\alpha+1}^{n'=N_\alpha-1} \delta \hat{F}_{k2}^{n'} \exp(i n' \alpha_m) \} \exp(-i n \alpha_m) \\
 &= \frac{1}{2N_\alpha - 1} \sum_{m=0}^{m=2N_\alpha-2} \sum_{k1} \hat{k}_1 \delta \hat{\phi}_{k1} i^2 / (2 \hat{v}_\perp) [\exp(i \alpha_m) \exp(-i \beta_1) - \exp(-i \alpha_m) \exp(i \beta_1)] \\
 &\quad \cdot (i n') \left\{ \sum_{n'=-N_\alpha+1}^{n'=N_\alpha-1} \delta \hat{F}_{k2}^{n'} \exp(i n' \alpha_m) \right\} \exp(-i n \alpha_m) + \frac{1}{2N_\alpha - 1} \sum_{k1} \sum_{m=0}^{m=2N_\alpha-2} \hat{k}_1 \delta \hat{\phi}_{k1} i^2 / (2 \hat{v}_\perp) \\
 &\quad \times [i \exp(i \alpha_m) \exp(-i \beta_1) + i \exp(-i \alpha_m) \exp(i \beta_1)] \left\{ \sum_{n'=-N_\alpha+1}^{n'=N_\alpha-1} \delta \hat{F}_{k2}^{n'} \exp(i n' \alpha_m) \right\} \exp(-i n \alpha_m) \\
 &= \frac{1}{2N_\alpha - 1} \sum_{m=0}^{m=2N_\alpha-2} \sum_{k1} \hat{k}_1 \delta \hat{\phi}_{k1} i^2 / (2 \hat{v}_\perp) [\exp(i \alpha_m) \exp(-i \beta_1) i (1 + n') + \exp(-i \alpha_m) \exp(i \beta_1) i (1 - n')] \\
 &\quad \cdot \left\{ \sum_{n'=-N_\alpha+1}^{n'=N_\alpha-1} \delta \hat{F}_{k2}^{n'} \exp(i n' \alpha_m) \right\} \exp(-i n \alpha_m) \\
 &= \sum_{k1} -\delta \hat{\phi}_{k1} i \hat{k}_1 / (2 \hat{v}_\perp) [n \exp(-i \beta_1) \delta \hat{F}_{k2}^{n-1} - n \exp(i \beta_1) \delta \hat{F}_{k2}^{n+1}]. \tag{A.13}
 \end{aligned}$$

In the first step of the above derivation process, $\partial_\alpha N L_k^n(\hat{\mu})$ is replaced by the corresponding term in Eq. (A.8). In the second step of the above process, Eq.

(A.3) is applied. In the last step of the above process, $n' = n - 1$, $n' = n + 1$ are set.

The ∂_μ term is derived as Eq. (A.14):

$$\begin{aligned}
 \frac{1}{2N_\alpha - 1} \sum_{m=0}^{m=2N_\alpha-2} \partial_\mu N L_k^n(\hat{\mu}) \exp(-i n \alpha_m) &= \frac{1}{2N_\alpha - 1} \sum_{m=0}^{m=2N_\alpha-2} \sum_{k1} \partial_\mu [(T_e/T_i) \delta \hat{\phi}_{k1} i \hat{k}_1 \cdot \hat{\mathbf{v}}_\perp \delta f_{k2}] \exp(-i n \alpha_m) \\
 &= \frac{1}{2N_\alpha - 1} \sum_{k1} \sum_{m=0}^{m=2N_\alpha-2} \partial_\mu \left\{ (T_e/T_i) \delta \hat{\phi}_{k1} i \hat{k}_1 \hat{v}_\perp / 2 [\exp(i \alpha_m) \exp(-i \beta_1) + \exp(-i \alpha_m) \exp(i \beta_1)] \right. \\
 &\quad \cdot \sum_{n'=-N_\alpha+1}^{n'=N_\alpha-1} \delta \hat{F}_{k2}^{n'} \exp(i n' \alpha_m) \left. \right\} \exp(-i n \alpha_m) \\
 &= \sum_{k1} (T_e/T_i) \partial_\mu \left\{ \delta \hat{\phi}_{k1} i \hat{k}_1 \hat{v}_\perp / 2 [\exp(-i \beta_1) \delta \hat{F}_{k2}^{n-1} + \exp(i \beta_1) \delta \hat{F}_{k2}^{n+1}] \right\} \tag{A.14}
 \end{aligned}$$

In the first step of the above derivation process, $\partial_\mu N L_k^n(\hat{\mu})$ is replaced by the corresponding term in Eq. (A.8). In the second step of the above process, Eq. (A.2) is applied. In the last step of the above process,

$n' = n - 1$, $n' = n + 1$ are set. The conservative form of the CKinFH equation is obtained as Eq. (A.15), by combining Eqs. (A.13) and (A.14).

$$\begin{aligned}
 D \delta \hat{F}_k^n / D \hat{t} - i \hat{\omega}_k^d \delta \hat{G}_k^n + i k \rho \Omega_* / 2 [\exp(-i \beta) \delta \hat{G}_k^{n-1} + \exp(i \beta) \delta \hat{G}_k^{n+1}] - \Omega_* i n \delta \hat{G}_k^n + i \hat{\omega}_{*k}^{nT} \delta \hat{\phi}_k (n_0 F_M) \delta_0^n \\
 = \sum_{k1} \hat{k}_1 \delta \hat{\phi}_{k1} (-i) / (2 \hat{v}_\perp) [n \exp(-i \beta_1) \delta \hat{F}_{k2}^{n-1} - n \exp(i \beta_1) \delta \hat{F}_{k2}^{n+1}]
 \end{aligned}$$

$$+ \sum_{k1} (T_e/T_i) \partial_{\hat{\mu}} \{ \delta \hat{\phi}_{k1} i \hat{k}_1 \hat{v}_{\perp} / 2 [\exp(-i\beta_1) \delta \hat{F}_{k2}^{n-1} + \exp(i\beta_1) \delta \hat{F}_{k2}^{n+1}] \}. \quad (\text{A.15})$$

A.2 Derivation of nonlinear incremental entropy conservation

The CKinFH equations are taken as examples in this section to prove the nonlinear incremental entropy conservation. The incremental entropy of CKinFH is defined as

$$\begin{aligned} S &= \sum_{\mathbf{k}} \oint d\alpha \int_0^{\infty} d\hat{\mu} (\delta \hat{f}_{\mathbf{k}}^* \delta \hat{f}_{\mathbf{k}}) \\ &= 2\pi \int_0^{\infty} d\hat{\mu} \sum_{\mathbf{k}} \sum_{n=-N_{\alpha}+1}^{n=N_{\alpha}-1} (\delta \hat{F}_{\mathbf{k}}^n)^* \delta \hat{F}_{\mathbf{k}}^n. \end{aligned} \quad (\text{A.16})$$

The time derivative of the incremental entropy should be zero:

$$\int_0^{\infty} d\hat{\mu} \sum_{\mathbf{k}} \sum_{n=-N_{\alpha}+1}^{n=N_{\alpha}-1} (\delta \hat{F}_{\mathbf{k}}^n)^* d\delta \hat{F}_{\mathbf{k}}^n / dt + c.c. = 0.$$

Only the nonlinear terms in the above equation are needed for proving the nonlinear incremental entropy conservation:

$$\int_0^{\infty} d\hat{\mu} \sum_{\mathbf{k}} \sum_{n=-N_{\alpha}+1}^{n=N_{\alpha}-1} (\delta \hat{F}_{\mathbf{k}}^n)^* {}^{NL}S(\hat{k}, \hat{\mu}, n) + c.c. = 0, \quad (\text{A.17})$$

where ${}^{NL}S(\hat{k}, \hat{\mu}, n)$ represents the nonlinear terms. Note the conjugate condition $\delta \hat{F}_{-\mathbf{k}}^n = (\delta \hat{F}_{\mathbf{k}}^{-n})^*$.

A.2.1 The incremental entropy conservation of the ∂_{μ} term

Conservative form.

Eq. (A.18) is obtained by substituting the ${}^{NL}S(\hat{k}, \hat{\mu}, n)$ term in Eq. (A.17) into the conservative ∂_{μ} term in Eq. (A.15).

$$\begin{aligned} &\int_0^{\infty} d\hat{\mu} \sum_{\mathbf{k}} \sum_{n=-N_{\alpha}+1}^{n=N_{\alpha}-1} (\delta \hat{F}_{\mathbf{k}}^n)^* \partial_{\hat{\mu}} \left\{ \sum_{k1} (T_e/T_i) \delta \hat{\phi}_{k1} (i \hat{k}_1 \hat{v}_{\perp} / 2) [\exp(-i\beta_1) \delta \hat{F}_{k2}^{n-1} + \exp(i\beta_1) \delta \hat{F}_{k2}^{n+1}] \right\} + c.c. \\ &= (T_e/T_i) \int_0^{\infty} d\hat{\mu} \sum_{\mathbf{k}} \sum_{k1} \sum_{k2} \delta(\mathbf{k} + \mathbf{k}_1 + \mathbf{k}_2) \sum_{n=-N_{\alpha}+1}^{n=N_{\alpha}-1} \delta \hat{F}_{\mathbf{k}}^{-n} \partial_{\hat{\mu}} \{ \delta \hat{\phi}_{k1} (i \hat{k}_1 \hat{v}_{\perp} / 2) [\exp(-i\beta_1) \delta \hat{F}_{k2}^{n-1} \\ &\quad + \exp(+i\beta_1) \delta \hat{F}_{k2}^{n+1}] \} + c.c. \\ &= -(T_e/T_i) \int_0^{\infty} d\hat{\mu} \sum_{\mathbf{k}} \sum_{k1} \sum_{k2} \delta(\mathbf{k} + \mathbf{k}_1 + \mathbf{k}_2) \sum_{n=-N_{\alpha}+1}^{n=N_{\alpha}-1} \{ \delta \hat{\phi}_{k1} (i \hat{k}_1 \hat{v}_{\perp} / 2) [\exp(-i\beta_1) \delta \hat{F}_{k2}^{n-1} \\ &\quad + \exp(+i\beta_1) \delta \hat{F}_{k2}^{n+1}] \} \partial_{\hat{\mu}} (\delta \hat{F}_{\mathbf{k}}^{-n}) + c.c.. \end{aligned} \quad (\text{A.18})$$

In the first step of Eq. (A.18), the wavenumber \mathbf{k} is replaced by $-\mathbf{k}$. In the second step, integration by parts is performed, and a zero boundary condition (A.19) is assumed as Eq. (A.19).

$$\{ \delta \hat{\phi}_{k1} (i \hat{k}_1 \hat{v}_{\perp} / 2) [\exp(-i\beta_1) \delta \hat{F}_{k2}^{n-1}$$

$$+ \exp(+i\beta_1) \delta \hat{F}_{k2}^{n+1}] (\delta \hat{F}_{\mathbf{k}}^{-n}) \} \Big|_0^{\infty} + c.c. \Big|_0^{\infty} = 0. \quad (\text{A.19})$$

Non-conservative form.

Eq. (A.20) is obtained by substituting the ${}^{NL}S(\hat{k}, \hat{\mu}, n)$ term in Eq. (A.17) into the non-conservative ∂_{μ} term in Eq. (A.12).

$$\begin{aligned} &\int_0^{\infty} d\hat{\mu} \sum_{\mathbf{k}} \sum_{n=-N_{\alpha}+1}^{n=N_{\alpha}-1} (\delta \hat{F}_{\mathbf{k}}^n)^* \sum_{k1} (T_e/T_i) \delta \hat{\phi}_{k1} (i \hat{k}_1 \hat{v}_{\perp} / 2) [\exp(-i\beta_1) \partial_{\hat{\mu}} \delta \hat{F}_{k2}^{n-1} + \exp(+i\beta_1) \partial_{\hat{\mu}} \delta \hat{F}_{k2}^{n+1}] + c.c. \\ &= (T_e/T_i) \int_0^{\infty} d\hat{\mu} \sum_{\mathbf{k}} \sum_{k1} \sum_{k2} \delta(\mathbf{k} + \mathbf{k}_1 + \mathbf{k}_2) \sum_{n=-N_{\alpha}+1}^{n=N_{\alpha}-1} \delta \hat{F}_{\mathbf{k}}^{-n} \{ \delta \hat{\phi}_{k1} (i \hat{k}_1 \hat{v}_{\perp} / 2) [\exp(-i\beta_1) \partial_{\hat{\mu}} (\delta \hat{F}_{k2}^{n-1}) \\ &\quad + \exp(+i\beta_1) \partial_{\hat{\mu}} (\delta \hat{F}_{k2}^{n+1})] \} + c.c. \\ &= (T_e/T_i) \int_0^{\infty} d\hat{\mu} \sum_{\mathbf{k}} \sum_{k1} \sum_{k2} \delta(\mathbf{k} + \mathbf{k}_1 + \mathbf{k}_2) \sum_{n=-N_{\alpha}+1}^{n=N_{\alpha}-1} \{ \delta \hat{\phi}_{k1} (i \hat{k}_1 \hat{v}_{\perp} / 2) [\exp(-i\beta_1) \delta \hat{F}_{k2}^{n-1} \\ &\quad + \exp(+i\beta_1) \delta \hat{F}_{k2}^{n+1}] \} \partial_{\hat{\mu}} (\delta \hat{F}_{\mathbf{k}}^{-n}) + c.c.. \end{aligned} \quad (\text{A.20})$$

In the first step of Eq. (A.20), the wavenumber \mathbf{k} is replaced by $-\mathbf{k}$. In the second step, the identity in Eq. (A.21) is first applied, following which the wavenumbers \mathbf{k} and \mathbf{k}_2 are swapped. The identity in Eq. (A.21) will be proved at the end of this section.

$$\sum_{n=-N_\alpha+1}^{n=N_\alpha-1} \delta A^n \delta B^{-(n\pm 1)} = \sum_{n=-N_\alpha+1}^{n=N_\alpha-1} \delta B^n \delta A^{-(n\pm 1)}. \quad (\text{A.21})$$

As discussed in Section 2.3.4, the nonlinear terms in the rCYCLO code are calculated by adding the conservative form to the equivalent non-conservative form of nonlinear terms and dividing by 2 to precisely ensure the nonlinear incremental entropy conservation. The nonlinear incremental entropy conservation of the ∂_μ term can be demonstrated by adding Eq. (A.18) to Eq. (A.20) and showing that the result of this addition is zero.

Derivation of the identity in Eq. (A.21).

The function $c(\alpha)$ is an arbitrary function of the gyro-phase α , which equals to $a(\alpha)$ times $b(\alpha)$:

$$c(\alpha) = a(\alpha)b(\alpha) = \sum_{n_1=-N_\alpha+1}^{n_1=N_\alpha-1} \delta A_{n_1} \exp(+in_1\alpha_m) \cdot \sum_{n_2=-N_\alpha+1}^{n_2=N_\alpha-1} \delta B_{n_2} \exp(+in_2\alpha_m). \quad (\text{A.22})$$

where $a(\alpha)$ and $b(\alpha)$ are expanded in Fourier series. An arbitrary Fourier series of $c(\alpha)$ is presented as δC_n .

$$\delta C_n = \frac{1}{2N_\alpha - 1} \sum_{m=0}^{m=2N_\alpha-2} c(\alpha) \exp(-in\alpha_m),$$

We replace $c(\alpha)$ by the RHS of Eq. (A.22).

$$\delta C_n = \frac{1}{2N_\alpha - 1} \sum_{m=0}^{m=2N_\alpha-2} \exp(-in\alpha_m)$$

$$\begin{aligned} & \int_0^\infty d\hat{\mu} \sum_k \sum_{n=-N_\alpha+1}^{n=N_\alpha-1} (\delta \hat{F}_k^n)^* \sum_{k_1} \delta \hat{\phi}_{k_1}(-i)(\hat{k}_1/2\hat{v}_\perp) n [\exp(-i\beta_1) \delta \hat{F}_{k_2}^{n-1} - \exp(+i\beta_1) \delta \hat{F}_{k_2}^{n+1}] + c.c. \\ &= \int_0^\infty d\hat{\mu} \sum_k \sum_{k_1} \sum_{k_2} \delta(\mathbf{k} + \mathbf{k}_1 + \mathbf{k}_2) \sum_{n=-N_\alpha+1}^{n=N_\alpha-1} n \delta \hat{F}_k^{-n} \delta \hat{\phi}_{k_1}(-i)(\hat{k}_1/2\hat{v}_\perp) \{ \exp(-i\beta_1) \delta \hat{F}_{k_2}^{n-1} \\ & \quad - \exp(+i\beta_1) \delta \hat{F}_{k_2}^{n+1} \} + c.c., \end{aligned} \quad (\text{A.25})$$

where the wavenumber \mathbf{k} is replaced by $-\mathbf{k}$.

Non-conservative form.

Eq. (A.26) is obtained by substituting the $^{NL}S(\hat{k}, \hat{\mu}, n)$ term in Eq. (A.17) into the non-conservative ∂_α term in Eq. (A.12).

$$\int_0^\infty d\hat{\mu} \sum_k \sum_{n=-N_\alpha+1}^{n=N_\alpha-1} (\delta \hat{F}_k^n)^*$$

$$\begin{aligned} & \cdot \sum_{n_1=-N_\alpha+1}^{n_1=N_\alpha-1} \delta A_{n_1} \exp(+in_1\alpha_m) \\ & \cdot \sum_{n_2=-N_\alpha+1}^{n_2=N_\alpha-1} \delta B_{n_2} \exp(+in_2\alpha_m) \\ &= \frac{1}{2N_\alpha - 1} \sum_{n_1=-N_\alpha+1}^{n_1=N_\alpha-1} \delta A_{n_1} \sum_{n_2=-N_\alpha+1}^{n_2=N_\alpha-1} \delta B_{n_2} \\ & \cdot \sum_{m=0}^{m=2N_\alpha-2} \exp[-i(n - n_1 - n_2)\alpha_m]. \end{aligned}$$

Eq. (A.23) is obtained by setting $n_2 = n - n_1$.

$$\delta C_n = \sum_{n_1=-N_\alpha+1}^{n_1=N_\alpha-1} \delta A_{n_1} \delta B_{n-n_1}. \quad (\text{A.23})$$

Otherwise, Eq. (A.24) is obtained by setting $n_1 = n - n_2$.

$$\delta C_n = \sum_{n_2=-N_\alpha+1}^{n_2=N_\alpha-1} \delta A_{n-n_2} \delta B_{n_2}. \quad (\text{A.24})$$

The identity in Eq. (A.21) is proved by adding Eq. (A.23) to Eq. (A.24):

$$\begin{aligned} \delta C_{\mp 1} &= \sum_{n=-N_\alpha+1}^{n=N_\alpha-1} \delta A^n \delta B^{-(n\pm 1)} \\ &= \sum_{n=-N_\alpha+1}^{n=N_\alpha-1} \delta B^n \delta A^{-(n\pm 1)}. \end{aligned}$$

A.2.2 The incremental entropy conservation of the ∂_α term

Conservative form.

Eq. (A.25) is obtained by substituting the $^{NL}S(\hat{k}, \hat{\mu}, n)$ term in Eq. (A.17) into the conservative ∂_α term in Eq. (A.15).

$$\begin{aligned} & \cdot \sum_{k_1} \delta \hat{\phi}_{k_1}(-i)(\hat{k}_1/2\hat{v}_\perp) [\exp(-i\beta_1)(n-1) \delta \hat{F}_{k_2}^{n-1} \\ & \quad - \exp(+i\beta_1)(n+1) \delta \hat{F}_{k_2}^{n+1}] + c.c. \\ &= \int_0^\infty d\hat{\mu} \sum_k \sum_{k_1} \sum_{k_2} \delta(\mathbf{k} + \mathbf{k}_1 + \mathbf{k}_2) \sum_{n=-N_\alpha+1}^{n=N_\alpha-1} \delta \hat{F}_k^n \\ & \cdot \delta \hat{\phi}_{k_1}(-i)(\hat{k}_1/2\hat{v}_\perp) [\exp(-i\beta_1)(-n-1) \delta \hat{F}_{k_2}^{n-1} \end{aligned}$$

$$-\exp(+i\beta_1)(-n+1)\delta\hat{F}_{k_2}^{-n+1}] + c.c., \quad (\text{A.26})$$

where the wavenumber \mathbf{k} is replaced by $-\mathbf{k}$, and har-

monic n is replaced by $-n$. The two terms of Eq. (A.26) are treated respectively, as follows.

The first term of Eq. (A.26) is treated as

$$\begin{aligned} & \int_0^\infty d\hat{\mu} \sum_k \sum_{k_1} \sum_{k_2} \delta(\mathbf{k} + \mathbf{k}_1 + \mathbf{k}_2) \sum_{n=-N_\alpha+1}^{n=N_\alpha-1} \delta\hat{F}_k^n \delta\hat{\phi}_{k_1}(-i)(\hat{k}_1/2\hat{v}_\perp) \exp(-i\beta_1)(-n-1)\delta\hat{F}_{k_2}^{-n-1} + c.c. \\ &= \int_0^\infty d\hat{\mu} \sum_k \sum_{k_1} \sum_{k_2} \delta(\mathbf{k} + \mathbf{k}_1 + \mathbf{k}_2) \delta\hat{\phi}_{k_1}(-1)(\hat{k}_1/2\hat{v}_\perp) \exp(-i\beta_1) \sum_{n=-N_\alpha+1}^{n=N_\alpha-1} \delta\hat{F}_k^n i(-n-1)\delta\hat{F}_{k_2}^{-n-1} + c.c. \\ &= \int_0^\infty d\hat{\mu} \sum_k \sum_{k_1} \sum_{k_2} \delta(\mathbf{k} + \mathbf{k}_1 + \mathbf{k}_2) \delta\hat{\phi}_{k_1}(-1)(\hat{k}_1/2\hat{v}_\perp) \exp(-i\beta_1) \sum_{n'=-N_\alpha+2}^{n'=N_\alpha} \delta\hat{F}_k^{n'-1}(-in')\delta\hat{F}_{k_2}^{-n'} + c.c. \\ &= \int_0^\infty d\hat{\mu} \sum_k \sum_{k_1} \sum_{k_2} \delta(\mathbf{k} + \mathbf{k}_1 + \mathbf{k}_2) \delta\hat{\phi}_{k_1}(-1)(\hat{k}_1/2\hat{v}_\perp) \exp(-i\beta_1) \sum_{n'=-N_\alpha+2}^{n'=N_\alpha} \delta\hat{F}_k^{-n'}(-in')\delta\hat{F}_{k_2}^{n'-1} + c.c. \\ &= \int_0^\infty d\hat{\mu} \sum_k \sum_{k_1} \sum_{k_2} \delta(\mathbf{k} + \mathbf{k}_1 + \mathbf{k}_2) \delta\hat{\phi}_{k_1}(-1)(\hat{k}_1/2\hat{v}_\perp) \exp(-i\beta_1) \sum_{n'=-N_\alpha+1}^{n'=N_\alpha-1} \delta\hat{F}_k^{-n'}(-in')\delta\hat{F}_{k_2}^{n'-1} + c.c.. \quad (\text{A.27}) \end{aligned}$$

In the second step of Eq. (A.27), $n' = n+1$ is chosen. In the third step, the wavenumbers \mathbf{k} and \mathbf{k}_2 are swapped. The fourth step replaces the summation $\sum_{n'=-N_\alpha+2}^{n'=N_\alpha}$ with $\sum_{n'=-N_\alpha+1}^{n'=N_\alpha-1}$, which requires the periodic properties of the distribution function and the derivative harmonic identity, as described below:

$$\delta\hat{F}_k^{-n'}(-in')|_{n'=N_\alpha} = \delta\hat{F}_k^{-N_\alpha+(2N_\alpha-1)}i[-N_\alpha$$

$$+(2N_\alpha-1)]$$

$$= \delta\hat{F}_k^{-n'}(-in')|_{n'=-N_\alpha+1},$$

$$\delta\hat{F}_{k_2}^{n'-1}|_{n'=N_\alpha} = \delta\hat{F}_{k_2}^{N_\alpha-1-(2N_\alpha-1)}$$

$$= \delta\hat{F}_{k_2}^{n'-1}|_{n'=-N_\alpha+1}.$$

The second term of Eq. (A.26) is treated as

$$\begin{aligned} & \int_0^\infty d\hat{\mu} \sum_k \sum_{k_1} \sum_{k_2} \delta(\mathbf{k} + \mathbf{k}_1 + \mathbf{k}_2) \delta\hat{\phi}_{k_1}(\hat{k}_1/2\hat{v}_\perp) \exp(+i\beta_1) \sum_{n=-N_\alpha+1}^{n=N_\alpha-1} \delta\hat{F}_k^n i(-n+1)\delta\hat{F}_{k_2}^{-n+1} + c.c. \\ &= \int_0^\infty d\hat{\mu} \sum_k \sum_{k_1} \sum_{k_2} \delta(\mathbf{k} + \mathbf{k}_1 + \mathbf{k}_2) \delta\hat{\phi}_{k_1}(\hat{k}_1/2\hat{v}_\perp) \exp(+i\beta_1) \sum_{n=-N_\alpha}^{n=N_\alpha-2} \delta\hat{F}_k^{n'+1}i(-n')\delta\hat{F}_{k_2}^{-n'} + c.c. \\ &= \int_0^\infty d\hat{\mu} \sum_k \sum_{k_1} \sum_{k_2} \delta(\mathbf{k} + \mathbf{k}_1 + \mathbf{k}_2) \delta\hat{\phi}_{k_1}(\hat{k}_1/2\hat{v}_\perp) \exp(+i\beta_1) \sum_{n=-N_\alpha}^{n=N_\alpha-2} \delta\hat{F}_k^{-n'}i(-n')\delta\hat{F}_{k_2}^{n'+1} + c.c. \\ &= \int_0^\infty d\hat{\mu} \sum_k \sum_{k_1} \sum_{k_2} \delta(\mathbf{k} + \mathbf{k}_1 + \mathbf{k}_2) \delta\hat{\phi}_{k_1}(\hat{k}_1/2\hat{v}_\perp) \exp(+i\beta_1) \sum_{n=-N_\alpha+1}^{n=N_\alpha-1} \delta\hat{F}_k^{-n'}i(-n')\delta\hat{F}_{k_2}^{n'+1} + c.c.. \quad (\text{A.28}) \end{aligned}$$

In the second step of (A.28), $n' = n-1$ is chosen. In the third step, the wavenumbers \mathbf{k} and \mathbf{k}_2 are swapped. The fourth step replaces the summation $\sum_{n'=-N_\alpha}^{n'=N_\alpha-2}$ with $\sum_{n'=-N_\alpha+1}^{n'=N_\alpha-1}$, which also requires the periodic properties of the distribution function and the derivative harmonic identity, as described below:

$$\begin{aligned} \delta\hat{F}_k^{-n'}i(-n')|_{n'=-N_\alpha} &= \delta\hat{F}_k^{N_\alpha-(2N_\alpha-1)}i[N_\alpha \\ &\quad -(2N_\alpha-1)] \\ &= \delta\hat{F}_k^{-n'}i(-n')|_{n'=N_\alpha-1}, \end{aligned}$$

$$\delta\hat{F}_{k_2}^{n'+1}|_{n'=-N_\alpha} = \delta\hat{F}_{k_2}^{N_\alpha+1+(2N_\alpha-1)}$$

$$= \delta\hat{F}_{k_2}^{n'+1}|_{n'=N_\alpha-1}.$$

Next, Eq. (A.29) is obtained by combining Eq. (A.27) with Eq. (A.28).

$$\begin{aligned} & \int_0^\infty d\hat{\mu} \sum_k \sum_{n=-N_\alpha+1}^{n=N_\alpha-1} (\delta\hat{F}_k^n)^* \\ & \cdot \sum_{k_1} \delta\hat{\phi}_{k_1}(-i)(\hat{k}_1/2\hat{v}_\perp) [\exp(-i\beta_1)(n-1)\delta\hat{F}_{k_2}^{n-1} \end{aligned}$$

$$\begin{aligned}
 & -\exp(+i\beta_1)(n+1)\delta\hat{F}_{k2}^{n+1}] + c.c. \\
 & = \int_0^\infty d\hat{\mu} \sum_k \sum_{k_1} \sum_{k_2} \delta(\mathbf{k} + \mathbf{k}_1 + \mathbf{k}_2) \sum_{n=-N_\alpha+1}^{n=N_\alpha-1} \delta\hat{F}_k^n \\
 & = - \int_0^\infty d\hat{\mu} \sum_k \sum_{k_1} \sum_{k_2} \delta(\mathbf{k} + \mathbf{k}_1 + \mathbf{k}_2) \\
 & \quad \cdot \sum_{n=-N_\alpha+1}^{n=N_\alpha-1} n \delta\hat{F}_k^{-n} \delta\hat{\phi}_{k1}(-i)(\hat{k}_1/2\hat{v}_\perp) \\
 & \quad \cdot \{\exp(-i\beta_1)\delta\hat{F}_{k2}^{n-1} - \exp(+i\beta_1)\delta\hat{F}_{k2}^{n+1}\} + c.c..
 \end{aligned} \tag{A.29}$$

The nonlinear incremental entropy conservation of the ∂_α term is demonstrated by adding Eq. (A.25) to Eq. (A.29) and showing that the result is zero.

In Sections A.2.1 and A.2.2, the nonlinear incremental entropy conservation of CKinFH has been proved. The proof for the CKinCH form is analogous, and will not be repeated.

References

1. M. N. Rosenbluth and A. N. Kaufman, Plasma diffusion in a magnetic field, *Phys. Rev.* 109(1), 1 (1958)
2. D. Pfirsch and A. Schluter, Max Planck Institute Report MPI/PA/7/62 (unpublished), 1962
3. H. W. Hendel, T. K. Chu, and P. A. Politzer, Collisional drift waves — Identification, stabilization, and enhanced plasma transport, *Phys. Fluids* 11(11), 2426 (1968)
4. S. C. Prager, A. K. Sen, and T. C. Marshall, Dissipative trapped-electron instability in cylindrical geometry, *Phys. Rev. Lett.* 33(12), 692 (1974)
5. J. Slough, G. A. Navratil, and A. K. Sen, Production and observation of the dissipative trapped-ion instability, *Phys. Rev. Lett.* 47(15), 1057 (1981)
6. R. Scarmozzino, A. K. Sen, and G. A. Navratil, Production and identification of a collisionless, curvature-driven, trapped-particle instability, *Phys. Rev. Lett.* 57(14), 1729 (1986)
7. A. K. Sen, J. Chen, and M. Mauel, Production and identification of the ion-temperature-gradient instability, *Phys. Rev. Lett.* 66(4), 429 (1991)
8. E. Mazzucato, Small-scale density fluctuations in the adiabatic toroidal compressor, *Phys. Rev. Lett.* 36(14), 792 (1976)
9. C. M. Surko and R. E. Slusher, Study of the density fluctuations in the adiabatic toroidal compressor scattering tokamak using CO₂ laser, *Phys. Rev. Lett.* 37(26), 1747 (1976)
10. R. E. Slusher and C. M. Surko, Study of density fluctuations in the absorption of oxygen on silicon, *Phys. Rev. Lett.* 40(6), 400 (1978)
11. W. Horton, Spectral distribution of drift-wave fluctuations in Tokamaks, *Phys. Rev. Lett.* 37(19), 1269 (1976)
12. R. V. Bravenec, K. W. Gentle, B. Richards, D. W. Ross, D. C. Sing, A. J. Wootton, D. L. Brower, N. C. Luhmann, W. A. Peebles, C. X. Yu, T. P. Crowley, J. W. Heard, R. L. Hickok, P. M. Schoch, and X. Z. Yang, Core turbulence and transport studies on the Texas Experimental Tokamak, *Phys. Fluids B Plasma Phys.* 4(7), 2127 (1992)
13. K. W. Gentle, R. V. Bravenec, G. Cima, H. Gasquet, G. A. Hallock, P. E. Phillips, D. W. Ross, W. L. Rowan, A. J. Wootton, T. P. Crowley, J. Heard, A. Ouroua, P. M. Schoch, and C. Watts, An experimental counter-example to the local transport paradigm, *Plasma Phys. Contr. Fusion* 2(6), 2292 (1995)
14. G. Cima, R. V. Bravenec, A. J. Wootton, T. D. Rempel, R. F. Gandy, C. Watts, and M. Kwon, Core temperature fluctuations and related heat transport in the Texas Experimental Tokamak-Upgrade, *Phys. Plasmas* 2(3), 720 (1995)
15. C. Watts, R. F. Gandy, G. Cima, R. V. Bravenec, D. W. Ross, A. J. Wootton, A. Ouroua, J. W. Heard, T. P. Crowley, P. M. Schoch, D. L. Brower, Y. Jiang, B. Deng, C. W. Domier, and N. C. Luhmann, Poloidal asymmetry and gradient drive in core electron density and temperature fluctuations on the Texas Experimental Tokamak-Upgrade, *Phys. Plasmas* 3(5), 2013 (1996)
16. B. H. Deng, D. L. Brower, G. Cima, C. W. Domier, N. C. Luhmann, and C. Watts, Mode structure of turbulent electron temperature fluctuations in the Texas Experimental Tokamak Upgrade, *Phys. Plasmas* 5(12), 4117 (1998)
17. A. Hasegawa and K. Mima, Stationary spectrum of strong turbulence in magnetized nonuniform plasma, *Phys. Rev. Lett.* 39(4), 205 (1977)
18. A. Hasegawa and K. Mima, Pseudo-three-dimensional turbulence in magnetized nonuniform plasma, *Phys. Fluids* 21(1), 87 (1978)
19. A. Hasegawa and M. Wakatani, Plasma edge turbulence, *Phys. Rev. Lett.* 50(9), 682 (1983)
20. R. E. Waltz, R. R. Dominguez, and G. W. Hammett, Gyro-Landau fluid models for toroidal geometry, *Phys. Fluids B Plasma Phys.* 4(10), 3138 (1992)
21. P. H. Rutherford and E. A. Frieman, Drift instabilities in general magnetic field configurations, *Phys. Fluids* 11(3), 569 (1968)
22. J. B. Taylor and R. J. Hastie, Stability of general plasma equilibria - I formal theory, *Plasma Phys.* 10(5), 479 (1968)
23. T. M. Antonsen and B. Lane, Kinetic equations for low frequency instabilities in inhomogeneous plasmas, *Phys. Fluids* 23(6), 1205 (1980)
24. P. J. Catto, W. M. Tang, and D. E. Baldwin, Generalized gyrokinetics, *Plasma Phys.* 23(7), 639 (1981)
25. E. A. Frieman and L. Chen, Nonlinear gyrokinetic equations for low-frequency electromagnetic waves in general plasma equilibria, *Phys. Fluids* 25(3), 502 (1982)
26. C. Holland, A. E. White, G. R. McKee, M. W. Shafer, J. Candy, R. E. Waltz, L. Schmitz, and G. R. Tynan, Implementation and application of two synthetic diagnostics for validating simulations of core Tokamak turbulence, *Phys. Plasmas* 16(5), 052301 (2009)

27. J. Candy and R. E. Waltz, Anomalous transport scaling in the DIII-D Tokamak matched by supercomputer simulation, *Phys. Rev. Lett.* 91(4), 045001 (2003)
28. R. E. Waltz, Search for the missing L-mode edge transport and possible breakdown of gyro kinetics, BAPS Series II, 57(12), 105, DI3-2 (2012)
29. A. E. White, L. Schmitz, G. R. McKee, C. Holland, W. A. Peebles, T. A. Carter, M. W. Shafer, M. E. Austin, K. H. Burrell, J. Candy, J. C. DeBoo, E. J. Doyle, M. A. Makowski, R. Prater, T. L. Rhodes, G. M. Staebler, G. R. Tynan, R. E. Waltz, and G. Wang, Measurements of core electron temperature and density fluctuations in DIII-D and comparison to nonlinear gyrokinetic simulations, *Phys. Plasmas* 15(5), 056116 (2008)
30. T. Rhodes, C. Holland, S. Smith, A. White, K. Burrell, J. Candy, J. DeBoo, E. Doyle, J. Hillesheim, J. Kinsey, G. McKee, D. Mikkelsen, W. Peebles, C. Petty, R. Prater, S. Parker, Y. Chen, L. Schmitz, G. Staebler, R. E. Waltz, G. Wang, Z. Yan, and L. Zeng, L-mode validation studies of gyrokinetic turbulence simulations via multiscale and multifield turbulence measurements on the DIII-D Tokamak, *Nucl. Fusion* 51(6), 063022 (2011)
31. R. E. Waltz and D. Zhao, Nonlinear theory of drift-cyclotron kinetics and the possible breakdown of gyro-kinetics, *Phys. Plasmas* 20(1), 012507 (2013)
32. Zhao Deng and R. E. Waltz, Numerical methods for nonlinear simulations of cyclotronics illustrating the breakdown of gyrokinetics at high turbulence levels, *Comput. Phys. Commun.* 195, 23 (2015)
33. R. D. Hazeltine and J. D. Meiss, Plasma Confinement, Addison-Wesley, 1992
34. W. E. Drummond and M. N. Rosenbluth, Anomalous diffusion arising from microinstabilities in a plasma, *Phys. Fluids* 5(12), 1507 (1962)
35. N. A. Krall and M. N. Rosenbluth, Trapping instabilities in a slightly inhomogeneous plasma, *Phys. Fluids* 5(11), 1435 (1962)
36. N. A. Krall and M. N. Rosenbluth, Universal instability in complex field geometries, *Phys. Fluids* 8(8), 1488 (1965)
37. T. F. R. Group, J. Adam, J. F. Bonnal, A. Breson, et al., Ion-cyclotron instability in the TFR Tokamak, *Phys. Rev. Lett.* 41(2), 113 (1978)
38. R. E. Waltz and R. R. Dominguez, Ion cyclotron modes in Tokamaks, *Phys. Fluids* 24(8), 1575 (1981)
39. Zhao Deng and R. E. Waltz, Testing the high turbulence level breakdown of low-frequency gyrokinetics against high-frequency gyrokinetic simulations, *Phys. Plasmas* 22(5), 056101 (2015)
40. S. I. Braginskii, Reviews of Plasma Physics, edited by M. A. Leontovich, Consultants Bureau, New York, 1965, Vol. I, 205
41. S. Chapman and T. G. Cowling, Mathematical Theory of Nonuniform Cases, Cambridge University Press, 1953
42. A. Sommerfeld, Thermodynamics and Statistical Mechanics, Academic Press, New York, 1949
43. L. D. Landau and E. M. Lifshits, Fluid Mechanics, Addison-Wesley, Reading, Mass, 1959
44. B. A. Trubnikov, Reviews of Plasma Physics, edited by M. A. Leontovich, Consultants Bureau, New York, 1965, Vol. I, 105
45. F. L. Hinton and R. E. Waltz, Gyrokinetic turbulent heating, *Phys. Plasmas* 13(10), 102301 (2006)
46. I. S. Gradshteyn and I. M. Ryzhik, Tables of Integrals, Series, and Products, Academic, 1965
47. J. Candy and R. E. Waltz, Velocity-space resolution, entropy production, and upwind dissipation in Eulerian gyrokinetic simulations, *Phys. Plasmas* 13(3), 032310 (2006)
48. J. Candy and R. E. Waltz, An Eulerian gyrokinetic-Maxwell solver, *J. Comput. Phys.* 186(2), 545 (2003)
49. W. Dorland, F. Jenko, M. Kotschenreuther, and B. N. Rogers, Electron temperature gradient turbulence, *Phys. Rev. Lett.* 85(26), 5579 (2000)
50. M. Kotschenreuther, G. Rewoldt, and W. M. Tang, Comparison of initial value and eigenvalue codes for kinetic toroidal plasma instabilities, *Comput. Phys. Commun.* 88(2-3), 128 (1995)
51. Z. Lin, S. Ethier, T. S. Hahm, and W. M. Tang, Size scaling of turbulent transport in magnetically confined plasmas, *Phys. Rev. Lett.* 88(19), 195004 (2002)
52. R. E. Waltz, J. Candy, and C. C. Petty, Projected profile similarity in gyrokinetic simulations of Bohm and gyro-Bohm scaled DIII-D L and H modes, *Phys. Plasmas* 13(7), 072304 (2006)
53. E. N. Lorenz, Deterministic nonperiodic flow, *J. Atmos. Sci.* 20(2), 130 (1963)
54. A. E. White, N. T. Howard, M. Greenwald, M. L. Reinke, C. Sung, S. Baek, M. Barnes, J. Candy, A. Dominguez, D. Ernst, C. Gao, A. E. Hubbard, J. W. Hughes, Y. Lin, D. Mikkelsen, F. Parra, M. Porkolab, J. E. Rice, J. Walk, S. J. Wukitch, and A. C. M. Team, Multi-channel transport experiments at Alcator C-Mod and comparison with gyrokinetic simulations, *Phys. Plasmas* 20(5), 056106 (2013)
55. N. T. Howard, A. E. White, M. Reinke, M. Greenwald, C. Holland, J. Candy, and J. Walk, Validation of the gyrokinetic model in ITG and TEM dominated L-mode plasmas, *Nucl. Fusion* 53(12), 123011 (2013)
56. N. T. Howard, A. E. White, M. Greenwald, M. L. Reinke, J. Walk, C. Holland, J. Candy, and T. Gorler, Investigation of the transport shortfall in Alcator C-Mod L-mode plasmas, *Phys. Plasmas* 20(3), 032510 (2013)
57. N. T. Howard, C. Holland, A. E. White, M. Greenwald, and J. Candy, Synergistic cross-scale coupling of turbulence in a Tokamak plasma, *Phys. Plasmas* 21(11), 112510 (2014)
58. D. Told, F. Jenko, T. Gorler, F. J. Casson, and E. Fable, Characterizing turbulent transport in ASDEX Upgrade L-mode plasmas via nonlinear gyrokinetic simulations, *Phys. Plasmas* 20(12), 122312 (2013)
59. J. Chowdhury, W. Wan, Y. Chen, S. E. Parker, R. J. Groebner, C. Holland, and N. T. Howard, Study of the L-mode tokamak plasma "shortfall" with local and global nonlinear gyrokinetic δf particle-in-cell simulation, *Phys. Plasmas* 21(11), 112503 (2014)